Path Integral Computer Simulations of Liquid Water

Matthew Glover

A thesis submitted for the degree of
Doctor of Philosophy

University of York
Department of Physics

January 2004

Abstract

Liquid water exhibits a well-known maximum of density at 4°C and 1 atm pressure. The temperature at which this density maximum occurs is known to *increase* when hydrogen in the water molecule is replaced with a heavier isotope; such an isotope with a *reduced* degree of nuclear quantum delocalisation causes water to behave *less* like a simple liquid.

The structure of water close to the density maximum has been studied by computer simulation, using the technique of path integral molecular dynamics. It was found that the magnitude of quantum spreading seen in the liquid is in good agreement with theoretical calculations for a proton or deuteron in a harmonic potential with respect to hydrogen bond bending, and is essentially unaffected by changes in temperature and density over the range considered here.

First and second neighbour characteristics were analysed in relation to hydrogen bond bending and first neighbour orientational characteristics. Quantum versus classical simulation demonstrated destructuring effects in the quantum fluid consistent with an increase in temperature over the classical counterpart. When the quantum simulation of *heavy* water was compared to that of light water, a stronger intermolecular bonding network was found to exist. Second nearest neighbour molecules at a reduced radial distance would seem to be surrounded by regions with a higher degree of local structure. Building on previous ideas concerning the mechanism by which the density maximum occurs, it is therefore proposed that the inflated density seen in heavy water compared with light water at its density maximum is the result of a cooperation between a greater level of tetrahedrality in the liquid structure and a greater degree of saturation of that structure with molecular interstitials.

“Lead me, O Lord . . . make thy way plain before my face.”
Psalms 5:8

To the glory of God.

My life is but a weaving
Between my Lord and me,
I cannot chose the colours
He worketh steadily.

Oft times he weaveth sorrow,
And I in foolish pride
Forget he sees the upper
And I, the underside.

Not till the loom is silent
And the shuttle cease to fly
Shall God unroll the canvas
And explain the reason why.

The dark threads are as needful
In the Weaver’s skillful hand
As the threads of gold and silver
In the pattern He has planned.

Author unknown

Contents

List of Figures

List of Tables

Acknowledgements

I would like to begin by acknowledging the support of my supervisor, Dr. Matt Probert — academically, personally and spiritually. He is a man who has demonstrated an abundance of patience and tolerance over the past few years, going out of his way on numerous occasions for my benefit. And he taught me a thing or two about coffee. Thanks also to Rex Godby who has played a significant role in my academic development, and bought me lots of coffee.

A great deal of further support has come from colleagues — and friends — and housemates: Kris, Lee, Dave and Luke. These are people who have demonstrated symptoms of genuine amusement when confronted with my sense of humour.

I would like to say a special thankyou to my other friends in York, without whom I would be quite lost. Though in some sense pained to mention individuals for fear of choosing favourites, there are a few people to whom I'd like to offer a particularly deep brand of thanks for keeping me sane (with the bunny-rabbit ears): Ian, Hilary, Emma, Angela and Kris. There is, however, a much wider circle of people I hold very dear; people around whom I find a sanctuary in which I can be a bit "Maffish". Thanks also to my family for understanding my lack of contact.

I must extend a huge thankyou to the people of Heslington Church, and to the music group in particular. Special thanks must be extended to Alison, Robert and Hugh, and further to Graham and Sue for taking me in when I needed a home.

Thanks also to the EPSRC who made my studies financially possible through the provision of a 3-year research grant.

I have often said that life is a training in the acceptance of imperfection; an exercise in making the best of what you already have. My life as a postgraduate student has borne this out time and again. Last but most certainly not least, I would like to thank God for standing by me. Even when I shouted.

Author’s Declaration

I declare that the work presented in this thesis, except where otherwise stated, is based on my own research and has not been submitted previously for a degree in this or any other University.

Signed,

Matthew J. Glover

Chapter 1

Introduction

1.1 Water

Water is the only substance which occurs naturally as a solid, liquid and vapour (Franks, 1983). It is essential for life; our own bodies are $\sim$ 65–70% water (Franks, 1972). We drink it, and we wash in it as indicated by Figure 1.1.

Yet despite the apparent simplicity of the water molecule, water in the liquid phase has many anomalous properties, as we shall see in Chapter 2. A snapshot of liquid water from the present calculations is shown in Figure 1.2.

Among the liquid anomalies sits the famous density maximum at 4°C below which water begins to *expand* on cooling, contrary to simple liquid behaviour. If it were not for the preference of water to expand as it cools — and hence freeze from the *top downwards* — life on Earth would not have survived the first winter.

Scientific consensus states that the anomalous properties are a consequence of hydrogen bonding; the desirable formation of hydrogen bonds counteracts an arrangement into a more close-packed structure. Further, the literature highlights the importance of the *second* nearest neighbour configuration, which therefore plays a key part in the analysis presented here.

1.2 Motivation

As we shall see in Chapter 2, the temperature at which the density maximum occurs — or the *temperature of maximum density* (TMD) — is strongly influenced by the isotope of hydrogen which in part forms the water molecule. We shall go on to see

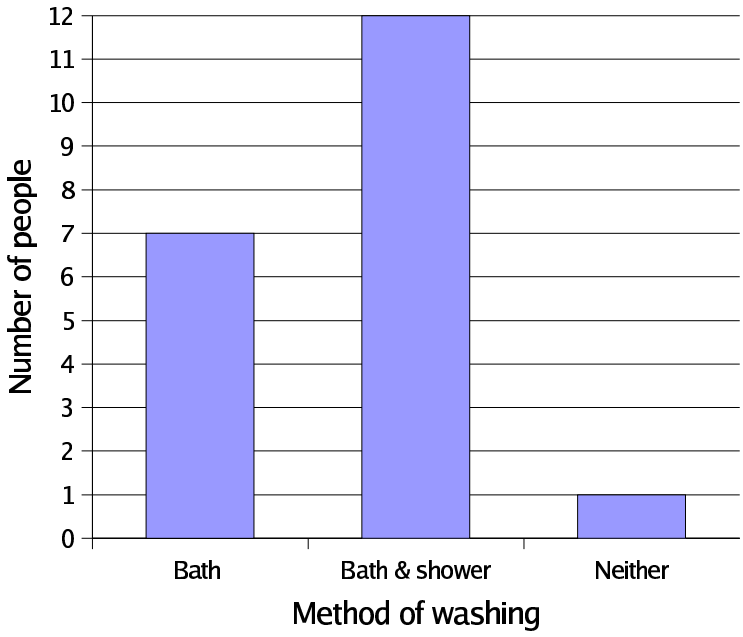

Figure 1.1: Distribution of washing techniques amongst people in the author's class at Austwick Primary School (1988/89).

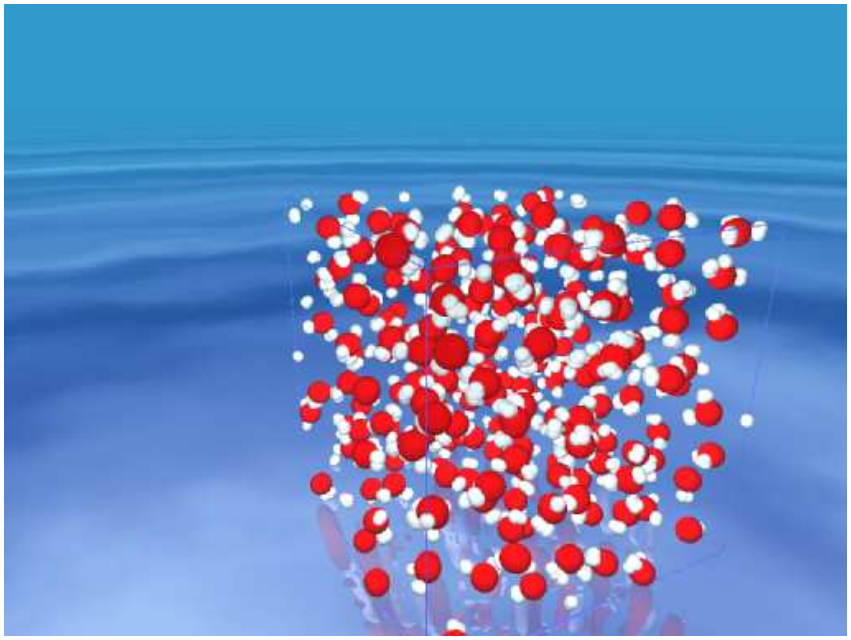

Figure 1.2: Snapshot of liquid water from the present work. Oxygen atoms are shown as red, and hydrogen as white.

that the TMD in heavy water is *higher* than that seen in light water. In other words, when a *heavier* isotope of hydrogen is included in the water molecule, the TMD is shifted *upwards*; the expected reduction in quantum effects owing to the heavier deuterium atoms results in water behaving *less* like a simple liquid!

It is the purpose of this thesis to study the role which the quantum mechanical nature of atomic *nuclei* has to play with regard to the local structure of water close to the density maximum. Comparisons are made between a classical and a quantum model for water, and the change in quantum behaviour is studied under isotopic substitution.

1.3 Molecular dynamics

Though molecular dynamics simulation is dependent upon our theoretical knowledge of atomic interactions, it is inexpensive in comparison with experiment and affords direct access to a microscopic view of structural behaviour; structure functions, for example, are easy to calculate.

Water was simulated here using both classical and path integral molecular dynamics. As we shall see in later chapters, the former yields access to ensemble averages for a classical system through time averages. Path integral molecular dynamics builds upon this and allows access to *quantum* ensemble averages by averaging over both real and *imaginary* time.

Since *nuclear* quantum properties are of interest here, an explicit account of *electronic* quantum behaviour was sacrificed so as to facilitate simulation with a sufficiently large number of molecules; indeed, a suitable number is required to build structure functions, and path integral molecular dynamics makes heavy computational demands.

1.3.1 The MUDPIES code

The molecular dynamics calculations for the present work were performed using the computer program MUDPIES, written by the author. The program name is a tenuous acronym of *MolecUlar Dynamics using Path Integrals for Empirical Systems*. Later chapters describe elements of theory from which it is built. For now, however, MUDPIES is a parallel code written in Fortran90 with message passing. It boasts a dual communicator topology, allowing parallelism to work for both accuracy and speed.

1.4 Outline of thesis

A summary of the the current understanding of water, with particular reference to the density maximum is given in Chapter 2. Chapters 3 to 5 concern the ideas behind molecular dynamics, the description of intermolecular interactions and the incorporation of nuclear quantum effects into the framework of molecular dynamics. Chapters 6 and 7 present an analysis of the raw degree of quantum spreading, and structural consequences of the same. Chapter 8 draws the thesis to a conclusion.

While Chapter 5 sets out the conceptual foundation of path integrals, a derivation of the path integral starting from Schrödinger's equation is left to Appendix A.

Chapter 2

Water

2.1 Introduction

In this chapter we shall meander through current understanding as regards the behavioural anomalies observed in liquid water, from both microscopic and thermodyamic perspectives.

Sections 2.2 and 2.2 describe the water monomer and dimer. Anomalous behaviour of the liquid is outlined in Section 2.4. The structure of solid water — ice — is touched upon in Section 2.5. Section 2.6 discusses the nearest neighbour characteristics of the liquid, and Section 2.7 considers hydrogen bonding. Section 2.8 looks at properties of water in terms of *macroscopic* quantities. The nature of quantum fluctuations in the liquid is considered in Section 2.9, and Section 2.10 brings the chapter to a close.

2.2 The water molecule

Before we look at water in condensed phases, we first consider the isolated water molecule.

Working with orbitals of the hydrogen atom, we note that hydrogen in its ground state has the electronic configuration $1s$ and oxygen has the configuration $1s^2 2s^2 2p^4$. Oxygen therefore has two electron vacancies in its outer shell. Hydrogen atoms in the water molecule can be understood to form covalent bonds with the oxygen atom, with the hydrogen and oxygen atoms acting as an electron donor and acceptor respectively. The model thus far would predict a value of 90° for the H-O-H bond

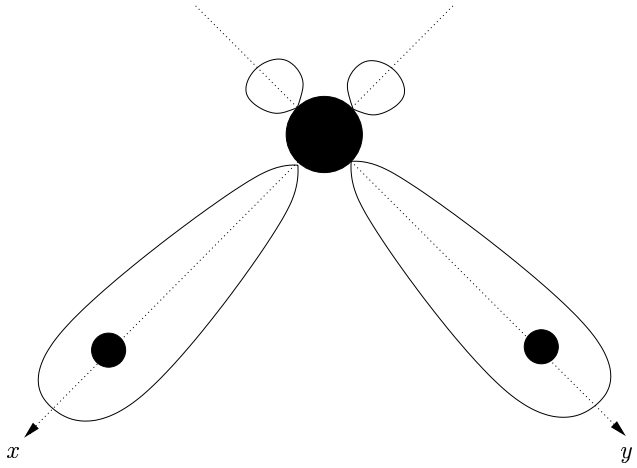

Figure 2.1: Hydrogen atoms in a water molecule bonding with the p-orbitals of an oxygen atom. If this was a complete description of O-H bonding within the water molecule, the bond angle would be 90°. Redrawn from Coulson (1961).

angle. So how can we account for the experimental value of 104°? Coulson (1961) has summarised the main reasons:

1. The hydrogen atoms in the water carry a net positive charge and hence repel. Heath and Linnett (1948) determined that this accounts for a widening of the H-O-H angle of up to 90°.

2. The electrons brought to the molecule by the hydrogen atoms mean that there is now an extra electron in both the x and y directions — bond repulsion may be considered to contribute towards the widened bond angle.

3. $2s^2$ electrons from the oxygen atom form hydrid orbitals with the $2p^4$ orbitals.

4. Configurational interaction, which relates to quantum correlation effects.

Coulson covers s-p hybridisation in a little more depth. Constructing linear combinations of orbitals using λ and μ as "mixing parameters":

$$|\psi_i\rangle = |s\rangle + \lambda\,|p_i\rangle \tag{2.1a}$$

$$|\psi_j\rangle = |s\rangle + \mu\,|p_j\rangle \tag{2.1b}$$

which will be orthogonal if

$$\langle\psi_i\,|\psi_j\rangle = \langle s + \lambda p_i\,|s + \mu p_j\rangle = 0 \tag{2.2}$$

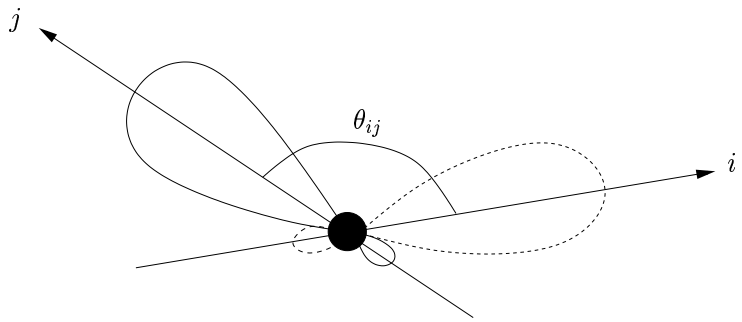

Figure 2.2: Resultant geometry from hybridisation of s and p-orbitals. Redrawn from Coulson (1961).

Type of hybridisation	Pure s	Digonal sp	Trigonal sp^2	Tetrahedral sp^3	Pure p
Example		Acetylene	Ethylene	Methane	
Value of λ	0	1	$\sqrt{2}$	$\sqrt{3}$	
Valence angle		180°	120°	109.47°	90°

Table 2.1: Some values of λ for which the orthogonality condition in Equation 2.5 is met. (Coulson, 1961).

Expanding the bra-ket in Equation 2.2:

$$\langle \psi_i \, | \psi_j \rangle = \langle s \, | s \rangle + \mu \, \langle s \, | p_j \rangle + \lambda \, \langle p_i \, | s \rangle + \lambda\mu \, \langle p_i \, | p_j \rangle \tag{2.3}$$

which reduces to

$$\begin{aligned} \langle \psi_i \, | \psi_j \rangle &= \langle s \, | s \rangle + \lambda\mu \cos\theta_{ij} \, \langle p_i \, | p_i \rangle \\ &= 1 + \lambda\mu \cos\theta_{ij} \end{aligned} \tag{2.4}$$

and if the hybrids are equivalent, then we are left with the condition that

$$1 + \lambda^2 \cos\theta_{ij} = 0 \tag{2.5}$$

So we may choose any combination of λ and θ_{ij} such that $\lambda^2 \cos\theta_{ij} = -1$. Some values of λ for which this condition is met are given in Table 2.1. We see that for $\lambda = \sqrt{3}$, we recover the tetrahedral angle of 109.47° — which is closer to the experimental value than that predicted by bonding only through p-orbitals.

Bond	Energy / KJ mol^{-1}	Energy / eV per molecule
Intramolecular OH	492 [a]	5.10
Intermolecular HO	23.3 [b]	0.242

[a] Ruscic *et al.* (2002)
[b] Suresh and Naik (2000)

Table 2.2: Intramolecular and intermolecular dissociation energies.

2.3 The water dimer

The water dimer is the simplest possible example of bound water molecules. We shall take some time here to discuss the configuration of the dimer, and the mechanism by which the molecules are bound.

2.3.1 Hydrogen bonding

Hydrogen bonding was first proposed as the mechanism for the binding of water molecules by Latimer and Rodebush (1920). A hydrogen bond is formed when a hydrogen atom lies between two highly electronegative atoms, such as oxygen atoms. Martí *et al.* (1996) have given a set of geometrical criteria under which two water molecules may be said to be hydrogen bonded:

1. The distance R_{OO} between the oxygen of both molecules is smaller than $R^c_{OO} = 3.6$ Å.

2. The distance R_{OH} between the oxygen of the *acceptor* molecule and the hydrogen of the *donor* is less than a given R^c_{OH}, where R^c_{OH} is the distance of the first minimum of the radial distribution function[1] $g_{OH}(r)$, and is generally taken as 2.4 Å.

3. The bond bending angle θ_{bend} between the O-O direction and the molecular O-H direction of the *donor* is less than some fixed value, such as θ^c_{bend} = 30°.

Table 2.2 gives the dissociation energies of intramolecular OH bonds and also that of two hydrogen bonded water molecules. Note that the energy associated with the forming of the hydrogen bond is just 5% of that of the intramolecular OH bond — a hydrogen bond is comparatively weak.

[1] Radial distribution functions are introduced in Chapter 3.

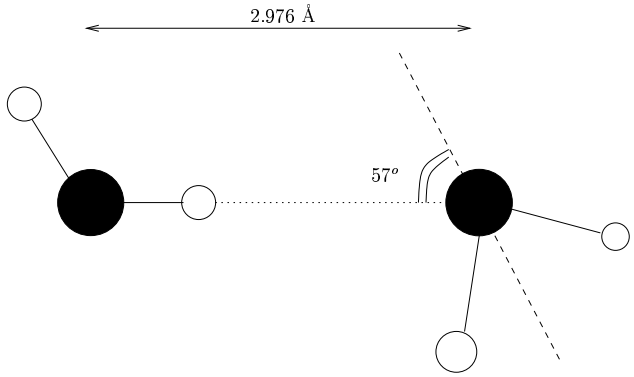

Figure 2.3: Configuration of the water dimer. The hydrogen atoms of the left and rightmost molecules lie on the axes parallel and normal to the plane of the paper respectively.

2.3.2 Configuration

The water dimer occurs naturally in the vapour phase, and its configuration has been studied experimentally by Dyke *et al.* (1977) and Odutola and Dyke (1980). A graphical illustration is given in Figure 2.3.

2.4 Anomalous behaviour

Key anomalies of liquid water have been summarised by Cho *et al.* (1997), and we shall consider them together with explanations here.

2.4.1 The density maximum

Perhaps the most famous manifestation of the anomalous behaviour of liquid water is that of the density maximum. Below a temperature of 4°C — at atmospheric pressure — the density of the liquid begins to *decrease* on cooling, in contrast with simple liquid behaviour; the density profile is shown in Figure 2.4. Insight into this phenomenon has come from both experiment (Bosio *et al.*, 1983) and computer simulation (Sciortino *et al.*, 1990; Jedlovszky *et al.*, 2000; Jedlovszky and Vallauri, 2001; Sciortino *et al.*, 1991).

Further, there exists a discontinuity in the density profile upon freezing. The densities of the liquid and the solid at the freezing point are given in Table 2.3.

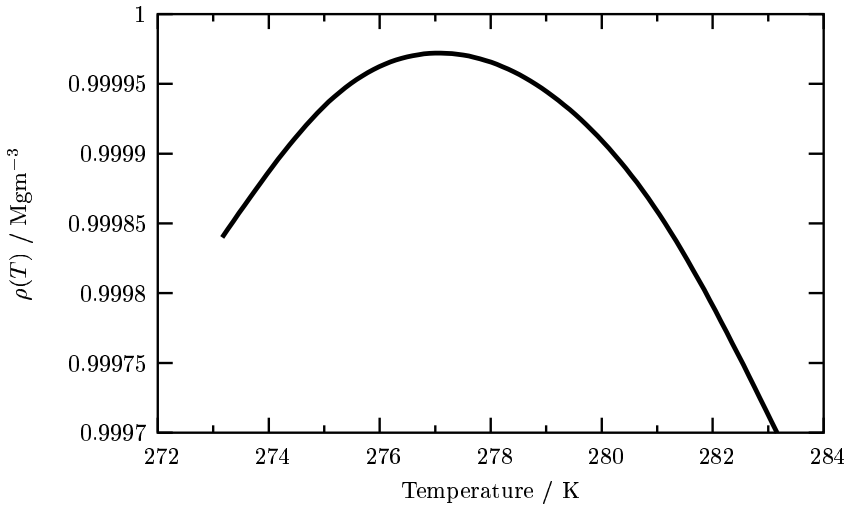

Figure 2.4: Density profile of liquid water as a function of temperature at atmospheric pressure. Data taken from Kell (1967).

	Density / Mgm^{-3}
Ice	0.91668 [a]
Water	0.999840 [b]

[a] Ginnings and Corruccini (1947)
[b] Kell (1967)

Table 2.3: Densities of ice and water the freezing point.

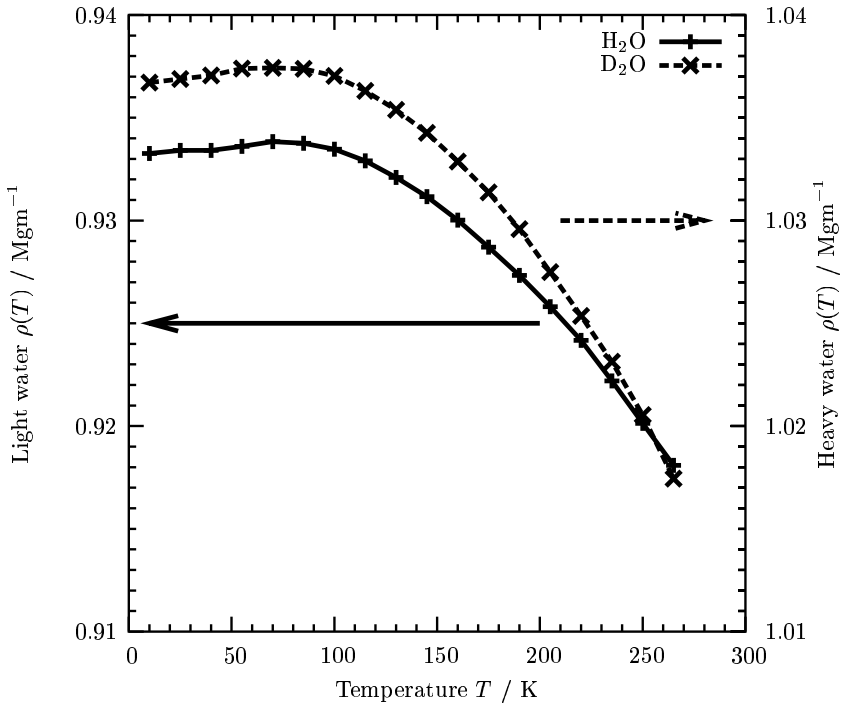

Figure 2.5: Density profile of solid H_2O and D_2O as a function of temperature at atmospheric pressure. Densities were calculated using the lattice parameter data of Röttger *et al.* (1994).

2.4.2 Other anomalies

Pressure effect

In contrast with more familiar logic, high pressures inhibit the freezing action of water, and the melting temperature is made lower. The water now has to push back harder against the applied pressure in order to form the stiffer, less dense structure.

Temperature dependent vibrations

The frequency of intermolecular modes *decreases* with increasing temperature. As the hydrogen bonds are weakened and the more dense structure forms, molecules find themselves in more shallow and flat potential minima.

Viscosity anomaly

High external pressure inhibits the water from forming the stronger, less dense structure — the pressure holds the water in the dense and much more loose structure. Therefore, rather than pressure increasing the viscosity as is the case in simple liquids, it is *lowered*.

Heat capacity anomaly

The energetically desirable dense structure is strong — it takes a lot of thermal energy to break bonds. The heat capacity below the density maximum is therefore seen to be surprisingly high.

Non-Arrhenius behaviour

According to the Arrhenius equation, the diffusion coefficient

$$D = \frac{1}{6N}\frac{\mathrm{d}}{\mathrm{d}t}\left\langle \sum_{i=1}^{N} \left(\boldsymbol{r}_i(t) - \boldsymbol{r}_i(0)\right)^2 \right\rangle \tag{2.6}$$

may be expressed as (Einsenberg and Kauzmann, 1969)

$$D = A\exp\left(-\frac{E_\mathrm{A}}{RT}\right) \tag{2.7}$$

where A is a constant. Here the diffusion coefficient is related to barrier heights in the system, with the exponential term expressing a probability that the barrier would be overcome. The formation of the hydrogen bond network has a significant effect on barrier heights, inducing a departure from Arrhenius behaviour.

Isotopic substitution

It is this anomaly which will be most relevant to us. Heavy water shows a temperature of maximum density (TMD) at about 11°C, which is *higher* than the observed value of about 4°C in light water. If the density maximum were to be in part stimulated by increasing nuclear quantum delocalisation, one might expect that the reduced quantum nature of the deuteron as compared with the lighter hydrogen nucleus would delay the onset of anomalous behaviour as the temperature is lowered. The reverse is true.

2.5 Ice

Before we go on to consider the structure of the liquid, we shall first look at the structure of solid water — ice. Figure 2.6 shows the structure of ice Ih, or "ordinary" ice. We see that the ice adopts a tetrahedral arrangement, with each molecule hydrogen bonded to four nearest neighbours.

Pauling (1935) put forward four assumptions about ice, which we shall quote here:

1. In ice each oxygen atom has two hydrogen atoms attached to it at distances of about 0.95 Å, forming a water molecule.
2. Each water molecular is oriented so that its two hydrogen atoms are directed approximately toward two of the four oxygen atoms which surround it tetrahedrally, forming hydrogen bonds.
3. The orientations of adjacent water molecules are such that only one hydrogen atom lies approximately along each oxygen-oxygen axis.
4. Under ordinary conditions the interaction of non-adjacent molecules is not such as to appreciable stablize any one of the many configurations satisfying the preceding conditions with reference to the others.

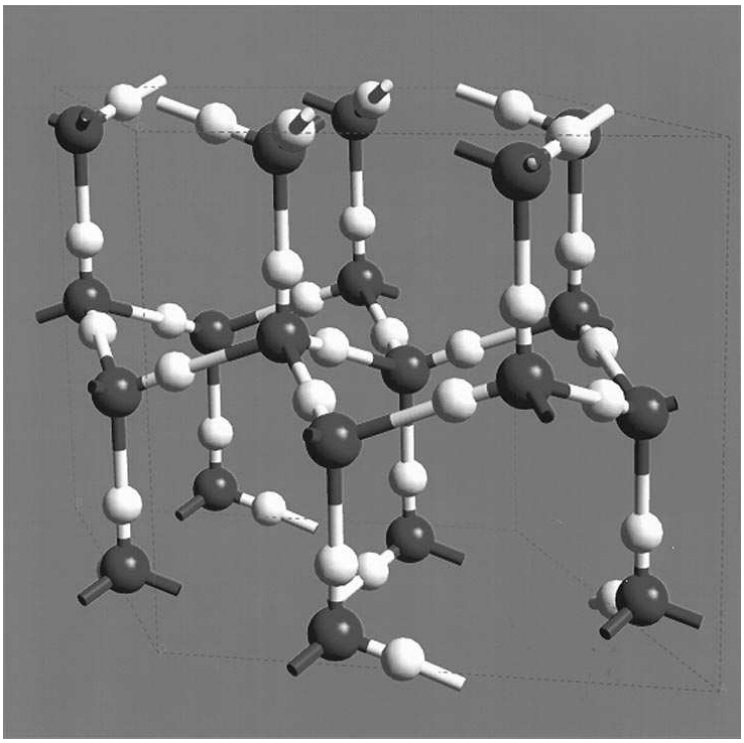

Figure 2.6: Structure of ice Ih. The grey and white balls represent oxygen and hydrogen atoms respectively. Taken from Isaacs *et al.* (2000).

Pauling was able to give credibility to these assumptions by obtaining a theoretical value for the entropy of ice which was in good agreement with the experimental value. The first and third of these assumptions have become known as the "ice rules" (Petrenko and Whitworth, 1999).

We note here that in ice, the nearest neighbour oxygen–oxygen separation R_{OO} is reduced from 2.976 Å in the dimer to about 2.8 Å (Xantheas and Dunning, 1993). Ding *et al.* (1987) used a Density Functional Theory[2] (DFT) scheme which predicted correctly that water freezes to the hexagonal lattice of Figure 2.6; further, the observed density in the computer model was found to be 10% lower than that of liquid water, which they comment as being in good agreement with the experimental value of 8.3%.

2.6 Neighbour characteristics

Now that we have an awareness of the structure of ice Ih, we shall go on to compare its nearest neighbour characteristics with those in the liquid.

[2]Density Functional Theory is described briefly in Chapter 4.

	Coordination number
Close packing	12
Liquid sodium	10
Water	4

Table 2.4: Number of particles present in the first coordination shell for a few different systems. Water clearly may not be represented by a close packed system of spheres — the coordination number is radically different to that for such a system. Data quoted in Morgan and Warren (1938).

	Radius of first peak / Å
Ice Ih	2.76
Water at 1.5°C	2.90
Water at 83°C	3.05

Table 2.5: Location of the first peak of the RDF in both water and ice. Data quoted in Morgan and Warren (1938).

We find an indication of the similarities of the structure of solid and liquid water by comparison of the coordination numbers; that is, the number of molecules appearing in the first nearest neighbour peak of the radial distribution function[3] (RDF). In a face-centered cubic (FCC) lattice where we see close packed spheres, any atom has 12 nearest neighbours. Morgan and Warren (1938) note that sodium forms an FCC lattice in its solid phase, and as such we would expect the number of first nearest neighbours in the liquid phase to be slightly less than 12; indeed, liquid sodium has a coordination number of 10. Table 2.4 compares the number of nearest neighbours present in sodium with that in water. The fact that the coordination number in liquid water is so very much smaller than that in sodium indicates that the liquid is not at all close-packed; indeed, the coordination number in the liquid is approximately that of ice Ih. The above provides evidence pointing to the imposing presence of the tetrahedral hydrogen-bonded ice-like structure in the *liquid* phase.

Narten *et al.* (1967) measured the radial distribution function in H_2O at various different temperatures. The location of the peaks and troughs are centered roughly around those neighbour distances seen in ice I, but smeared out. However, a smeared radial distribution for ice does not account for the RDF seen for liquid water. Prins and Petersen (1936) applied an error function to the crystal RDF; it failed to account for 3.4 nearest neighbours seen at a radius of about 3.6 Å.

If ice were a perfectly tetrahedral structure, we may calculate the expected distance of the second coordination shell given our knowledge of the first nearest neighbour

[3] See Chapter 3.

Temp °C	1.5	13	30	62	83
Number	4.4	4.4	4.6	4.9	4.9

Table 2.6: Number of nearest neighbour molecules present in the first coordination shell in liquid water for a range of different temperatures. The liquid has approximately the four-fold coordination as seen in ice Ih. Data quoted in Morgan and Warren (1938).

distance:

$$r = 2.76 \times \left(\frac{8}{3}\right)^{\frac{1}{2}} = 4.51\,\text{Å} \tag{2.8}$$

Note that this calculated second nearest neighbour distance agrees not only with the location of the second peak in the RDF for ice Ih, but it also lends further support approximately tetrahedral structures appearing in *liquid* water; the peak at about 4.5 Å is also seen there. This has lended support to the picture in which water is composed of a distorted hydrogen bond network. This notion is supported by the work of Tanaka (2001), who notes that strong vibrational peaks are observed in the liquid at the same positions as those in ice Ih; further, the peaks are better defined for four-fold hydrogen bonding over those due to molecules forming fewer H-bonds. Moreover, the *ab initio* computer simulations of Sato and Fumio (1999) indicate that "water largely retains the short range structure which is characteristic to ice . . . in the normal density".

Table 2.6 gives the number of molecules in the first coordination shell at a range of different temperatures. We see here the increasing distortion of the four-fold structure with increasing temperature; in contrast with sodium, however, the number of nearest neighbours *increases* with temperature. As we shall see, this may be viewed as the increased close-packing of molecules collapsing from the *second* nearest neighbour shell.

As Bernal and Fowler (1933) point out, simply stating four-fold coordination is not enough to fix the structure of water. They describe various four-fold coordinated structures present in the liquid as presented in Table 2.7. Bernal and Fowler go on to highlight the similarities and differences between first and second nearest neighbour distances of the tridymite-like and quartz-like structures, which are given in Table 2.8; although the first nearest neighbour distance remains the same in both structures, the inward movement of the second nearest neighbour peak would account for a 17% decrease in volume. Note that it is not the *first* nearest neighbour separation which differs in the two structures, but rather the *second* nearest neigh-

Type	Description	Dominance
Water I	Tridymite-ice-like	Corresponds to ordinary ice. Present to some degree at temperatures below 4°C.
Water II	Quartz-like	Predominant at ordinary temperatures.
Water III	Ammonia-like	Predominant at high temperatures but some distance below the critical point at 374°C.

Table 2.7: Different types of four-fold coordinated structures present in liquid water, as given by Bernal and Fowler (1933).

	First NN distance / Å	Second NN distance / Å
Tridymite-ice-like	2.8	4.5
Quartz-like	2.8	4.2

Table 2.8: Nearest neighbour distances in different four-fold crystal structures present in liquid water, as quoted in Bernal and Fowler (1933).

bour separation. Indeed, the first nearest neighbour oxygen-oxygen separation is the same in *all* forms of liquid water and ice (Bosio *et al.*, 1983; Einsenberg and Kauzmann, 1969).

An inward collapse of the second nearest neighbour distance has been seen by experiment, yet by a larger degree than that predicted by the above changing-structure scenario painted by Bernal and Fowler. Bosio *et al.* (1983) found that under the action of hydrogen bond bending, second nearest neighbour O–O distances at 4.5 Å collapse inward to a distance of 3.4 Å in heavy water; as temperature is increased, the structure collapses to one which is more dense and less stable.

In the light of computational studies, Sciortino *et al.* (1990) suggested that these *interstitial* second nearest neighbours may form *bifurcated* bonds with the central molecule. That is to say, the interstitial molecules may jointly hydrogen bond to an arm of the central molecule; the authors note that the mean energies of a single bond and a bifurcated bond are roughly the same. It is possible, then, for a water molecule to be “five-or-more bonded”.

This notion of a *second* neighbour collapse has been borne out by the computer simulations of Jedlovszky *et al.* (2000); Jedlovszky and Vallauri (2001) who, on analysing isochoric water on each side of the density maximum, found that heating the liquid reduced the number of 4-bonded molecules; the proportion of molecules having 1–3 *and* 5–6 hydrogen bonded nearest neighbours increased — this is shown in Figure 2.7. The density maximum, then, is thought to be the result of a competition between the effects of H-bond network breakdown — which acts to increase

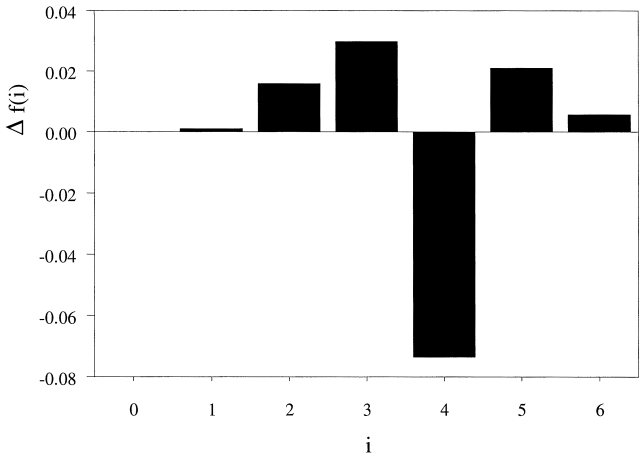

Figure 2.7: Isochoric differential of the fraction of molecules $f(i)$ having exactly i bonded neighbours. The separation between the two temperatures ΔT = 20 K, one state point on each side of the density maximum. Taken from Jedlovszky *et al.* (2000).

the density — and common thermal expansion; the density maximum marks the watershed.

Cho *et al.* (1996a) were able to construct an explanation of the density maximum which hinged on a double well potential relating to *second* nearest neighbour interactions, as illustrated in Figure 2.8. The outer, deeper well corresponded to the more distant O-O separation at 4.5 Å characteristic of ice; upon heating, second neighbours may hop into the inner well — thus increasing the density. They went on to investigate computationally a potential which had a minimum designed to exist at an O-O separation of 3.4 Å, and successfully reproduced water-like anomalous behaviour (Cho *et al.*, 1997).

2.7 Hydrogen bonding

So far we have a picture of water containing molecules with several degrees of hydrogen bonding. The anomalous density behaviour is thought to be induced by the formation of approximately linear hydrogen bonds which require a more open tetrahedral-like structure. Indeed, relationships between translational and tetrahedral order have been found in simulated water by Errington and Debenedetti (2001), revealing a strong correlation between the order parameters for each. Further, diffusive and thermodynamic anomalous behaviour was found to be contained within an envelope of structural anomaly.

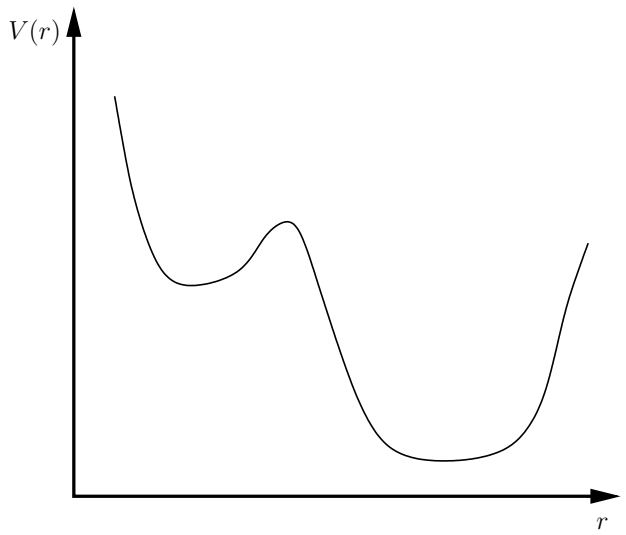

Figure 2.8: Double well potential relevant to *second* nearest neighbour interactions. Cho *et al.* (1996a) have proposed such a double well to explain the density anomaly.

2.7.1 Hydrogen bond formation

Models have been investigated which focus on the degree of connectivity; that is, purely on number of hydrogen bonds formed (Némethy and Scheraga, 1962; Stanley and Teixeira, 1980; Khan, 2000; Borick and Debenedetti, 1993; Truskett and Dill, 2002). Recently, Tanaka (1998b) obtained an excellent description of the density maximum using a potential of the form:

$$V(r,\Omega) = \overline{V}(r) + \Delta V(r,\Omega) \tag{2.9}$$

where Ω describes molecular orientation. The first term in Equation 2.9 depends upon the density, and the second on the orientational configuration of molecules. In the model, neither of the two potential terms alone describe the density maximum; rather it is the competition of the two which shows the desired result. Tanaka goes on to make the assertion that

> "the anomaly of ρ, κ_{T} and C_{P} is primarily due to neither thermodynamic singularity[4] nor cooperativity of hydrogen bonding[5], but due to the coupling between density and bond order parameters".

Sastry *et al.* (1993) note that orientational entropy competes against the formation of linear hydrogen bonds, which are energetically more favourable; even in regions

[4]Thermodynamic characteristics of water are explored in Section 2.8.
[5]Cooperativity is discussed in Subsection 2.7.3.

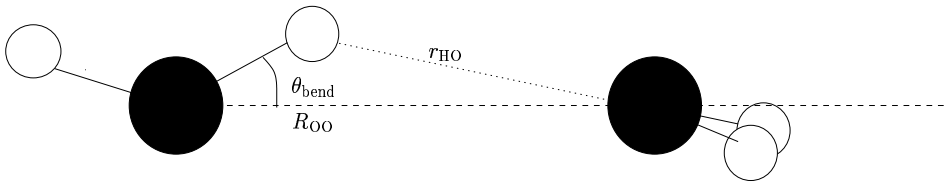

Figure 2.9: Illustration of lengths and bending angle in a water-water hydrogen bond; values are given in Table 2.9.

where the thermal energy is significantly less than the well depth of hydrogen bonding, the liquid state still persists. They saw anomalous behaviour consistent with water in a lattice-based model, which incorporates three basic features as quoted here:

1. The low temperature state (ground state) of the system should have an open, low density structure like that of ice.
2. Linear hydrogen bonds can form between two molecules only when (a) the local configuration is open and (b) the participating molecules are properly oriented.
3. Increased local density with respect to the open structure must result in an increase in the (a) local energy and (b) the local entropy. The normal lowering of energy on increasing the number of neighbours is reversed in water due to the distortion of hydrogen bonds.

Hydrogen bonding, then, is fundamental to our understanding of water; as we saw in the previous section, the anomalous behaviour of the liquid would seem to be rooted in the desire to form an energetically favourable open hydrogen-bonded network.

2.7.2 Hydrogen bond geometry

Hydrogen bonds are not linear within the liquid system. Modig *et al.* (2003) have determined the typical HB configuration using a combination of experiment and *ab initio* calculation, as shown in Figure 2.9 and Table 2.9.

Cho *et al.* (1997) write that the proportion of hydrogen bonds in the liquid remains less that 5% (Cho *et al.*, 1996b) — though bonds are continuously breaking and reforming; however the experiments of Myneni *et al.* (2002) put the number of hydrogen bonds per molecule at 2.4–2.8, corresponding to at least 30% proportion of broken H-bonds.

R_{OO}	2.82 Å
r_{HO}	1.88 Å
θ_{bend}	12°

Table 2.9: Values for the lengths and angles depicted in Figure 2.9, as determined by Modig *et al.* (2003).

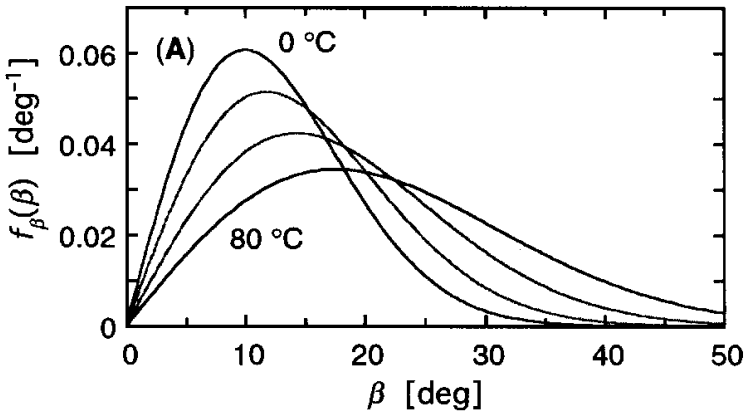

Figure 2.10: Distribution of hydrogen bond bending angles θ_{bend} ($\equiv \beta$ here) taken from Modig *et al.* (2003). The experimental curves shown represent temperatures of — from top to bottom — 0, 4, 15, 27, 50 and 80°C.

Pople (1951) noted much earlier that bond bending explains the *apparent* increase in the number of first nearest neighbour molecules over the figure of 4 for ice and also the filling of the region between first and second nearest neighbour shells at 3.5 Å as seen by Morgan and Warren (1938). Pople employed a statistical mechanical analysis of water using hydrogen bond bending. Using simple force constants of HB bending, he achieved a good reproduction of the radial distribution functions as such those which Morgan and Warren had obtained by experimental means.

Despite the directionality of the hydrogen bond appearing to be significant in inducing the tetrahedral structure of ice, the bond is more stable with respect to bond bending than with stretching; Espinosa *et al.* (1998) found that HB strength decays exponentially with distance. Indeed, the configurational criteria for the formation of a hydrogen bond is not well resolved, and is a judgement which must be made by the researcher. For example, Khan (2000) used values of R_{OO} = 3.10 Å and $\angle OHO$ = 146°, whereas Schwegler *et al.* (2000) used the more lax values of R_{OO} = 3.5 Å and $\angle OHO$ = 140°.

2.7.3 Polarisation & cooperative bonding

Frank (1958) tells of how bonding between water molecules promotes bonding be-

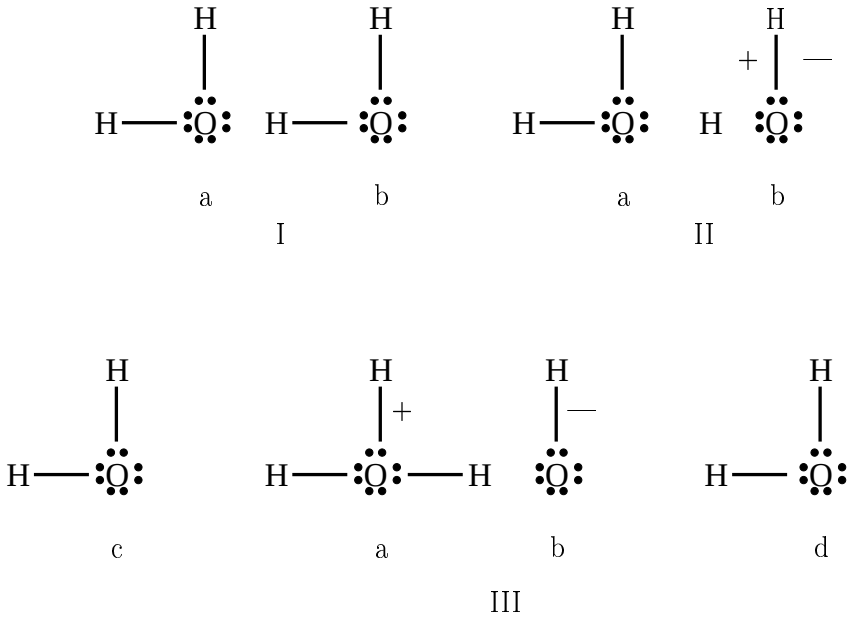

Figure 2.11: Cooperative effects in hydrogen bonding. Redrawn from Frank (1958).

tween the formed cluster and other molecules. For an illustration of this concept, see Figure 2.11. The covalent interaction between molecules a and b in structure III results in a greater charge separation in the donor molecule, thus encouraging interactions with other non-bonded molecules as represented in the figure by molecules c and d. Frank and Wen (1957) postulated that these cooperative bonding effects are seen in the liquid; water molecules form clusters which appear and dissolve together, promoting regions of high local order.

Tanaka (1998a) found by means of computer simulation that clustering behaviour is very different in the low density liquid (LDL) form to that in the high density liquid (HDL)[6]. According to Tanaka, clusters in the high density phase are disconnected, whereas the connectivity of clusters in the low density phase "spreads over the entire system".

More recently, Errington *et al.* (2002) found evidence for cooperative bonding behaviour in simulated water using the SPC/E potential[7]. There they studied the volume per molecule in ice-like water clusters. As the cluster size increased, the cluster showed a decrease in density up until some limiting size; beyond this size, the density of the cluster remained unchanged. Curiously, the SPC/E model for water uses rigid molecular constraints; there is no change in the intramolecular charge site geometry. Any cooperativity, then, would seem to have come about through many-body intermolecular effects and *not* from electronic polarisation.

[6]High and low density forms of liquid water are discussed in Section 2.8.2.
[7]The SPC/E potential for water is described in Chapter 4

The inclusion of molecular polarisation in empirical models for water is somewhat of an esoteric thing. The SPC/E potential of Berendsen *et al.* (1987) was intended to include some description of polarisation effects in the form of an effective potential. They essentially reparameterised the existing Simple Point Charge (SPC) model. The effect was to give a better description of the second nearest neighbour peak in the O-O radial distribution function. There has also been work to suggest that the Polarisable Point Charge (PPC) model gives a good description of liquid state properties (Svishchev *et al.*, 1996) and the liquid-vapour coexistence curve (Svishchev and Hayward, 1999).

Stern and Berne (2001) performed classical and path integral calculations using a flexible and polarisable model, simulating water in the liquid *and* the gas phase. The $\angle HOH$ angle was seen to *decrease* as the water entered the liquid phase, in contrast with experiment. Stern and Berne go on to comment that polarisation from surrounding molecules encourages the water molecule to form a larger dipole moment, and hence a smaller $\angle HOH$; yet the angle should become larger, since the liquid adopts something of the tetrahedral character seen in ice.

2.7.4 Model types

We have seen the importance of hydrogen bonding in the determination of the structure of water, but how are hydrogen bonded structures arranged in the liquid? The different types of proposed models for bulk water have been summarised by Frank (1972), which fall into three categories. We shall describe their qualitative features here.

Mixture

Here the liquid contains pockets of bonded and non-bonded molecules; when ice melts, it is pictured as forming a liquid containing “icebergs”.

Uniformist

Uniformist models are concerned with hydrogen bond *bending* rather than breaking, leading to a remaining but distorted H-bond network.

Interstitial

Interstitial models are concerned with the notion that upon heating molecules fall out of the tetrahedrally coordination lattice structure and occupy vacancies between lattice sites.

Note that the picture of the real liquid which we have leaned towards so far is of the *interstitial* type.

2.8 Thermodynamic approach

So far we have considered the behaviour of water from the perspective of *microscopic* structure. For the sake of completeness, we now consider briefly the interpretations of the density maximum from a more *macroscopic* perspective.

2.8.1 Stability limit conjecture

It has been found that some thermodynamic quantities appeared to diverge below the temperature of homogeneous nucleation T_{N}, below which water always crystallizes. The correspondance between T_{N} and the temperature at which the liquid becomes mechanically unstable led to proposals that it is the approach towards the spinodal line of mechanical instability which is behind behavioural anomalies (Speedy and Angell, 1976; Speedy, 1982b,a, 1987).

Defining the isothermal compressibility κ_T and the thermal expansivity α

$$\kappa_T \equiv -\frac{1}{V}\left(\frac{\partial V}{\partial P}\right)_T \tag{2.10}$$

$$\alpha \equiv \frac{1}{V}\left(\frac{\partial V}{\partial T}\right)_P \tag{2.11}$$

then for a particular path $P_s(T)$ which represents the locus of points for which the liquid becomes mechanically unstable,

$$\alpha = \frac{1}{V}\left(\frac{\mathrm{d}V_s}{\mathrm{d}T}\right) + \kappa_T\left(\frac{\mathrm{d}P_s}{\mathrm{d}T}\right). \tag{2.12}$$

Under normal conditions, the stability criterion is met:

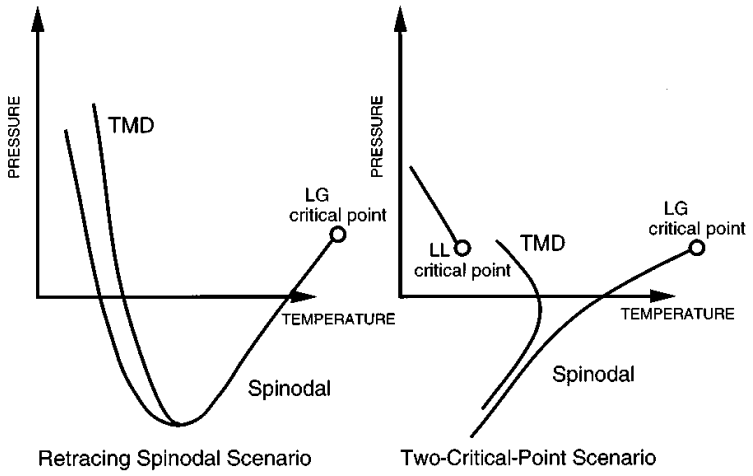

Figure 2.12: Schematic representation of the reentrant spinodal and liquid-liquid critial points scenarios. Taken from Sastry *et al.* (1996).

$$\left(\frac{\partial P}{\partial V}\right)_T < 0 \quad \text{or} \quad \kappa_T > 0. \tag{2.13}$$

However as $P \to P_s$, $\left(\frac{\partial P}{\partial V}\right)_T \to 0$ and hence $\kappa_T \to +\infty$.

Since $\left(\frac{\mathrm{d}V_s}{\mathrm{d}T}\right)$ and $\left(\frac{\mathrm{d}P_s}{\mathrm{d}T}\right)$ remain finite except at singular points on the $P_s(T)$ line, Equation 2.12 tell us that

$$\frac{\alpha}{\left(\frac{\mathrm{d}P_s}{\mathrm{d}T}\right)} \to +\infty. \tag{2.14}$$

This tells us that α and $\frac{\mathrm{d}P_s}{\mathrm{d}T}$ have the same sign close to the spinodal pressure P_s.

Under the *stability limit conjecture* (SLC), pressure decreases with temperature and goes through a minimum in the negative pressure region of the phase diagram. Since $\frac{\mathrm{d}P_s}{\mathrm{d}T}$ changes sign, α must do the same; there must therefore be a path such that $\alpha(P,T) = 0$ — the density maximum (or minimum). Further, if the TMD line remains negatively sloped in the (P,T) plane, then its intersection with the liquid-gas spinodal must render the spinodal line reentrant[8]; the TMD line must intersect the spinodal at the *minimum* in the (P,T) plane. The reentrant spinodal is illustrated in Figure 2.12.

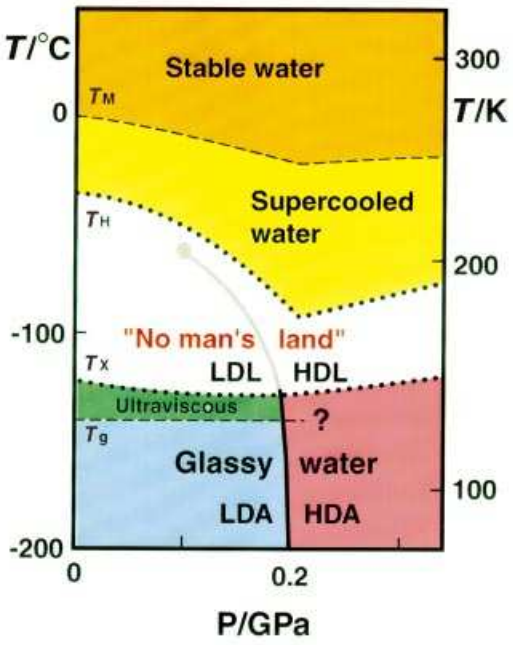

Figure 2.13: Phase diagram of water showing the hypothesised second critical point. Taken from Stanley *et al.* (2000).

2.8.2 Liquid-liquid phase transition

Poole *et al.* (1992, 1993) studied water by simulation, and found inflections in isotherms of the phase diagram which increased in magnitude deeper into the supercooled region, perhaps providing evidence for a *second critical point* in supercooled water; below this critical point, it has been postulated that there exists two forms of liquid water – the High Density Liquid (HDL) and Low Density Liquid (LDL). A schematic diagram of this idea is shown in Figure 2.12, and a phase diagram showing the second critical point is shown in Figure 2.13. Though the second critical point itself is thought to lie in the supercooled region of the phase diagram, the anomalous behaviour of water at ambient pressure and temperature may be attributed to the onset of critical behaviour in the liquid.

Experimental analysis of the HDL and LDL forms of supercooled water are not possible, since the second critial point lies below the temperature at which homogenous nucleation of the liquid into solid ice begins to occur. However, some insight may be achieved by noting that the HDL–LDL transition line may be seen as a continuation of the High Density Amorphous (HDA) and Low Density Amorphous (LDA) phases of ice into the supercooled liquid region of the phase diagram; indeed, the

[8]The spinodal line must retrace back into positive pressures.

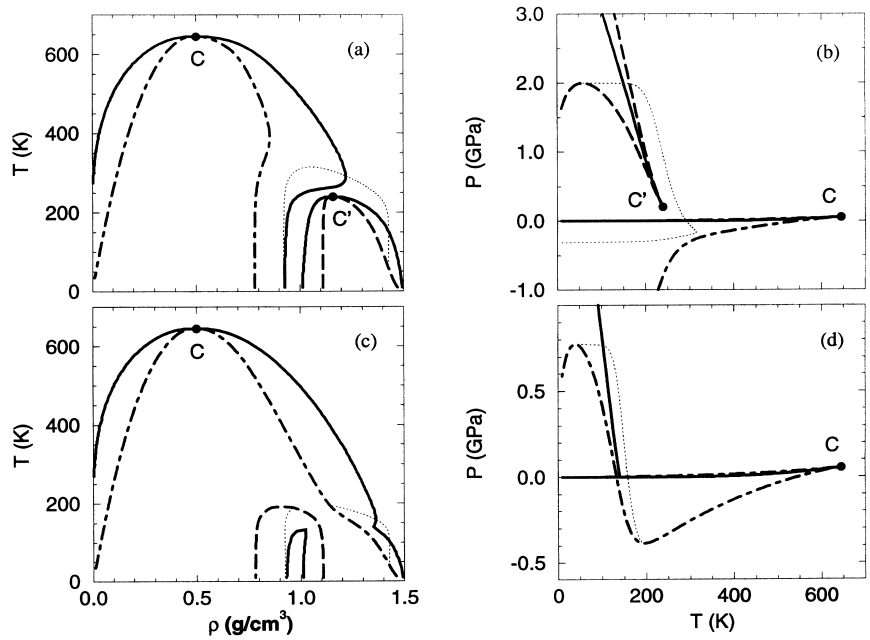

Figure 2.14: Coexistence curves and P-T phase diagrams, taken from Poole *et al.* (1994). Coexistence curves are shown as solid lines, spinodal lines as dashed and dot-dashed, and lines of density maxima are shown as fine dotted lines.

HDA–LDA has been achieved between the two amorphs at temperatures of 77 K and 140 K, with the transition seen to happen at about 200 MPa (Mishima, 1994). Mishima noted the absence of any intermediate amorphous states between the LDA and HDA phases; if there is a clear phase boundary just below the glass transition temperature, it is reasonable to suppose that there may be a similar boundary just above it.

In the same year came a theoretical derivation of liquid-liquid phase separation at low temperature. Poole *et al.* (1994) constructed a free energy of the form:

$$A = A_{\mathrm{VDW}} + 2A_{\mathrm{HB}}. \tag{2.15}$$

They followed the practice of distinguishing two strengths of hydrogen bond: strong and weak, with energies $\epsilon_{\mathrm{weak}} = 0$ and $\epsilon_{\mathrm{strong}} = \epsilon_{\mathrm{HB}} < 0$. It was found that for $|\epsilon_{\mathrm{HB}}| > 16.5\,\mathrm{kJ\,mol^{-1}}$, the liquid-gas coexistence curve splits in two, with a region of instability lying between them as illustrated in Figure 2.14. There is evidence, then, that two phases of liquid water exist in the supercooled region.

Further experimental evidence came from observations of the melting curves of various phases of *heavy* water ice (Mishima, 2000). It was found that one phase demonstrates a smooth melting curve, whereas the curve becomes kinked for phases with a lower melting temperature at a given density, as shown in Figure 2.15.

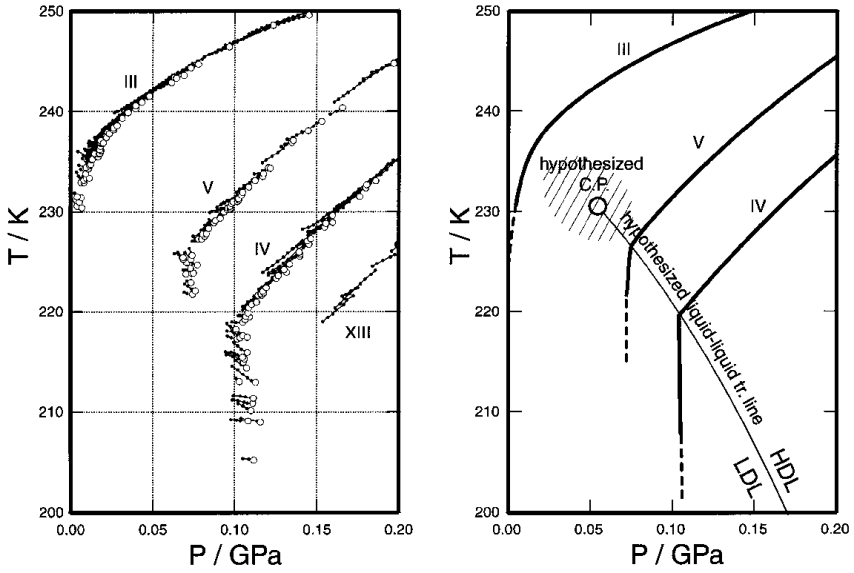

Figure 2.15: The melting curves of D_2O ices (III,V,IV,XIII) taken from Mishima (2000), from the region of 0–0.2 GPa pressure and 200–250 K temperature. Left: the experimental data, with the open circles marking the onset of a change in temperature. Right: schematic diagram representing the hypothesised HDL–LDL transition line and the second critical point.

It is the TIP5P model for water[9] which is employed for the molecular dynamics calculations presented here. We shall therefore take a moment to note the work of Yamada *et al.* (2002). These authors have found evidence for a liquid-liquid critical point in TIP5P water by observing inflections in $P - T$ curves, as shown in Figure 2.16. It is also worth noting — recalling the stability limit conjecture — that the spinodal line which they construct is not reentrant, and does not intersect the TMD line. These conditions are not required by the singularity-free interpretations, to which we turn our attention now.

2.8.3 Singularity-free interpretation

Later, Sastry *et al.* (1996) presented an interpretation of the behaviour of water which was free of any singular behaviour which came as a result of the SLC. From thermodynamic arguments, they derive the expression given in Equation 2.16:

$$\left(\frac{\partial \kappa_T}{\partial T}\right)_{P,\mathrm{TMD}} = \frac{1}{v}\frac{\partial^2 v/\partial T^2}{(\partial P/\partial T)_{\mathrm{TMD}}} \tag{2.16}$$

where v is the volume per particle. This equation indicates that a negatively sloped

[9]Described in Chapter 4

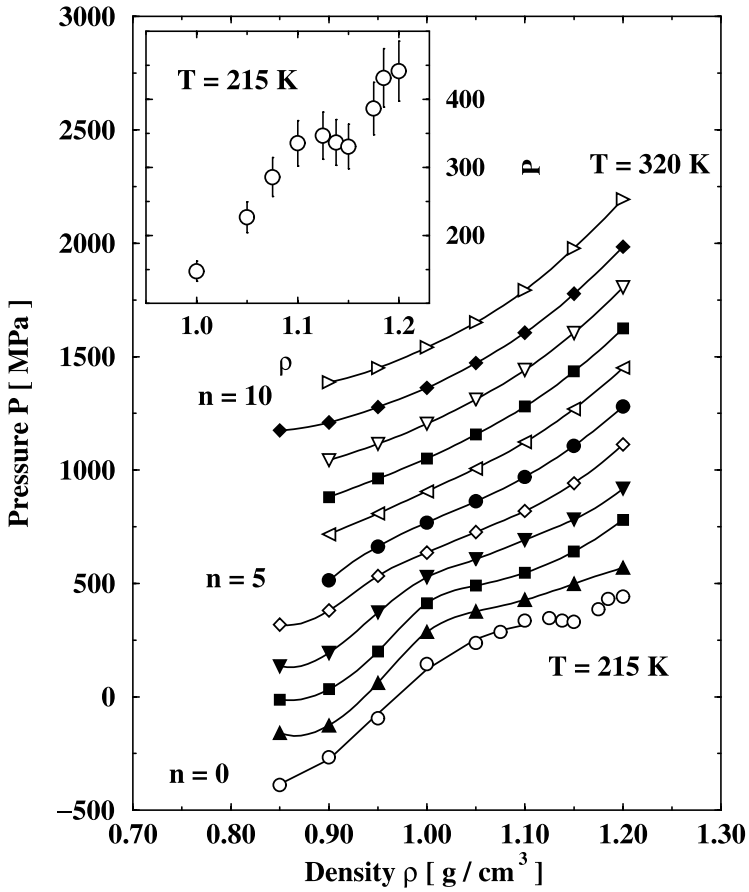

Figure 2.16: Pressure as a function of temperature for simulated water using the TIP5P potential. Each curve is shifted upwards by $n \times 150$ MPa for clarity. Inflections are evident until the lowest temperature, perhaps where a phase coexistence region has set in. Taken from Yamada *et al.* (2002).

TMD in the (P, T) plane gives rise to an increasing isothermal compressibility at constant pressure as temperature is decreased. The increase in compressibility, then, does not necessarily point to any singular behaviour. After intersecting the line of compressibility maxima, the TMD *retraces*, or takes on a positive slope in the (P, T) plane — which is consistent with the picture for the liquid-liquid phase transition hypothesis shown in Figure 2.12.

2.9 Nuclear quantum effects

We saw in Section 2.2 that $2s^2$ electrons from the oxygen atoms form hybrids with electrons in the $2p^4$ state. They therefore become valence electrons and hence chemically active; the only two remaining core electrons are those in the $1s^2$ state in the oxygen atom.

Considering, then, that 80% of the electrons in the water molecule are chemically active, it is striking to note the radical shift in the TMD upon isotopic substitution. The switch from *light* to *heavy* water generates a dramatic change in the TMD, even though the electronic configuration remains the same! Indeed, there is experimental verification from X-ray diffraction experiments that the electron densities in H_2O and D_2O are virtually indistinguishable (Neuefeind *et al.*, 2002).

Heavy water is slightly more ordered than light water at the same temperature (Tomberli *et al.*, 2000). Further, Némethy and Scheraga (1964) point out that the inflated viscosity, melting point, TMD and heat capacity in heavy water serve to indicate a higher degree of structural order than exists in light water at the same temperature; deuterium bonds would appear to be stronger. There is evidence from crystallographic data that the hydrogen and deuterium bond lengths the respective waters are almost identical (Megaw, 1934), yet the maximum densities of light and heavy water differ; the maxima of density and corresponding temperatures are given in Table 2.10. Increasing the mass on the ends of two arms of the water molecule can conceivably have two effects. The first is that the resultant dynamics of those heavier particles might be slower when acted upon by the same forces as present in the light water system. The second is quantum mechanical in origin: the magnitude of quantum delocalisation decreases with increasing mass.

So, then, it would appear critical to include nuclear quantum effects in calculations of the water system. This has been done for bulk water by a number of researchers using a range of methods for handling electronic and nuclear behaviour (Billeter *et al.*, 1994; Kuharski and Rossky, 1985; Del Buono *et al.*, 1991; Lobaugh and

	H_2O	D_2O	T_2O
Max. of density ($g\,cm^{-3}$)	1.0[a]	1.11[a]	1.22[a]
TMD (°C)	3.98[b]	11.2[c]	13.4[d]

[a] Franks (2000)
[b] Watanabe (1991)
[c] Kirshenbaum (1951)
[d] Goldblatt (1964)

Table 2.10: The effect of isotopic substitution on the temperature of maximum density.

Voth, 1997; Guillot and Guissani, 1998; Shiga *et al.*, 2000; Stern and Berne, 2001). In particular, Kuharski and Rossky (1985) found that the inclusion of quantum effects had a similar effect on the liquid structure as an increase in temperature of approximately 50 K; hydrogen bonds showed a greater degree of bending, and further they saw an increase in the number of molecules situated at a radial distance of $\simeq 3.4$ Å at the expense of those at the tetrahedral value of $\simeq 4.5$ Å. Calculations performed with *heavy* water demonstrated structural characteristics *between* those found classical and path integral simulations of light water. Kuharski and Rossky further note that it is most the *orientational* characteristics of molecules which are affected by nuclear quantum properties. Del Buono *et al.* (1991) performed similar calculations using other empirical potentials, demonstrating similar relaxations in hydrogen bond linearity, and an outward movement and broadening of the second neighbour peak upon activation of the path integral treatment.

2.10 Summary

The isolated water molecule owes its V-shaped geometrical form to p-type covalent bonding; molecules form dimers through hydrogen bonding — a bond with covalent characteristics in which electrons involved in *intramolecular* covalent bonding are now also taking part in covalent bonding with the oxygen atom of the second molecule.

The hydrogen bond is directionally dependent, preferring to exist with a hydrogen atom lying on a straight line between two oxygen atoms. This directional dependence is thought to play a key part in the density anomaly below 4°C at 1 atm by encouraging the formation of an open tetrahedral-like structure; at this pressure and temperature range, water *expands* as it is cooled contrary to simple liquid behaviour.

The four-fold symmetry of the molecule is thought to be responsible for the tetra-

hedral structure which persists in the liquid phase. As water is heated towards the density maximum, molecules from the second neighbour shell move from a radial distance of about 4.5 Å to about 3.4 Å; they become *interstitial* molecules, filling vacancies in the tetrahedral lattice. The density maximum itself is thought to come about as the result of a competition between the formation of interstitial molecules and thermal expansion familiar in simple liquids.

It is not only thermal fluctuations which induce the growth of the 3.4 Å neighbour peak; there is evidence from computer simulation that nuclear quantum fluctuations have a significant impact, creating structures consistent with those of a sizeable temperature increase in the liquids. Electrons, owing to their very much smaller mass, display more pronounced quantum mechanical behaviour in general; this would seem to be of reduced significance, however, when considering the location of the density maximum — the TMD shows a significant shift when exploring isotopes of hydrogen. Further, the maximum density of *heavy* water is approximately 10% greater than that seen in light water. Nuclear quantum fluctuations, then, would seem to be playing a key role as regards the liquid water structure.

Chapter 3

Molecular Dynamics

3.1 Introduction

Molecular dynamics (MD) aims to simulate real systems as closely to nature as possible on the microscopic scale. Of course, we must look to experiment to validate simulation data. However, if simulation proves reliable, molecular dynamics affords access to a wealth of information about a system which cannot necessarily be obtained from experiment; molecular structure, for example, may be visualised easily.

During the course of a molecular dynamics run, positions and velocites are propagated according to Newton's equations of motion. In doing so, possible phasespace configurations are explored. We may extract structural, dynamical and thermodynamical information by sampling those phasespace configurations.

In this chapter we will look at the ingredients of molecular dynamics, and the information which it affords.

Section 3.2 looks at the fundamental building blocks of molecular dynamics simulation. Section 3.3 concerns required lengths for molecular dynamics runs, and Section 3.4 discussed serial correlation between timesteps. The thermostat emploted to maintain the water system at the desired temperature is described in Section 3.6, and the method by which rigid molecular constraints were applied is given in Section 3.7. Sections 3.8 to 3.11 describe some quantities which are measureable from molecular dynamics simulation, including water specific structure functions as presented in later chapters. Section 3.12 brings the chapter to a close.

3.2 Fundamentals

We first take a walk through issues relating to the fundamental nature of molecular dynamics simulation.

3.2.1 Ergodic hypothesis

The *ensemble average* is an average taken on the assumption that all microstates are equally accessible. The *ergodic hypothesis*[1] is central to molecular dynamics and says that if the phasespace trajectory of a system passes through every point in phase space without bias, then time averages become equivalent to ensemble averages; that is, the phasespace trajectory samples possible microstates of the system without bias. Mathematically,

$$\overline{A} = \langle A \rangle_{\text{ens}} \tag{3.1}$$

where $\overline{A}$ denotes the time average of some quantity of interest, and $\langle A \rangle_{\text{ens}}$ denotes the ensemble average.

We must then ensure that during a molecular dynamics run we have generated a suitable representative sample of phasespace configurations. We shall pick up on this idea again in later sections.

3.2.2 Initialisation & equilibration

While it might seem desirable to initiate the water system with random positions, this is a dangerous practice. In this case it is easy for particles to be unphysically close and feel exceedingly high forces, which may potentially result in numerical instability. For this reason, molecules were set up on a regular face centred cubic (FCC) lattice[2].

Initial velocities were chosen from the Maxwell-Boltzmann distribution seen in an equilibrium system. Having assigned velocities from the *normal* distribution and rescaled such that the linear momentum was zero, the velocities were rescaled to the desired temperature on the assumption of no constraints:

[1] The ergodic hypothesis is discussed by Frenkel and Smit (1996), pp. 15–17.
[2] The reason for a specifi cally FCC lattice is discussed in Subsection 3.2.3.

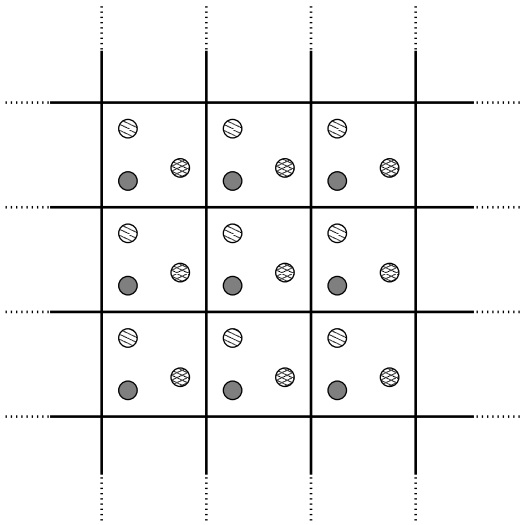

Figure 3.1: Graphical demonstration of periodic boundary conditions in two dimensions. The central cell is the simulation cell, and those which surround it are periodic images of the simulation cell. The periodic image cells extend out to infinity in each dimension.

$$\boldsymbol{v}_i' = \boldsymbol{v}_i \sqrt{\frac{3NT_{\text{desired}}}{\sum_{i=1}^{N} m_i v_i^2}} \tag{3.2}$$

Equation 3.2 is not quite accurate for a system of constrained water molecules, yet it is satisfactory since the system is yet to undergo an *equilibration phase* — a period of time must be allowed at the start of a simulation to allow the system to come to a state of equilibrium before meaningful measurements can be taken of the system properties. An equilibrated system will not care how it was started. Only once observables have ceased to show any systematic drift with simulation time may we begin the *production phase* over which quantities are sampled.

3.2.3 Periodic boundary conditions

In the simulation of bulk properties, it is desirable to use period boundary conditions (PBC) to remove surface effects. Under this scheme, the simulation cell is surrounded by cells which are identical to it, as shown in Figure 3.1. Atoms inside the simulation cell we shall call *real* atoms, and atoms in the image cells we shall call *image* atoms. If an atom was to leave the simulation cell, an *image* atoms would come into the simulation cell from the opposite side.

The system being simulated is known to be large enough when the system properties have converged with respect to particle number; there is no point in simulating larger

systems than is necessary if no significant improvement can be seen in the results.

Some output properties such as the mean square displacement require "unpacked" atomic positions — the positions of those atoms which were initially in the simulation cell at some later time through the simulation. From an implementational perspective, it is therefore desirable to maintain a vector for each atom which translates from the simulation cell to the image cell in which it currently resides.

Commensurate particle numbers

Repeating the simulation cell in all dimensions in the way described above carries with it a restriction of the numbers of atoms or molecules which can be included in a simulation. Choosing an inappropriate number of particles can result in the presence of artifical defects upon freezing; the otherwise preferred lattice structure just cannot fit correctly into the simulation cell.

Argon, for example, forms a 4-atom FCC unit cell. A suitable number of argon atoms for simulation in a cubic box would therefore be $3 \times 3 \times 3 \times 4 = 108$. Ice Ih forms an eight-molecule orthorhombic unit cell (Röttger *et al.*, 1994). Consequently, for water in a cubic simulation cell, a suitable number of molecules would be $3 \times 3 \times 3 \times 8 = 216$ molecules, or 648 atoms — double the number in the FCC configuration. It is for this reason that a compressed FCC lattice was used as the starting configuration.

Whilst solid water is not simulated here, simulations are performed close the the solid-liquid phase boundary; a *commensurate* number of particles was always used for the sake of prudence. Indeed, *short-ranged* order persists in the liquid phase.

Minimum image criterion

The *minimum image criterion* is used when calculating the separation between atoms. It says that out of all atoms in our infinitely periodic system, we use that which gives the smallest separation. This is demonstrated graphically in Figure 3.2.

3.2.4 Choice of ensemble

The most simple approach to molecular dynamics simulation would be to use constant particle number, simulation cell volume and energy — the *canonical* or "NVE" ensemble. This, however, is somewhat unphysical. In the real world, water exists

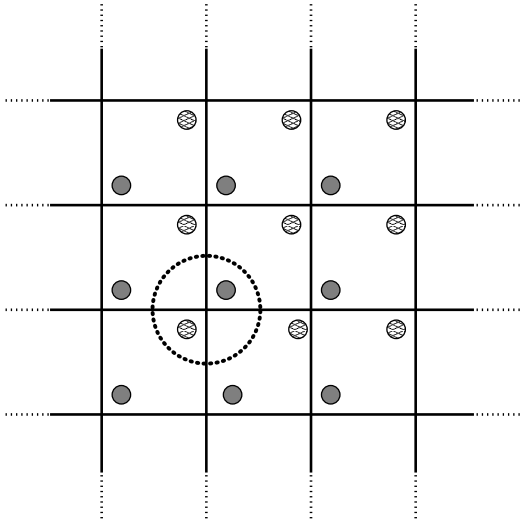

Figure 3.2: Illustration of the minimum image criterion. The separation between the real and image atoms within the circle is smaller than the distance between the equivalent real atoms in the simulation cell.

in thermal equilibrium with its surroundings; it is coupled to a heat bath of constant temperature. The *canonical* or "NVT" ensemble, then, employs constant particle number, volume and *temperature*. Indeed, the NVE ensemble provides no means for the temperature control which is so desired when analysing the dependence of system properties with temperature. It is further possible to take a further step closer to real life, and replace the constancy of volume with that of *pressure*.

For ease of computation, the NVT ensemble was chosen for the present work. Indeed, constant volume simulation has the advantage of allowing direct control over the density of the system; in Chapter 7 we shall find it desirable to study changes the water structure with respect to such changes in density.

3.2.5 Reduced units

MUDPIES performs calculations using quantities in *atomic* units. *Reduced* units keep numbers of order unity and hence the risk of numerical inaccuracies is reduced; the use of atomic units performs this function.

Base units of mass, length and temperature are defined in Table 3.1, and units derived from these are given in Table 3.2.

Quantity	Symbol	Unit	
Mass	M	Electron mass	m_e
Length	L	Bohr	$a_0 = \hbar/\alpha c m_e$
Temperature	T		$m_e \alpha^2 c^2 / k_\mathrm{B}$

Table 3.1: Mass, length and temperature in atomic units. α is the fine structure constant, m_e is the electron rest mass, c is the speed of light and a_0 is the Bohr radius. The symbols are for use in conjuction with Table 3.2.

Quantity	Reduced unit	Quantity	Reduced unit
Density	L^{-3}	Volume	L^3
Time	$L\sqrt{M/k_\mathrm{B}T}$	Velocity	$\sqrt{k_\mathrm{B}T/M}$
Energy	$k_\mathrm{B}T$	Force	$k_\mathrm{B}T/L$
Momentum	$\sqrt{Mk_\mathrm{B}T}$	Pressure	$k_\mathrm{B}T/L^3$

Table 3.2: Reduced units of various quantities as derived from base units of mass, length and temperature in atomic units. M, L and T are mass, length and temperature in atomic units, as given in Table 3.1. e is the charge on the proton.

3.2.6 Centre of mass constraint

To ensure that the system was held in the laboratory frame, particle velocities were rescaled on initialisation such that the centre of mass momentum in each dimension was held at zero:

$$m_i \boldsymbol{v}_i' = m_i \boldsymbol{v}_i - \frac{1}{N} \sum_{i=1}^{N} m_i \boldsymbol{v}_i. \tag{3.3}$$

Thereafter, forces were rescaled such that there was no net force on the centre of mass of the system:

$$\boldsymbol{f}_i' = \boldsymbol{f}_i - \frac{1}{N} \sum_{i=1}^{N} \boldsymbol{f}_i. \tag{3.4}$$

A rescaling of this type at each timestep becomes important when we employ the thermostatting techniques of Section 3.6; Indeed, the only function of Equation 3.4 thoughout the remainder of the simulation is to ensure that the *Langevin forces* — to be introduced there in Section 3.6 — sum to zero at each timestep; all internal forces due to the intermolecular potential, for example, sum to zero.

3.2.7 Integrating the equations of motion

The *Verlet* algorithm (Verlet, 1967) can be obtained by subtracting a backwards-in-time Taylor expansion from one which is forwards-in-time:

$$\boldsymbol{r}(t+\Delta t) = 2\boldsymbol{r}(t) - \boldsymbol{r}(t-\Delta t) + \ddot{\boldsymbol{r}}(t)\Delta t^2 + O(\Delta t^4). \tag{3.5}$$

where Δt is the integration timestep.

Equation 3.5 clearly does not make explicit use of atomic velocities. The velocity information is implicit in the form of positions at two previous times. Position Verlet has one advantage in that it is accurate to third order, despite its third order term being zero. It does, however, have two important drawbacks. Firstly, it is not self-starting; an Euler step must be performed for the first timestep so as to generate the two positions required by Position Verlet. Also, the lack of availability of atomic velocities renders the calculation of quantities which are dependent upon the phasespace configuration very cumbersome; this algorithm focusses on one of two dimensions per atom in phase space.

Defining

$$\dot{\boldsymbol{r}}(t) = \frac{\boldsymbol{r}(t+\Delta t) - \boldsymbol{r}(t-\Delta t)}{2\Delta t} \tag{3.6}$$

we can find a much better algorithm to work with which retains the accuracy of Position Verlet - the *Velocity Verlet* algorithm (Swope *et al.*, 1982):

$$\boldsymbol{r}(t+\Delta t) = \boldsymbol{r}(t) + \dot{\boldsymbol{r}}(t)\Delta t + \ddot{\boldsymbol{r}}(t)\frac{\Delta t^2}{2} \tag{3.7a}$$

$$\dot{\boldsymbol{r}}(t+\Delta t) = \dot{\boldsymbol{r}}(t) + [\ddot{\boldsymbol{r}}(t) + \ddot{\boldsymbol{r}}(t+\Delta t)]\,\frac{\Delta t}{2} \tag{3.7b}$$

Velocity Verlet has another strong advantage: we do not need to worry about the possibility that periodic boundary conditions were applied to an atom at the previous iteration. Such a situation under Position Verlet yields an apparent very high velocity of an atom!

Setting the timestep size

When setting the length of the timestep there is a balance to be struck. If the timestep is too long, the integration of the equations of motion will become unstable. Conversely, if the timestep is too small then calculations will take a good deal longer for no extra gain. A very small timestep may also result in numerical inaccuracies due to rounding errors! The method by which the optimum timestep was determined is given in Section 3.5.

3.3 Simulation times

The required simulation should be long enough to sample a representative proportion of phasespace, and this is in part determined by the measured property of interest. Different quantities such as temperature and pressure converge at different rates. We are presently interested in local structure, and hence production times — the simulation time over which quantities were measured — were sufficient to reduce noise in relative frequency plots to a tolerable level. A production time of 75 ps was found to be sufficient for this. A more general rule of thumb when deciding on a ballpark production time is that it should be greater than ten times the *Langevin damping time,* to be introduced in Section 3.6.

The time given for the system to come to equilibrium was 15 ps. The production phase was conducted in 15 ps segments; noting the lack of significant variation in the radial distribution functions[3] between the segments demonstrated that the system was indeed showing an equilibrium structure.

3.4 Statistics and correlation

In molecular dynamics, positions and velocities are propagated using deterministic equations of motion. The degree of *serial correlation* between data from consecutive timesteps is therefore very high. Here we shall explore methods of analysing and correcting for such correlations.

[3] To be introduced in Section 3.9.

3.4.1 Autocorrelation function

The *correlation function*[4] is a function whose modulus varies between 0 and 1 for low and high serial correlation respectively.

Defining

$$\Delta A = A - \langle A \rangle \tag{3.8a}$$

$$\Delta B = B = \langle B \rangle \tag{3.8b}$$

the correlation function is given by

$$C_{AB} = \frac{\langle \Delta A \, \Delta B \rangle}{\sigma(A) \, \sigma(B)} \tag{3.9}$$

where $\sigma(A)$ and $\sigma(B)$ are the RMS fluctuations on A and B respectively. In the case where A and B are uncorrelated, the numerator reduces to the product $\langle \Delta A \rangle \, \langle \Delta B \rangle$, which is *zero*.

A and B may represent the same quantity with some time interval between them, in which case we speak of an *autocorrelation* function; the numerator $\langle \Delta A(t) \Delta A(t + t') \rangle$ is averaged over all time origins. The autocorrelation function provides a measure of the timescales over which serial correlations decay to zero. An important example is the *velocity autocorrelation function* (VACF):

$$C_{vv}(t) = \frac{1}{N} \lim_{T \to \infty} \sum_{i=1}^{N} \int_0^T \frac{\boldsymbol{v}_i \left(t'\right) \cdot \boldsymbol{v}_i \left(t' + t\right)}{\boldsymbol{v}_i \left(t'\right) \cdot \boldsymbol{v}_i \left(t'\right)} \mathrm{d}t' \tag{3.10}$$

where the $\boldsymbol{v}_i$ are single particle velocities; we average over all atoms in the system to improve the statistics. An example is shown in Figure 3.3, which indicates that it takes approximately three times longer for oxygen correlations to die away than is the case for hydrogen.

3.4.2 Data blocking

When taking results from MD simulation we must be careful not to *oversample* the data, because not every phasespace configuration contributes entirely new informa-

[4] Correlation functions are discussed by Allen and Tildesley (1987), pp. 58–64.

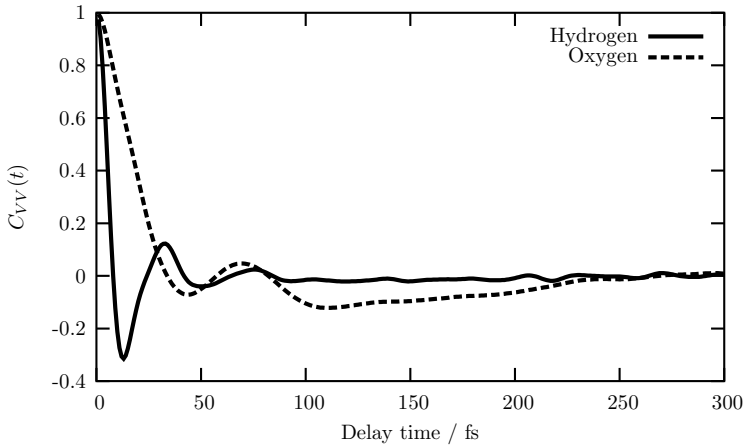

Figure 3.3: Velocity autocorrelation functions for hydrogen and oxygen motion in TIP5P water at $\simeq 277\,\mathrm{K}$. The density was $\rho = 1.0\,\mathrm{g\,cm^{-3}}$.

tion to the average. While the mean — with its status as an unbiased estimator — will be unaffected, the *standard error* on the mean may be significantly underestimated.

Friedberg and Cameron (1970) defined a quantity called the *statistical inefficiency* s:

$$s = \lim_{\tau_\mathrm{b}\to\infty} \frac{\tau_\mathrm{b}\,\sigma^2\left(\langle A\rangle_b\right)}{\sigma^2(A)} \tag{3.11}$$

where τ_b is the block "time" — the number of timesteps which form each of the blocks. It represents the number of timesteps which must be performed in order to arrive at a phasespace configuration which contributes entirely new information to the average. Once s is known, the standard error on the mean may be estimated through:

$$\delta\left\langle A\right\rangle_\mathrm{run} = \left(\frac{s}{\tau_\mathrm{run}}\right)^{\frac{1}{2}} \times \sigma(A). \tag{3.12}$$

where τ_run is the number of samples which constitute the entire run. Moreover, s affords a handle a suitable number of timesteps between phasespace samples taken from an MD run. While it is desirable to take a sample as frequently as possible to minimise the MD run length, it would be insensible to take a sample at every timestep. This would result in a large volume of highly correlated data; moreover, there would be a good deal of computational effort wasted in doing so. A good rate of output, then, would be every s timesteps, with s representing the smallest statistical inefficiency among the output quantities of interest. Here we use a time of 30 fs between output samples.

A similar method has been reported by Flyvbjerg and Petersen (1989) which affords an estimate of the *uncertainty in the uncertainty of the mean*, however it is the method of Friedberg and Cameron (1970) which we use here.

3.4.3 Structure functions

Though data blocking analyses of the types described above are essential if we are not to underestimate error bars on time averaged *scalar* quantities, we do not need to worry so much when calculating structure functions such as the radial distribution function — to be met later — which divide quantities such as particle number into bins of different radii from a molecule, for example. The mean is an unbiased estimator, and hence the result of adding too many contributions to a structure function is *not* to make the mean value in a given bin systematically incorrect; rather it serves to speed the smoothing of the resultant curve or surface.

3.5 Vibrational properties

Recall the correlation function from Section 3.4 (unnormalised here):

$$C(t) = \int_{-\infty}^{\infty} \mathrm{d}t' A\left(t'\right) B\left(t'+t\right) \tag{3.13}$$

The convolution theorem tells us that

$$\hat{C}(\omega) = \hat{A}^{*}(\omega)\hat{B}(\omega) \tag{3.14}$$

where hats denote Fourier transforms. Hence the Fourier transform of the velocity autocorrelation function gives us a handle on the characteristic frequencies of motion in the system, and is "proportional to the density of normal modes in a purely harmonic system" (Allen and Tildesley, 1987).

Figure 3.4 shows the Fourier transform of the VACF separately for oxygen and hydrogen atoms; integration timesteps and Langevin damping times[5] used are given in Tables 3.3 and 3.4.

[5] Langevin damping times are introduced in Section 3.6.

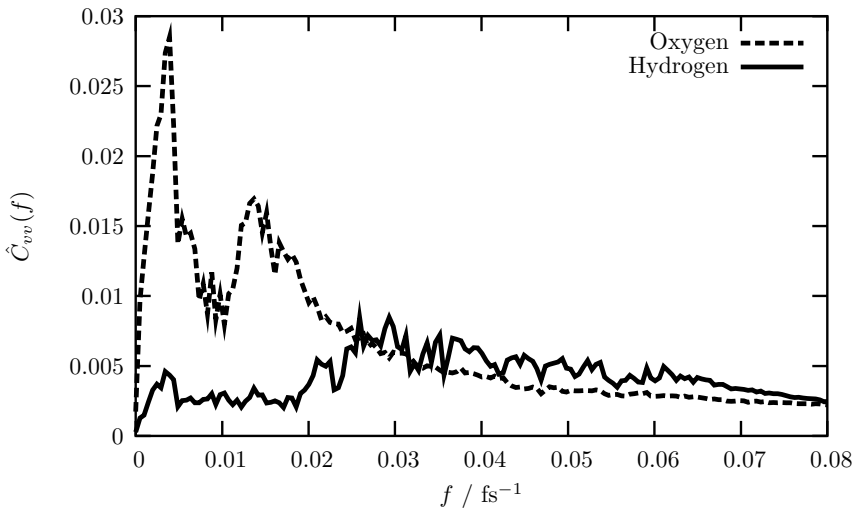

Figure 3.4: Fourier transformed velocity autocorrelation function for a system of light water at T = 275 K. This information is useful for the determination of the optimal integration timestep and Langevin damping time. The density was ρ = 1.0 g cm^{-3}.

Water type	Highest freq. mode / fs^{-1}	Period / fs	Integration timestep / fs
Light	0.06	17	2
Heavy	0.03	33	3

Table 3.3: Integration timestep derived from the Fourier transformed velocity autocorrelation functions, for temperatures $\simeq$ 277 K.

Water type	Lowest freq. mode / fs^{-1}	Period / fs	Langevin time / fs
Light	0.003	333	3500
Heavy	0.002	500	5000

Table 3.4: Langevin damping times derived from the Fourier transformed velocity autocorrelation functions. Temperatures are those calculated in the microcanonical ensemble, and are presented with RMS fluctuations.

3.6 Thermostat

In order to simulate a system in the canonical ensemble — with constant particle number, volume and temperature — we require a thermostat of some description to ensure that the temperature averages to the desired value. Here we discuss how this was achieved.

3.6.1 Temperature and temperature fluctuation

We demand two things of a thermostat algorithm. Firstly, it must hold the desired mean value of temperature. Secondly, we look for the same fluctuation of instantaneous temperature as is predicted by statistical mechanics.

The expected instantaneous temperature fluctuation may be obtained as follows. We start by noting that the instantaneous temperature may be found from:

$$\frac{1}{2}\sum_{i=1}^{N} m_i v_i^2 = \frac{\nu}{2} k_{\mathrm{B}} T \tag{3.15}$$

where N is the particle number and ν is the number of degrees of freedom. Note that a system of N atoms of which rigid water molecules are constructed has $2N - 3$ degrees of freedom, having substracted three to account for the centre of mass constaint of Subsection 3.2.6. If all the particles have the same mass, we may write

$$T = \frac{m}{\nu k_{\mathrm{B}}} \sum_i v_i^2 \tag{3.16}$$

and the mean square fluctuation in temperature may be written as

$$\Delta T^2 = \sum_{i=1}^{N} \left[\frac{\partial T}{\partial (v_i^2)}\right]^2 \Delta (v_i^2)^2. \tag{3.17}$$

To find the mean square deviation of speeds, we note that

$$\Delta (v_i^2)^2 = \left\langle \left(\Delta v^2\right)^2 \right\rangle = \left\langle \left(v^2\right)^2 \right\rangle - \left\langle \left(v^2\right) \right\rangle^2 \tag{3.18}$$

and

$$\left\langle \left(v^2\right)^2 \right\rangle = \frac{\int_0^\infty v^4 n(v)\,\mathrm{d}v}{\int_0^\infty n(v)\,\mathrm{d}v} \tag{3.19}$$

$$\left\langle \left(v^2\right) \right\rangle^2 = \frac{\int_0^\infty v^2 n(v)\,\mathrm{d}v}{\int_0^\infty n(v)\,\mathrm{d}v} \tag{3.20}$$

Solutions of the integral

$$I_n = \int_0^\infty y^n e^{-by^2}\,\mathrm{d}y \tag{3.21}$$

are well known, and may be found in many books such as the text by Mandl (1988):

$$I_0 = \frac{1}{2}\sqrt{\frac{\pi}{b}} \tag{3.22a}$$

$$I_1 = \frac{1}{2b} \tag{3.22b}$$

$$I_n = \left(\frac{n-1}{2b}\right) I_{n-2} \tag{3.22c}$$

Noting that the Maxwell-Boltzmann *speed* distribution take the form

$$n(v) = \text{const} \times v^2 \exp\left(-\frac{mv^2}{2k_\mathrm{B}T}\right) \tag{3.23}$$

we see that

$$\left\langle \left(v^2\right)^2 \right\rangle = \frac{I_6}{I_2} \tag{3.24a}$$

$$\left\langle \left(v^2\right) \right\rangle^2 = \frac{I_4}{I_2} \tag{3.24b}$$

$$\left(\delta(v_i^2)\right)^2 = \frac{I_6}{I_2} - \frac{I_4}{I_2} = \frac{3}{2b^2} = \frac{3}{2}\left(\frac{2k_\mathrm{B}T}{m}\right)^2 \tag{3.25}$$

and thus for any one particle contributing to the temperature, the resulting temperature fluctuation may be expressed as[6]

[6]The notion of the temperature of a single particle only makes sense when the speed may be

$$\Delta(v_i^2)^2 = \frac{3}{2}\left(\frac{2k_{\mathrm{B}}T}{m}\right)^2 \tag{3.26}$$

The total square fluctuation on the temperature may now be written as

$$\Delta T^2 = \sum_{i=1}^{N}\left[\frac{\partial T}{\partial(v_i^2)}\right]^2 \Delta(v_i^2)^2 = 6N\left(\frac{T}{\nu}\right)^2 \tag{3.27}$$

and hence

$$\frac{\Delta T}{T} = \frac{\sqrt{6N}}{\nu}. \tag{3.28}$$

3.6.2 Langevin thermostat

The *Langevin thermostat* (Chandrasekhar, 1943) satisfies the above requirement for the temperature and its fluctuation. It simulates the Brownian buffeting of the atoms under study by solvent atoms at the desired temperature. Mathematically, the force on the i^{th} atom becomes:

$$\boldsymbol{F}_i(t) \rightarrow \boldsymbol{F}_i(t) - \gamma m_i \boldsymbol{v}_i(t) + \boldsymbol{R}_i(t) \tag{3.29}$$

with

$$R_i^{\alpha}(t+\Delta t) = \sqrt{\frac{2m_i k_{\mathrm{B}}T}{\tau\,\Delta t}}N(0,1) \tag{3.30}$$

where α is a cartesian component index and $N(0,1)$ represents a normal random deviate with mean 0 and variance 1.

Note that the force on an atom is dependent upon its velocity. Therefore, to calculate the velocities at the next time step we require the forces which we are attempting to calculate. We can escape this vicious circle by substituting the velocity propagator of Equation 3.7b into Equation 3.29 to obtain the result given in Equation 3.31.

$$\boldsymbol{F}_i(t+\Delta t)\left[1+\frac{\gamma\Delta t}{2}\right] = \boldsymbol{F}_i^{\mathrm{raw}} - \gamma m_i \boldsymbol{v}_i\left(t+\frac{\Delta t}{2}\right) + \boldsymbol{R}_i(t+\Delta t) \tag{3.31}$$

Centroid thermostatting

We shall see in Chapter 5 that a quantum particle may be represented as a "necklace" of possible position realisations. Although we shall leave the reason why until later, we note here that applying Equation 3.31 to each point on the loop separately will tend to result in little or no *net* force on the loop as a whole. For this reason, in our implementation of the Langevin thermostat, a Langevin force was applied to the *whole* loop in addition to the Langevin forces acting on any single bead on the necklace with the extra caveat that the individual bead forces are scaled such that they sum to zero. The new Langevin forces with *centroid* thermostatting included takes the form:

$$\begin{aligned}\boldsymbol{F}_i(t+\Delta t)\left[1+\frac{\gamma\Delta t}{2}\right] = \frac{1}{P}\boldsymbol{F}_i^{\mathrm{raw}} \\ + \boldsymbol{R}_i^{\mathrm{bead}}(t+\Delta t) - \gamma m_i \boldsymbol{v}_i^{\mathrm{bead}}\left(t+\frac{\Delta t}{2}\right) \\ + \boldsymbol{R}_i^{\mathrm{centroid}}(t+\Delta t) - \gamma m_i \boldsymbol{v}_i^{\mathrm{centroid}}\end{aligned} \tag{3.32}$$

where

$$R^{\alpha}_{i,\mathrm{centroid}}(t+\Delta t) = \frac{\sqrt{P}}{P}\sqrt{\frac{2m_i k_{\mathrm{B}}T}{\tau\,\Delta t}}N(0,1) \tag{3.33}$$

This ensures efficient sampling of classical phasespace when performing path integral calculations without destroying the value of the average temperature or its RMS fluctuation; we are not waiting for the loops to drift around at an otherwise much slower rate.

3.6.3 Langevin dynamics, serial correlation & ergodicity

In simulations using the microcanonical ensemble, serial correlation is high because the motion at one timestep depended upon the positions, velocities and forces at the previous timestep. The beauty of the Langevin thermostat is that it introduces a stochastic influence. Random numbers influence the forces at each timestep, and those random numbers are uncorrelated between timesteps. A further benefit of Langevin dynamics is that an MD run is guaranteed to be ergodic, provided that the run length is sufficiently long. This point results from the fact that the random noise

term in the Langevin forces is Gaussian, and hence has infinitely long tails; if we wait long enough, then, we *will* see a force large enough to get the system out of a local minimum.

3.7 Constraint dynamics

In cases for which the intermolecular potential is defined for a fixed molecular geometry, we need to perform *constraint dynamics* to preserve that fixed molecular geometry throughout the simulation. This was achieved using the so-called RATTLE algorithm, which shall be our next topic.

3.7.1 RATTLE

There exists a technique for coping with constraints in the framework of a Velocity Verlet integration scheme, known as RATTLE (Andersen, 1983). This scheme uses Lagrange multipliers which, in effect, add in extra forces to keep the molecular geometry constant.

We begin by writing down the new forces:

$$m_1\ddot{\boldsymbol{r}}_1 = \boldsymbol{f}_1 + \boldsymbol{g}_1 \tag{3.34a}$$

$$m_2\ddot{\boldsymbol{r}}_2 = \boldsymbol{f}_2 + \boldsymbol{g}_2 \tag{3.34b}$$

$$m_3\ddot{\boldsymbol{r}}_3 = \boldsymbol{f}_3 + \boldsymbol{g}_3. \tag{3.34c}$$

The constraints we require

In order to preserve the molecular required for the TIP5P water model, we need to constrain three lengths: the bond lengths and also the distance between the two hydrogen atoms required to constrain the bond angle. This technique to preserve the bond lengths and also the bond angle is is referred to as *triangulating* the molecule (Allen and Tildesley, 1987).

Deriving the equations

In practice we do not know the precise forces $\boldsymbol{g}_i$, but we can find approximations to them using an iterative method. Inspecting Figure 3.5 we may write

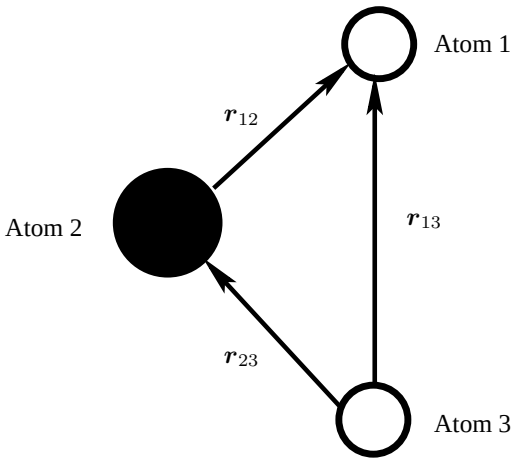

Figure 3.5: The atom labels used in the derivation of the RATTLE equations.

$$\boldsymbol{g}_1 = +\lambda_{12}\boldsymbol{r}_{12} + \lambda_{13}\boldsymbol{r}_{13} \tag{3.35a}$$

$$\boldsymbol{g}_2 = +\lambda_{23}\boldsymbol{r}_{23} - \lambda_{12}\boldsymbol{r}_{12} \tag{3.35b}$$

$$\boldsymbol{g}_3 = -\lambda_{13}\boldsymbol{r}_{13} - \lambda_{23}\boldsymbol{r}_{23} \tag{3.35c}$$

where the λ_{ij} are the Lagrange multipliers. Substituting these into Equation 3.34 and using the Velocity Verlet propagators of Equation 3.7 we find

$$\boldsymbol{r}_1(t+\Delta t) = \boldsymbol{r}'_1(t+\Delta t) + [+\lambda_{12}\boldsymbol{r}_{12} + \lambda_{13}\boldsymbol{r}_{13}]\,\frac{\Delta t^2}{2m_1} \tag{3.36a}$$

$$\boldsymbol{r}_2(t+\Delta t) = \boldsymbol{r}'_2(t+\Delta t) + [+\lambda_{23}\boldsymbol{r}_{23} - \lambda_{12}\boldsymbol{r}_{12}]\,\frac{\Delta t^2}{2m_2} \tag{3.36b}$$

$$\boldsymbol{r}_3(t+\Delta t) = \boldsymbol{r}'_3(t+\Delta t) + [-\lambda_{13}\boldsymbol{r}_{13} - \lambda_{23}\boldsymbol{r}_{23}]\,\frac{\Delta t^2}{2m_3} \tag{3.36c}$$

Equations 3.36a to 3.36c can be used to find expressions the separation vectors $\boldsymbol{r}_1$, $\boldsymbol{r}_2$ and $\boldsymbol{r}_3$. It is the *magnitude* of the vectors that we are interested in constraining. If we square the equations for the separation vectors we find

$$
\begin{aligned}
|\boldsymbol{r}_{12}(t+\Delta t)|^2 - |\boldsymbol{r}'_{12}(t+\Delta t)|^2 &= [\text{terms linear in } \Delta t^2] \\
&\quad + [\text{terms quadratic in } \Delta t^2] \quad \text{(3.37a)} \\
|\boldsymbol{r}_{13}(t+\Delta t)|^2 - |\boldsymbol{r}'_{13}(t+\Delta t)|^2 &= [\text{terms linear in } \Delta t^2] \\
&\quad + [\text{terms quadratic in } \Delta t^2] \quad \text{(3.37b)} \\
|\boldsymbol{r}_{23}(t+\Delta t)|^2 - |\boldsymbol{r}'_{23}(t+\Delta t)|^2 &= [\text{terms linear in } \Delta t^2] \\
&\quad + [\text{terms quadratic in } \Delta t^2] \quad \text{(3.37c)}
\end{aligned}
$$

We desire that the left-hand sides of Equation 3.37 are zero — in this case the propagated velocities are the same is the (unknown) actual velocites at the next timestep. Our task, then, is to find the Lagrange multipliers with which this is achieved.

3.7.2 Implementing RATTLE

In practice, we find the Lagrange multipliers by using linear algebra and interative techniques.

The equations of motion are first updated without any constraints applied. To find the required Lagrange multipliers, the terms in Equation 3.37 which are *quadratic* in Δt^2 are initially set to zero (i.e. no constraints), and the remaining linear equations are solved for the λ_{ij} by straightforward matrix inversion. If $\boldsymbol{A}$ is a matrix containing the linear terms *without Lagrange multipliers*, then

$$
\begin{pmatrix} \lambda_{12} \\ \lambda_{13} \\ \lambda_{23} \end{pmatrix} = \boldsymbol{A}^{-1} \begin{pmatrix} |\boldsymbol{r}_{12}(t+\Delta t)|^2 - |\boldsymbol{r}'_{12}(t+\Delta t)|^2 - O(\Delta t^4) \\ |\boldsymbol{r}_{13}(t+\Delta t)|^2 - |\boldsymbol{r}'_{13}(t+\Delta t)|^2 - O(\Delta t^4) \\ |\boldsymbol{r}_{23}(t+\Delta t)|^2 - |\boldsymbol{r}'_{23}(t+\Delta t)|^2 - O(\Delta t^4) \end{pmatrix}. \qquad \text{(3.38)}
$$

When "guesses" for the Lagrange multipliers have been generated from the matrix inversion, the quadratic terms are evaluated, added in and a better guess is generated using the linearised equations. This cycle is continued until the Lagrange multipliers have converged to better than one part in 10^{10}.

In practice, two sets of Lagrange multipliers are required to complete the update of the positions *and* the velocities, since the velocity propagator also requires the force at the *next* timestep, which is dependent upon the positions at the next timestep. To

get around this difficulty, we must converge the Lagrange multipliers at the current timestep, update the positions and also the velocities as far as we can; we must then converge the Lagrange multipliers again (corresponding to those at the *next* timestep) in order to complete the velocity update procedure.

Finally, since the positions and velocities are updated *without constraints* at the beginning of the constraint routine, we can add the constraint effects to those quantities to obtain the new *constrained* positions and velocities.

When applying constraint dynamics, it is important remember that the "extra forces" which are applied to hold the molecules together contribute to the *pressure* of the system, to which we shall move now.

3.8 Pressure and the stress tensor

The *pressure tensor*[7] in the context of TIP5P water may be expressed as

$$\mathsf{J}_{\alpha\beta} = \sum_{i=1}^{n} M_i v_{i\alpha} v_{i\beta} + \sum_{i<j}^{n} F_{ij\alpha}^{\mathrm{OO}} r_{ij\beta}^{\mathrm{OO}} - \frac{\partial E}{\varepsilon_{\alpha\beta}} + \sum_{i<j}^{3} \lambda_{ij} r_{ij\alpha} r_{ij\beta} \tag{3.39}$$

where M_i is the *molecular* mass, n is the number of *molecules* and the $v_{i\alpha}$ represent components of molecular centre of mass velocities. The first term represents the kinetic contribution to the pressure, the second is the pressure due to oxygen-oxygen Lennard-Jones interactions, and $\sigma_{\alpha\beta}$ represents the stress tensor due to charge site interactions to be introduced in Equation 3.42. The final term is the contribution to the intramolecular constraints which were mentioned at the end of the previous section; the λ_{ij} are the corresponding Lagrange multipliers. Not included in the pressure tensor are contributions due to Langevin forces, which average out to zero over the course of an MD run.

The scalar pressure is then given by

$$\mathsf{P} = \frac{1}{3\Omega} \left\langle \sum_{\alpha} \mathsf{J}_{\alpha\alpha} \right\rangle \tag{3.40}$$

where Ω is the simulation cell volume.

There is a further contribution to the pressure from charge site interactions to be met in Chapter 4, and may be calculated by means of the *stress tensor* ...

[7] The pressure tensor is discussed by Haile (1992), pp. 242.

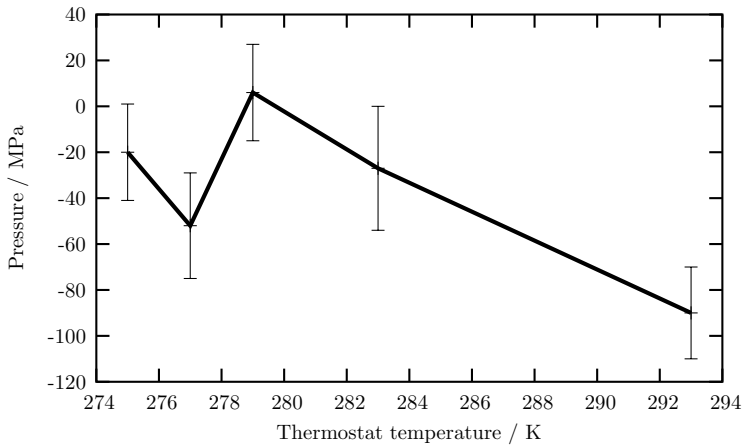

Figure 3.6: Pressure as a function of temperature from path integral simulations. Error bars were estimated using block averaging, but include RMS fluctuations due to the distribution in *imaginary time*, which is introduced in Chapter 5.

Let the columns $\boldsymbol{h}$ be vectors of the simulation cell. We can then define the *strain tensor* $\boldsymbol{\varepsilon}$ such that

$$\boldsymbol{h}' = (\boldsymbol{I} + \boldsymbol{\varepsilon})\boldsymbol{h} \tag{3.41}$$

where $\boldsymbol{h}'$ represents some new shape of the simulation cell. We may now define the *stress tensor*:

$$\sigma_{\alpha\beta} = \frac{1}{\Omega}\frac{\partial E}{\partial \varepsilon_{\alpha\beta}} \tag{3.42}$$

where Ω is the simulation cell volume. The stress tensor is just the negative of the pressure tensor.

While simulation times were sufficient to yield good structure functions, the pressure was not well converged with the present data and carries an uncertainty in the order of a few tens of MPa — the measured pressure as a function of temperature is shown in Figure 3.6. Consequently, the presence of a density maximum could not be justified by searching for a minimum of pressure; the measured pressures at T = 277 and T = 293 K, for example, are not statistically resolved.

3.9 Radial distribution function

The Radial Distribution Function (RDF) is something of a staple measurement in MD:

$$g(r) = \frac{V}{4\pi r^2 N^2} \left\langle \sum_i \sum_{i \neq j} \delta(r - r_{ij}) \right\rangle \tag{3.43}$$

where Δr is the radial width of the bins into which atomic separations are divided. The RDF represents the ratio of the density at a given distance from a particle (averaged over all atoms), to the uniform ideal density. In an ideal gas it would therefore assume the value of unity. On average, the density at a distance r from a particle is therefore given by

$$\rho(r) = \rho_{\text{uniform}} g(r). \tag{3.44}$$

3.10 Coordination numbers & hydrogen bonding

3.10.1 Coordination number

The *coordination number* refers to the number of particles which appear out to the the first minimum in the radial distribution function; that is, they appear in the ***first coordination shell***. Note that this is not quite the same as the number of nearest neighbours which the Voronoi construction of Subsection 3.11.1 presents. There it is possible for a particle to define a face of the Voronoi polyhedron (and hence be identified as a first nearest neighbour) and yet be in the *second* coordination shell; this is demonstrated graphically in Figure 3.7.

We may also define the *cumulative* coordination number as expressed in Equation 3.45:

$$N(r) = 4\pi\rho_{\text{H}} \int_0^r g_{\text{OH}}(r')\, r'^2 \mathrm{d}r' \tag{3.45}$$

This form of presentation affords an appreciation of how rapidly the number is changing with increasing radius. The coordination number is then obtained by setting $r = R_{\text{min}}$, where R_{min} is the position of the first minimum in the RDF.

3.10.2 Number of hydrogen bonds

We may take the idea of coordination numbers further and use them to quantify the number of hydrogen bonds present. Sato and Fumio (1999) point out that a common

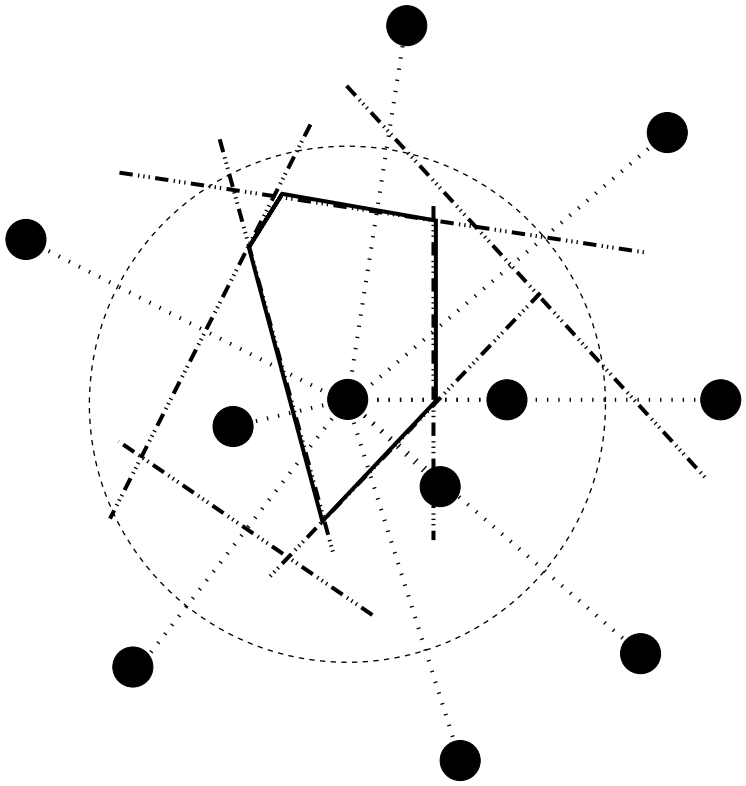

Figure 3.7: Graphical demonstration in two dimensions to show that a particle identified as a nearest neighbour by the Voronoi construction may not lie in the first coordination shell. Here the topmost particle defines a face of the Voronoi polygon, yet lies *outside* the dashed circle which approximates the minimum in the RDF.

definition for the number of hydrogen bonds is that given in Equation 3.46.

$$N_a = 4\pi\rho_{\mathrm{H}} \int_0^{R_{\min}} g_{\mathrm{OH}}(r)\, r^2 \mathrm{d}r \tag{3.46}$$

where ρ_{H} is the number density of hydrogen atoms and $R_{\min}$ is the distance to the first minimum of g_{OH}. This definition suffers from a lack of ability to distinguish between the case where hydrogen bonding is occuring and when hydrogen atoms are simply close to oxygen atoms. Sato and Fumio (1999) go on to present a more rigorous scheme. For our purposes, however, the estimate given by Equation 3.46 will be quite sufficient; indeed, we will estimate the number of intact hydrogen bonds using a geometrical analysis.

3.11 Local structure

We now move on to discuss more specific methods of analysing local bonding structure in water which are employed. Note that the analysis techniques to be described are based on water forming an approximately tetrahedral network as illustrated in Figure 3.8, and are not primed to detect *bifurcated* hydrogen bonding, as spoken of by Sciortino *et al.* (1990). When we speak of *bonded* molecules we refer only to those molecules which are closest to the central molecule, as for tetrahedral-like structures. That is to say, an increase in the number of *non-bonded* molecules refers to the possibility of many more molecules surrounding the central molecule, yet there remains only four "best" candidates for hydrogen bonding.

3.11.1 Voronoi analysis

Voronoi analysis[8] affords a technique for the analysis of nearest neighbours. We may define a Voronoi polyhedron which represents the region of space around a particle which is closer to that particle than to any other. A two-dimensional representation of this is shown in Figure 3.9.

We may now define the nearest neighbours of a particle at those atoms which define the faces of the Voronoi polyhedron; that is, an atom is counted as a nearest neighbour if the bisector between itself and the central atom forms a face of the Voronoi polyhedron. In the analysis to follow, the first four such nearest neighbours were taken into account when identifying hydrogen bonds.

[8] Voronoi analysis is addressed by Rapaport (1995), pp. 91–95.

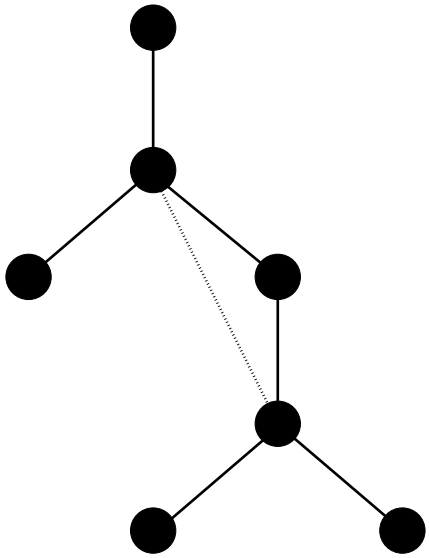

Figure 3.8: Representation of a tetrahedral network of water molecules. Hydrogen atoms are not shown. The solid lines indicate hydrogen bonds, whereas the the dotted line shows the second nearest neighbour separation.

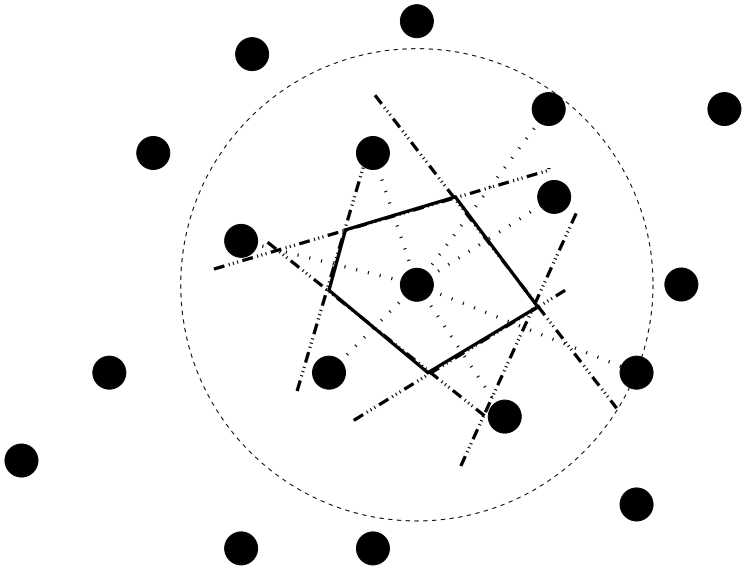

Figure 3.9: Schematic diagram of the procedure of Delauney triangulation for a two-dimensional system of argon. Lines are drawn from the central molecule out to some cut-off radius, and those lines are bisected. The corresponding Voronoi polygon is shown by the solid line. The cut-off radius is represented by the dashed circle.

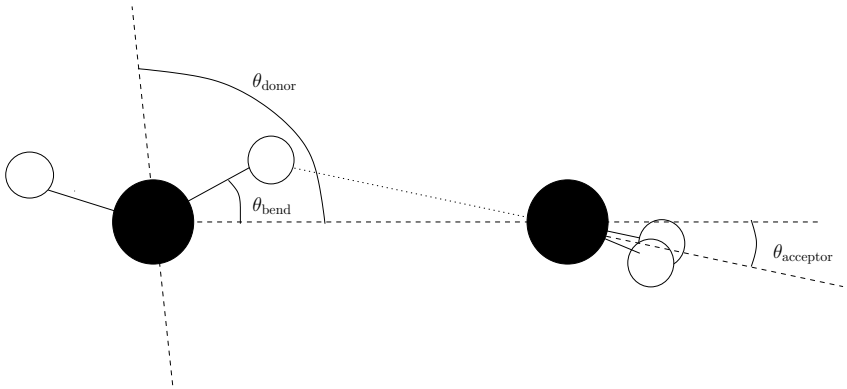

Figure 3.10: Illustration of the donor, acceptor and bond bending angles.

3.11.2 Nearest neighbours and hydrogen bonds

Though the Voronoi construction determines all nearest neighbours (NN) of a molecule[9], we saw in Figure 3.7 that the NN molecules which it identifies need not lie within the first coordination shell; indeed, there may be some variation as to how many molecules do lie within that shell. We proceed by treating the liquid as if it had a tetrahedral character, as in ice Ih.

It might be a concern that hydrogen bonds could be straighter — and hence stronger — with NN molecules that are further away from the central molecule than the closest four. We recall here the information about HB bending and stretching given in Chapter 2: the HB is more sensitive to stretching than to bending. Our central molecule is much less likely to be hydrogen bonded to those molecules which are *further away* than strongly bent.

Once the four nearest neighbour molecules to be used were identified, the hydrogen atom involved in the hydrogen bond then had to be found; that is, the hydrogen atom which forms the smallest value of the bending angle θ_{bend}. The bending angle is illustrated in Figure 3.10. The first NN distance and the θ_{bend} could then be calculated.

Second nearest neighbours were taken as the first nearest neighbours of the first nearest neighbours. The four nearest neighbours of the two first NN *acceptor* molecules were identified and those which were not the central molecule were included in resultant distributions. Restricting the analysis to neighbours of the two first NN acceptor molecules compliments the analysis of the acceptor angle which we discuss now.

[9]Oxygen atoms were taken as a reference point for the molecule.

3.11.3 Acceptor angle

In the construction of the TIP5P model, Mahoney and Jorgensen (2000) noted that a commonly missing feature in existing empirical potentials for water was a double well in the potential energy with respect to the *acceptor angle*, where the acceptor angle is defined as in Figure 3.10.

It should be noted that the acceptor angle as calculated from simulation here is purely the angle between the bisector of the acceptor molecule and the R_{OO} separation vector (pointing from donor to acceptor), and as such is positive definite. The double minima in the potential energy is strictly only identified the special case in which the bending angle θ_{bend} is zero and the plane in which the donor molecule hydrogen atoms lie is orthogonal to that plane in which the acceptor molecule H atoms lie. However, a demonstration of preference for the acceptor angle to assume a value consistent with a tetrahedral lattice — approximately $55^{\circ}\mathrm{C}$ — would be suggestive of a tetrahedral structure in the liquid.

After identifying the two first NN acceptor molecules, $\theta_{\mathrm{acceptor}}$ could be calculated. A strengthening of the hydrogen bond network in the liquid would be expected to manifest itself in a more localised value of $\theta_{\mathrm{acceptor}}$ *and* a more linear first NN bond bending angle; second NN distances may be analysed in relation to each of these.

3.12 Summary

Possible phasespace configurations for a molecular system may be generated by calcuating forces and updating positions and velocities according to Newton's equations of motion.

After a period of equilibration, it is then possible to sample those phasespace configurations during the course of a molecular dynamics production run. Provided that phasespace is sampled in an unbiased — or *ergodic* — manner, time averages of structural, dynamical and thermodynamical information become equivalent to *ensemble* averages. Provided, then, that a representative sample of phasespace is explored, we may find ensemble averages of structural information such as the equilibrium bonding geometry and nearest neighbour characteristics.

The water in the simulations presented here was equilibrated for at least 15 ps, and a production phase of 75 ps was found to be sufficient to generate good structure functions of interest. Samples were output every 30 fs.

Structure analysis focusses on first and second neighbour distances, particularly as they relate to hydrogen bond bending and first NN orientation.

The methodology behind the calculation of intermolecular forces is the subject of the following chapter. The molecular dynamics thus far deals only with classical simulation. The technique by which *quantum* properties were accounted for is described in Chapter 5.

Chapter 4

Molecular Modelling

4.1 Introduction

The success of molecular dynamics simulation rests in the most part with the model which is used to evaluate forces. There exists a hierarchy of methods available to us for perfoming this task, each at varying levels of complexity and accuracy.

In this chapter we shall discuss ideas behind the empirical potential used in the present simulations, together with further implementation techniques. Comparisons with *ab initio* calculations are made.

Section 4.2 introduces component terms of the empirical potential used here; the potential is introduced in Section 4.3. Energy surfaces are compared with *ab initio* calculations in Section 4.4. Notes concerning nuclear quantum corrections are made in Section 4.5, and Section 4.6 brings the chapter to a close.

4.2 Features of empirical potentials

4.2.1 Lennard-Jones potential

The Lennard-Jones interaction models the van der Waal dipole–dipole interaction between atomic charge clouds[1], and has the form:

$$V(r) = 4\epsilon_{\mathrm{O}} \left[\left(\frac{\sigma_{\mathrm{O}}}{r} \right)^{12} - \left(\frac{\sigma_{\mathrm{O}}}{r} \right)^{6} \right] \tag{4.1}$$

[1] van der Waal forces are discussed by Walton (1983), pp. 48–51

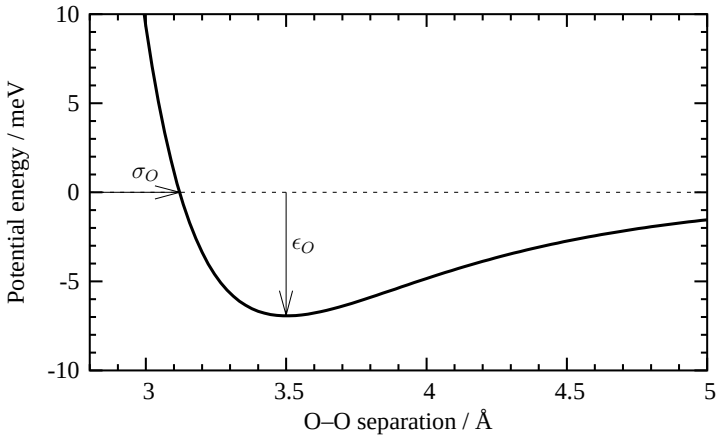

Figure 4.1: Lennard-Jones potential for oxygen, using parameters dictated by the TIP5P potential of Section 4.3.

where σ_{O} is the distance from $r = 0$ to the first zero of potential, and ϵ_{O} denotes the depth of the potential well. The curve is shown in Figure 4.1 using parameters for oxygen which are used in the classical form of the empirical potential used here.

The dipole–dipole interaction has the form

$$V(r) \sim -\frac{1}{r^6} \tag{4.2}$$

where r is the magnitude of the separation between the dipole centres of charge. Dipoles may be either permanent, induced, or spontaneous. By spontaneous we mean that fluctuations in charge clouds may give rise to temporary situations in which the centre of electronic charge in an atom does not lie on the same point as the centre of positive charge.

The Lennard-Jones potential also contains a strongly repulsive core of the form

$$V(r) \sim \frac{1}{r^{12}} \tag{4.3}$$

which acts to minimise the overlap of electron clouds. Note that this term is just the square of the $\frac{1}{r^6}$ for reasons of computational speed.

Truncation

To limit the number of molecules that are considered to be exerting a force on a given molecule, a cut-off radius was defined such that the Lennard-Jones tail reaches a zero of force at that radius; the cut-off was less than half the length of a simula-

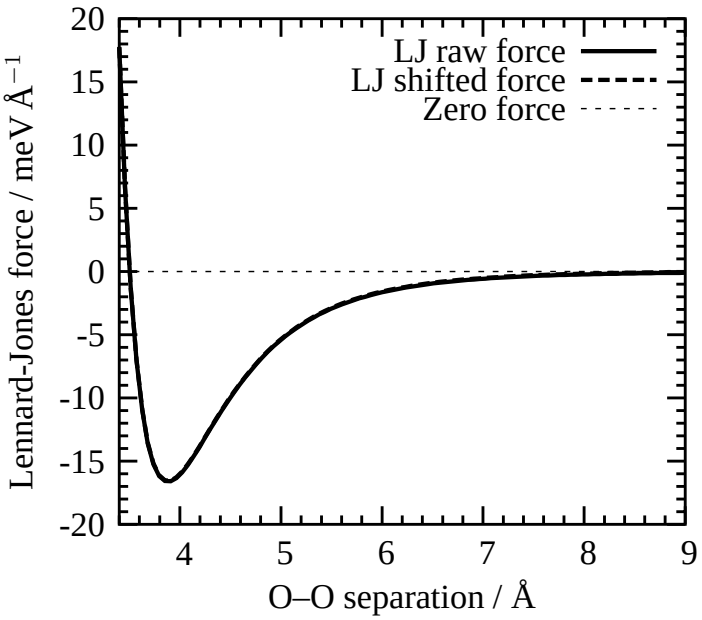

Figure 4.2: Lennard-Jones force for oxygen. The LJ parameters are those defined by the TIP5P model of Section 4.3.

tion cell side length to prevent atoms interacting with themselves through periodic boundary conditions.

To ensure that the force remains continuous across the cut-off boundary, the force may be shifted in order that it goes to zero at that point as shown in Figure 4.2.

The energy corresponding to the shifted force may be approximated by the first order integration scheme given in Equation 4.4.

$$V_{\text{shifted}} = V_{\text{LJ}}(r) - V_{\text{LJ}}\left(r_{\text{cut}}\right) + \left(r - r_{\text{cut}}\right) F_{\text{LJ}}\left(r_{\text{cut}}\right) \tag{4.4}$$

In practice, the magnitudes of the force and energy shifts for a cut-off radius of 8.7 Å are:

$$\begin{aligned} \text{Force shift:} \quad & -4.02 \times 10^{-5}\,\text{eV/Å} \\ \text{Energy shift:} \quad & -5.89 \times 10^{-5}\,\text{eV}. \end{aligned} \tag{4.5}$$

The force shift is tiny — three orders of magnitude smaller than the maximum attractive force. The Lennard-Jones force is illustrated in Figure 4.2; though both shifted and unshifted curves are shown, they are indistinguishable.

4.2.2 Coulomb interactions

Charge site interactions are described using Coulomb's law familiar from the classical theory of electrostatics. The force exterted *by* q_i *on* q_j is given by:

$$\boldsymbol{F}_{ij} = \frac{1}{4\pi\varepsilon_0}\frac{q_i\, q_j \hat{\boldsymbol{r}}_{ij}}{|\boldsymbol{r}_j - \boldsymbol{r}_i|^2} \tag{4.6}$$

where q_i and q_j are the charges on the particles i, j and ε_0 is the permittivity of free space. $\hat{\boldsymbol{r}}_{ij}$ is a unit vector pointing from q_i to q_j.

Coulomb interactions fall off as $\frac{1}{r}$, which may be compared with the $\frac{1}{r^6}$ dependence in the tail of the Lennard-Jones potential.

Since the interaction is so long-ranged, it demands a rigorous treatment of electrostatics over many surrounding image cells; this may by achieved using the *Ewald summation*[2] (Ewald, 1921). Here each point charge is given a Gaussian halo of charge which has the same magnitude but the opposite sign. The haloes screen the point charges making them short-ranged. In order to compute the Ewald energy, we must sum over these new short-ranged interactions in real space, and those of the haloes and their anti-haloes in reciprocal space (which are periodic due to periodic boundary conditions).

The Ewald sum is based on the identity

$$\begin{aligned}\sum_{\boldsymbol{l}} \frac{1}{|\boldsymbol{R}_1 + \boldsymbol{l} - \boldsymbol{R}_2|} = \frac{2}{\sqrt{\pi}} \sum_{\boldsymbol{l}} \int_\eta^\infty \exp\left(-|\boldsymbol{R}_1 + \boldsymbol{l} - \boldsymbol{R}_2|^2 \rho^2\right) d\rho \\ + \frac{2\pi}{\Omega} \sum_{\boldsymbol{G}} \int_0^\eta \exp\left(-\frac{|\boldsymbol{G}|^2}{4\rho^2}\right) \exp\left(\mathrm{i}(\boldsymbol{R}_1 - \boldsymbol{R}_2)\cdot\boldsymbol{G}\right) \frac{1}{\rho^3} d\rho.\end{aligned} \tag{4.7}$$

where $\boldsymbol{l}$ and $\boldsymbol{G}$ are real and reciprocal space lattice vectors respectively. Ω is the simulation cell volume.

The Ewald energy is then given by

[2] The Ewald sum is discussed in some detail by Frenkel and Smit (1996), pp. 347–354.

$$E^{\text{Ewald}} = \frac{1}{2}\sum_{i,j}\sum_{\boldsymbol{l}'}\frac{\text{erfc}\left(\eta\left|\boldsymbol{R}_i+\boldsymbol{l}-\boldsymbol{R}_j\right|\right)}{\left|\boldsymbol{R}_i+\boldsymbol{l}-\boldsymbol{R}_j\right|} + \frac{1}{2}\sum_{i,j} Z_i Z_j \frac{4\pi}{\Omega}\sum_{\boldsymbol{G}\neq 0}\frac{1}{|\boldsymbol{G}|^2}\exp\left(-\frac{|\boldsymbol{G}|^2}{4\eta^2}\right)\cos\left((\boldsymbol{R}_i-\boldsymbol{R}_j)\cdot\boldsymbol{G}\right) - \frac{1}{2}\sum_{i,j} Z_i Z_j \frac{\pi}{\eta^2\Omega} - \sum_i Z_i \frac{\eta}{\sqrt{\pi}}. \quad (4.8)$$

Higher values of the parameter η give narrower haloes, and consequently shorter ranged Coulomb interactions that must be dealt with in real space. However, as the haloes get narrower, a larger number of plane waves in reciprocal space are required to model them making the reciprocal space summation more expensive. We must therefore find an optimum value of η which reaches a compromise between the real and reciprocal space summations.

In the implementation used here, η was estimated through Equation 4.9:

$$\eta = \frac{\sqrt{\pi}}{\left(|\boldsymbol{a}|\,|\boldsymbol{b}|\,|\boldsymbol{c}|\right)^{\frac{1}{3}}} \quad (4.9)$$

where $\boldsymbol{a}$, $\boldsymbol{b}$ and $\boldsymbol{c}$ are simulation cell vectors (**?**). Further, there exists a cut-off radius in the real term of magnitude $r_{\text{cut}} = \eta\left|\boldsymbol{R}_1+\boldsymbol{l}-\boldsymbol{R}_2\right|$, and a similar spherical cut-off in recipocal space $g_{\text{cut}} = (|\boldsymbol{G}|/2\eta)$; r_{cut} = g_{cut} is hard-wired into the code.

An expression for the Ewald forces may be found by differentiating Equation 4.8:

$$\boldsymbol{F}_i^{\text{Ewald}} = \frac{1}{2}Z_i\sum_j Z_j\sum_{\boldsymbol{l}}\eta^3 \left(\frac{2}{\sqrt{\pi}}\frac{\exp\left(-\eta^2\left|\boldsymbol{R}_i+\boldsymbol{l}-\boldsymbol{R}_j\right|^2\right)}{\eta^2\left|\boldsymbol{R}_i+\boldsymbol{l}-\boldsymbol{R}_j\right|^2} + \frac{\text{erfc}\left(\eta\left|\boldsymbol{R}_i+\boldsymbol{l}-\boldsymbol{R}_j\right|\right)}{\eta^3\left|\boldsymbol{R}_i+\boldsymbol{l}-\boldsymbol{R}_j\right|^3}\right)(\boldsymbol{R}_i+\boldsymbol{l}-\boldsymbol{R}_j) + \frac{1}{2}Z_i\sum_j Z_j\frac{4\pi\eta}{\Omega}\sum_{\boldsymbol{G}\neq 0}\frac{\boldsymbol{G}}{|\boldsymbol{G}|^2}\exp\left(-\frac{|\boldsymbol{G}|^2}{4\eta^2}\right)\sin\left((\boldsymbol{R}_i-\boldsymbol{R}_j)\cdot\boldsymbol{G}\right) \quad (4.10)$$

In addition, the Ewald contribution to the stress tensor

$$\sigma_{\alpha\beta} = \frac{1}{\Omega}\frac{\partial E_{\text{Ewald}}}{\partial\varepsilon_{\alpha\beta}} \quad (4.11)$$

is given by (Nielsen and Martin, 1982):

$$\begin{aligned}\frac{\partial E_{\text{Ewald}}}{\partial \varepsilon_{\alpha\beta}} = \frac{1}{2}\sum_{i,j} Z_i Z_j \sum_{\boldsymbol{l}} -\eta^3 \\ \left(\frac{2}{\sqrt{\pi}}\frac{\exp\left(-\eta^2\left|\boldsymbol{R}_i+\boldsymbol{l}-\boldsymbol{R}_j\right|^2\right)}{\eta^2\left|\boldsymbol{R}_i+\boldsymbol{l}-\boldsymbol{R}_j\right|^2} + \frac{\operatorname{erfc}\left(\eta\left|\boldsymbol{R}_i+\boldsymbol{l}-\boldsymbol{R}_j\right|\right)}{\eta^3\left|\boldsymbol{R}_i+\boldsymbol{l}-\boldsymbol{R}_j\right|^3}\right) \\ \times\left(\boldsymbol{R}_i+\boldsymbol{l}-\boldsymbol{R}_j\right)_\alpha\left(\boldsymbol{R}_i+\boldsymbol{l}-\boldsymbol{R}_j\right)_\beta \\ + \frac{1}{2}\sum_{i,j} Z_i Z_j \frac{4\pi}{\Omega}\sum_{\boldsymbol{G}\neq 0}\frac{1}{|\boldsymbol{G}|^2}\cos\left(\left(\boldsymbol{R}_i-\boldsymbol{R}_j\right)\cdot\boldsymbol{G}\right)\left(\frac{2\boldsymbol{G}_\alpha\boldsymbol{G}_\beta}{|\boldsymbol{G}|^2}\left(\frac{|\boldsymbol{G}|^2}{4\eta^2}+1\right)-\delta_{\alpha\beta}\right) \\ + \frac{1}{2}\left(\sum_i Z_i\right)^2\frac{\pi}{\Omega\eta^2}\delta_{\alpha\beta}. \quad (4.12)\end{aligned}$$

4.3 Empirical potentials for water

Many properties of water models — empirical or otherwise — have been summarised by Guillot (2002). Path integral molecular dynamics — to be met in Chapter 5 — makes heavy computational demands. It is therefore desirable for intermolecular interactions to be calculated as cheaply as possible. Empirical models for water have a huge speed advantage over *ab initio* methods, particularly considering the number of molecules which are simulated. A suitable empirical potential was therefore chosen for the present simulations. Here, after a brief digression, follows a description of the empirical model used.

4.3.1 SPC/E potential

Before we come to discuss the TIP5P potential, we shall mention the SPC/E potential in passing. The Simple Point Charge (Extended), or SPC/E model (Berendsen *et al.*, 1987), has been used ubiquitously for the simulation of water and constitutes a first attempt to build something of the electronic polarisation into a rigid body intermolecular potential.

The functional form is given in Equation 4.13:

$$V(r) = \sum_{i=1}^{3}\sum_{j=1}^{3}\frac{q_i q_j}{r_{ij}} + 4\varepsilon_0\left[\left(\frac{\sigma_0}{r_{\text{OO}}}\right)^{12} - \left(\frac{\sigma_0}{r_{\text{OO}}}\right)^{6}\right] \quad (4.13)$$

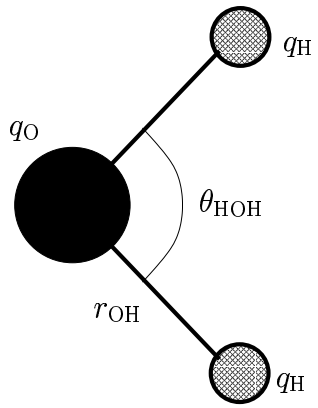

Figure 4.3: Molecular geometry of the SPC/E model for water.

r_{OH} (Å)	1.0
θ_{HOH} (deg)	109.47
q_{H} (e)	+0.4238
q_{O} (e)	-0.8476
σ_{O} (Å)	3.166
ϵ_{O} (kcal/mol)	0.155

Table 4.1: Parameterisation of the SPC/E model for water (Berendsen *et al.*, 1987).

The molecular geometry for the SPC/E potential is shown in Figure 4.3, and the parameterisation is given in Table 4.1.

The SPC/E model does show a density maximum, though it occurs at -38°C and 1 atm pressure (Baez and Clancy, 1994). Even though the model was parameterised to capture something of electronic polarisation, the TMD remains far removed from experiment.

4.3.2 TIP5P potential

Having been found to give an excellent description of the density maximum, the TIP5P potential (Mahoney and Jorgensen, 2000, 2001) was chosen for the present simulations. This model has a fixed molecular geometry which is approximately tetrahedral; this reflects the roughly tetrahedral character of the electron density in a water molecule. It is not, however, the first tetrahedral–like model; the ST2 model before it (Stillinger and Rahman, 1974) adopted such a form, although it involved computational complexities which have been shed in the TIP5P potential.

The potential has the mathematical form given in Equation 4.14:

$$V(r) = \sum_{i=1}^{4}\sum_{j=1}^{4}\frac{q_i q_j}{r_{ij}} + 4\epsilon_O\left[\left(\frac{\sigma_O}{r_{\mathrm{OO}}}\right)^{12} - \left(\frac{\sigma_O}{r_{\mathrm{OO}}}\right)^{6}\right]. \tag{4.14}$$

The molecular geometry is illustrated in Figure 4.4, and the parameterisation given in Table 4.2. Note that there are two sets of parameters; one set is for use with classical calculations, and the other for a path integral treatment. Both parameterisations were constructed so as to reproduce the correct liquid density at 25°C and 1 atm pressure.

The number of molecules for the present simulations was chosen to the 216 for which the TIP5P(PI) potential was parameterised. The same particle number was kept for classical simulation, though the TIP5P model was strictly parameterised for 512 molecules, for reasons of computational speed. However, we shall see in Chapter 7 that any structural changes caused by a small shift in the precise location of the density maximum due to finite size effects in classical water is tiny when compared with the structural changes upon activation of path integrals, and hence in no way hinders the relevant discussion presented there.

The necessity for the special quantum parameterisation has its origin in the method by which the model was parameterised — to comply with experiment. Experimental data already has the quantum effects included, and consequently the classical parameterisation will capture something of those quantum effects, but the description will be incomplete. Indeed Mahoney and Jorgensen (2001) applied path integrals to the TIP5P (classical) parameterisation and the density maximum was seen to become much *worse*, undergoing a significant downward shift. Employing the classical parameterisation in a path integral calculation will result in quantum effects, to some extent, being included *twice*. It is worthy of note that Mahoney and Jorgensen (2001) found that path integral simulation — using the TIP5P(PI) potential — performs better than classical simulation; Mahoney and Jorgensen note that the energy, density and heat capacity are better than those given by the TIP5P model.

It should be noted that while Table 4.2 lists eight parameters, there are in fact only four free parameters: r_{OL}, q_{H}, σ_{O} and ϵ_{O}. (q_{LP} is taken to be equal and opposite to q_{H} to give molecular charge neutrality. The parameters r_{OH} and θ_{HOH} are set to their experimental gas phase values, and θ_{LOL} is set to the the angle between arms of a perfect tetrahedron.

Mahoney and Jorgensen point to previous work when they comment that a common problem with empirical potentials may be the lack of a double minimum in the potential energy as a function of the acceptor angle $\theta_{\mathrm{acceptor}}$; the double well in the

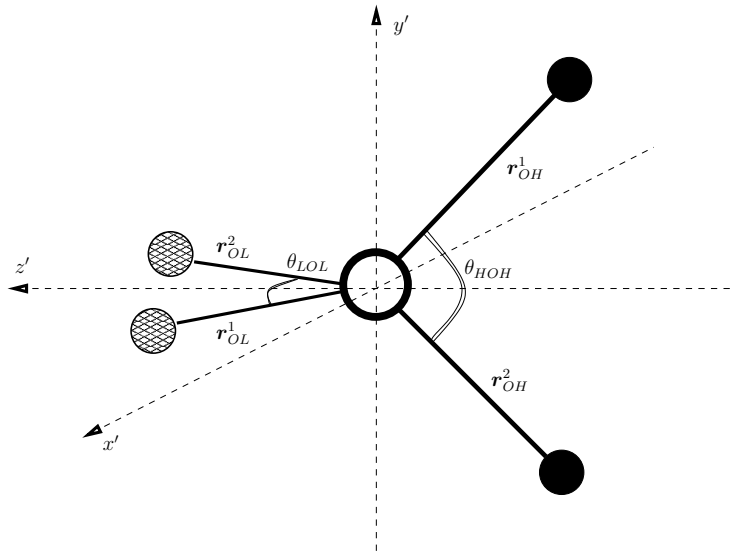

Figure 4.4: Molecular geometry of the TIP5P model for water.

	Classical	Quantum (5 beads)
r_{OH} (Å)	0.9572	same
r_{OL} (Å)	0.70	same
θ_{HOH} (deg)	104.52	same
θ_{LOL} (deg)	109.47	same
q_{H} (e)	+0.241	+0.251
q_{LP} (e)	-0.241	-0.251
σ_{O} (Å)	3.12	same
ϵ_{O} (kcal/mol)	0.16	same

Table 4.2: Parameterisation of the TIP5P and TIP5P(PI) models for water.

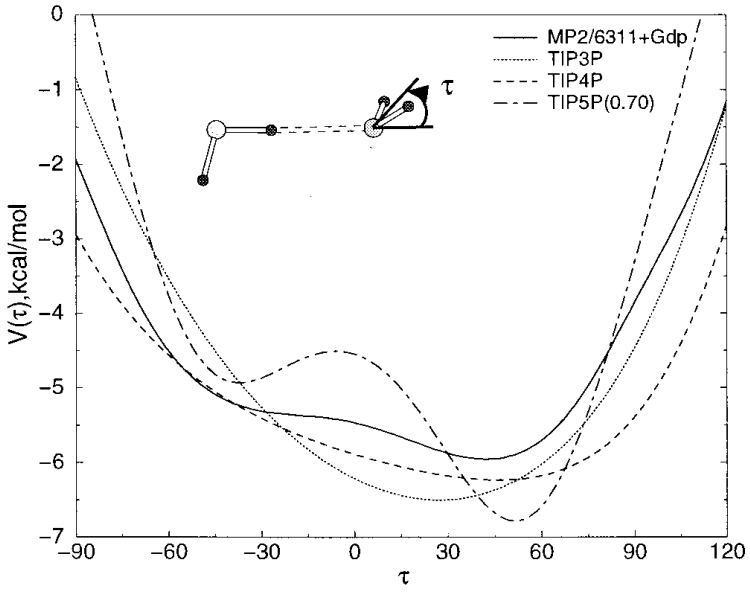

Figure 4.5: Potential energy as a function of acceptor angle ($\tau \equiv \theta_{\mathrm{acceptor}}$ here). Curves for other TIPnP potentials are shown. The solid line results from *ab initio* calculation. Taken from Mahoney and Jorgensen (2000).

TIP5P potential is illustrated in Figure 4.5, together with curves using other methods. Such a double well serves to encourage the lone pair lobes to point towards the donor hydrogen atom, and in doing so promotes tetrahedral order.

Path integral calculations[3] have been performed using the TIP5P model, and it was found that there was a downward shift in the density maximum to $T \lesssim 248\,\mathrm{K}$; in light of this, Mahoney and Jorgensen (2001) have reparameterised the TIP5P potential for use with path integral calculations — the new parameterisation is known as the TIP5P(PI) model.

Recent concerns have been raised over long-range interactions (Lísal *et al.*, 2002), which seem to result from the fact that the TIP5P model was parameterised using a cut-off radius for both the Lennard-Jones *and* Coulomb interactions. These authors note that the density maximum is slightly shifted upon application of an Ewald summation. The resulting density profile $\rho(T)$, however, is broader than that obtained by TIP5P with a simple cut-off scheme — visually closer to the broadness of the experimental profile. While there is perhaps a case for the reparameterisation of the TIP5P potential incorporating the Ewald sum, for the moment we note that both the classial and quantum models were parameterised using the same cut-off radius. The possibility that the precise location of the TMD may be shifted is of little consequence to the results presented in this thesis. Indeed, we shall see that structure functions presented in Chapter 7 point to the density maximum being located at the

[3] Path integrals are introduced in Chapter 5.

correct temperature.

Constructing lone pair site positions

Lone pair interactions influence the force on the molecular centre of mass, and also the torque about it. While they are needed for a true implementation of the model, they cannot be treated dynamically as atoms — they have no mass and there is nothing for intermolecular forces to act upon. Rather than storing the position vectors of the lone pair interaction sites, they can be constructed from the oxygen and hydrogen position vectors. This section describes a method by which this may be achieved.

The direction $\hat{\boldsymbol{y}}'$ is easily found by subtracting one hydrogen atom position vector from the other. Taking the cross product of their position vectors with the oxygen atom as the origin gives us $\hat{\boldsymbol{x}}'$. The unit vector $\hat{\boldsymbol{z}}'$ can then be found by crossing the unit vectors $\hat{\boldsymbol{x}}'$ and $\hat{\boldsymbol{y}}'$.

Mathematically,

$$\hat{\boldsymbol{y}}' = \frac{\boldsymbol{r}^1_{\mathrm{OH}} - \boldsymbol{r}^2_{\mathrm{OH}}}{|\boldsymbol{r}^1_{\mathrm{OH}} - \boldsymbol{r}^2_{\mathrm{OH}}|} \tag{4.15}$$

and it follows that

$$\hat{\boldsymbol{x}}' = \frac{\boldsymbol{r}^2_{\mathrm{OH}} \times \boldsymbol{r}^1_{\mathrm{OH}}}{|\boldsymbol{r}^2_{\mathrm{OH}} \times \boldsymbol{r}^1_{\mathrm{OH}}|} \tag{4.16}$$

and finally

$$\hat{\boldsymbol{z}}' = \hat{\boldsymbol{x}}' \times \hat{\boldsymbol{y}}' \tag{4.17}$$

Having found the body-fixed coordinates of the molecule, we can then use spherical polar coordinates to place the interaction sites in the correct places. Recalling that

$$x' = r \sin\theta \cos\phi \tag{4.18}$$
$$y' = r \sin\theta \sin\phi \tag{4.19}$$
$$z' = r \cos\theta \tag{4.20}$$

we see that

$$x' = \pm r_{\mathrm{OL}} \sin\left(\frac{1}{2}\theta_{\mathrm{LOL}}\right) \tag{4.21}$$

$$y' = 0 \tag{4.22}$$

$$z' = r_{\mathrm{OL}} \cos\left(\frac{1}{2}\theta_{\mathrm{LOL}}\right) \tag{4.23}$$

Finally, we need to project these on to the space-fixed frame, and add the oxygen position vector to give us position vectors relative to the global origin.

$$\boldsymbol{r}_L^1 = \begin{bmatrix} r_{\mathrm{OL}} \sin\left(\frac{1}{2}\theta_{\mathrm{LOL}}\right) \hat{\boldsymbol{x}}' \cdot \hat{\boldsymbol{x}} \\ 0 \\ r_{\mathrm{OL}} \cos\left(\frac{1}{2}\theta_{\mathrm{LOL}}\right) \hat{\boldsymbol{z}}' \cdot \hat{\boldsymbol{z}} \end{bmatrix} + \boldsymbol{r}_{\mathrm{O}} \tag{4.24}$$

$$\boldsymbol{r}_L^2 = \begin{bmatrix} -r_{\mathrm{OL}} \sin\left(\frac{1}{2}\theta_{\mathrm{LOL}}\right) \hat{\boldsymbol{x}}' \cdot \hat{\boldsymbol{x}} \\ 0 \\ r_{\mathrm{OL}} \cos\left(\frac{1}{2}\theta_{\mathrm{LOL}}\right) \hat{\boldsymbol{z}}' \cdot \hat{\boldsymbol{z}} \end{bmatrix} + \boldsymbol{r}_{\mathrm{O}} \tag{4.25}$$

Force and torque contribution from lone pair sites

We have just shown how lone pair positions may by calculated, eliminating the need to propagate them explicitly in a simulation. The difficulty now is that we must find a way of accounting for their contribution to the force on the centre of mass (CM) of the molecule as a whole, and also the torque.

The first task, is to compute the force on the molecular centre of mass, and also the torque about the same:

$$\boldsymbol{f}_{\mathrm{CM}} = \sum_{i=1}^{4} \boldsymbol{f}_i \tag{4.26a}$$

$$\boldsymbol{\tau} = \sum_{i=1}^{4} \boldsymbol{r}_i \times \boldsymbol{\tau}_i \tag{4.26b}$$

where position vectors are those *relative to the centre of mass* and i is an index representing the four charged interaction sites in the molecule.

The forces required to reproduce the desired force on the centre of mass are:

$$\boldsymbol{f}_i = \frac{m_i}{M}\boldsymbol{f}_{\mathrm{CM}} \tag{4.27}$$

where M is the the total mass of the molecule, and the i runs from $1 \rightarrow 3$ and is an index of the three atoms in the molecule. With the correct force weighting according to the atomic masses — as above — there will be no unwanted torque generated by these forces.

Calculating the forces required to generate the desired torque may be achieved through the use of a system of Lagrange multipliers such that

$$\boldsymbol{f}_i^{\mathrm{d}} = \boldsymbol{f}_i^{\mathrm{g}} + \lambda_i \boldsymbol{f}_i^{\mathrm{g}} \tag{4.28}$$

where i is an index representing the three atoms within the molecule. $\boldsymbol{f}^{\mathrm{d}}$ and $\boldsymbol{f}^{\mathrm{g}}$ denote desired and guessed forces respectively. The λ_i are calculated so as to ensure that the torques about the three Cartesian axes are simultaneously those which are desired.

Forces required to generate desired torques — i.e. the *guessed* forces — may be estimated using the relation

$$\boldsymbol{\tau} \times \boldsymbol{r} = r^2 \boldsymbol{f} - \boldsymbol{r}\left(\boldsymbol{r} \cdot \boldsymbol{f}\right) \tag{4.29}$$

in the special case where $(\boldsymbol{r} \cdot \boldsymbol{f}) = 0$. We must now find three position vectors for each atom, each orthogonal to one of the Cartesian directions (such vectors are subsequently primed). Once achieved, we may calculate the moment of inertia of the molecule about each Cartesian axis:

$$I_\alpha = \sum_{i=1}^{3} m_i \left|r'_{i\alpha}\right|^2 \tag{4.30}$$

where α is an index of a Cartesian direction. Note that the oxygen atom also contributes to the moment of inertia, since it does not quite lie on the centre of mass.

Employing the rotational analogue of Equation 4.27, the initial guesses at the required forces are

$$\boldsymbol{f}_i = \sum_{\alpha=1}^{3} \frac{m_i}{I_\alpha}\left(\boldsymbol{\tau}_\alpha \times \boldsymbol{r}'_{i\alpha}\right). \tag{4.31}$$

We may now move on to calculate the Lagrange multipliers required to correct our initial guess such that the desired torque on the molecule is recovered. τ^{d} and τ^{g} shall represent the desired and "guessed" torques respectively. To do this we define a matrix $\mathbf{A}$ with elements of the form $(\boldsymbol{r}_\alpha \times \boldsymbol{f}_\alpha)_\beta$, where α runs from $1 \rightarrow 3$ and denotes an atom in the molecule, while β also runs from $1 \rightarrow 3$ and is the index of a component of torque. The matrix $\mathbf{A}$ then has the form

$$\mathbf{A} = \begin{pmatrix} (\boldsymbol{r}_1 \times \boldsymbol{f}_1)_1 & (\boldsymbol{r}_2 \times \boldsymbol{f}_2)_1 & (\boldsymbol{r}_3 \times \boldsymbol{f}_3)_1 \\ (\boldsymbol{r}_1 \times \boldsymbol{f}_1)_2 & (\boldsymbol{r}_2 \times \boldsymbol{f}_2)_2 & (\boldsymbol{r}_3 \times \boldsymbol{f}_3)_2 \\ (\boldsymbol{r}_1 \times \boldsymbol{f}_1)_3 & (\boldsymbol{r}_2 \times \boldsymbol{f}_2)_3 & (\boldsymbol{r}_3 \times \boldsymbol{f}_3)_3 \end{pmatrix}. \tag{4.32}$$

such that

$$\begin{pmatrix} \boldsymbol{\tau}_1^{\mathrm{d}} - \boldsymbol{\tau}_1^{\mathrm{g}} \\ \boldsymbol{\tau}_2^{\mathrm{d}} - \boldsymbol{\tau}_2^{\mathrm{g}} \\ \boldsymbol{\tau}_3^{\mathrm{d}} - \boldsymbol{\tau}_3^{\mathrm{g}} \end{pmatrix} = \mathbf{A} \begin{pmatrix} \lambda_1 \\ \lambda_2 \\ \lambda_3 \end{pmatrix} \tag{4.33}$$

where each element represents the total torque around each Cartesian axis, and includes contributions from all three atoms in the molecule with multipliers λ_1, λ_2 and λ_3. It follows that

$$\mathbf{A}^{-1} \begin{pmatrix} \boldsymbol{\tau}_1^{\mathrm{d}} - \boldsymbol{\tau}_1^{\mathrm{g}} \\ \boldsymbol{\tau}_2^{\mathrm{d}} - \boldsymbol{\tau}_2^{\mathrm{g}} \\ \boldsymbol{\tau}_3^{\mathrm{d}} - \boldsymbol{\tau}_3^{\mathrm{g}} \end{pmatrix} = \begin{pmatrix} \lambda_1 \\ \lambda_2 \\ \lambda_3 \end{pmatrix}. \tag{4.34}$$

The λ_i may then be obtained by straight-forward matrix inversion. With the knowledge of the Lagrange multipliers, the force on each atom which must be applied to generate the desired torque may then be found through Equation 4.28.

4.4 Energy surfaces

The TIP5P contains no account of the electronic quantum properties of water. Here we shall compare the potential energy surface of the dimer as a function of the O-O separation and the bond bending angle θ_{bend} calculated by empirical means with a surface using a rigorous treatment of electronic quantum behaviour.

4.4.1 Density functional theory

Hohenberg and Kohn (1964) showed that the ground state energy of a system was uniquely determined by the ground state charge density:

$$n\left(\boldsymbol{r}\right) = N \int \cdots \int \left|\Psi(\boldsymbol{r}_2, \ldots, \boldsymbol{r}_N)\right|^2 \mathrm{d}^3\boldsymbol{r}_2 \ldots \mathrm{d}^3\boldsymbol{r}_N \tag{4.35}$$

where N is the number of interacting electrons. Later, Kohn and Sham (1965) showed that the total energy of the system could be expressed in terms of orbitals of *non-interacting* quasi-particles $\{\psi_i\}$ in some external potential; the total energy is expressed in Equation 4.36:

$$\begin{aligned} E\left[\{\psi_i\}\right] = 2\sum_i \int \left[-\frac{\hbar^2}{2m}\right] \nabla^2\psi_i \,\mathrm{d}^3\boldsymbol{r} + \int V_{\mathrm{ion}}(\boldsymbol{r}) n(\boldsymbol{r}) \,\mathrm{d}^3\boldsymbol{r} \\ + \frac{e^2}{2} \int \frac{n(\boldsymbol{r}) n(\boldsymbol{r'})}{|\boldsymbol{r} - \boldsymbol{r'}|} \,\mathrm{d}^3\boldsymbol{r} \,\mathrm{d}^3\boldsymbol{r'} + E_{\mathrm{ion}}\left(|\boldsymbol{R}_I|\right) + E_{\mathrm{xc}}\left[n(\boldsymbol{r})\right]. \end{aligned} \tag{4.36}$$

The first term is that which relates to quasi-particle kinetic energy. The second handles electron-ion interactions, the third concerns electron-electron interactions and the fourth describes ion-ion interactions. E_{xc} is an energy term into which all remaining effects of electron exchange and correlation are packed. The *exchange* energy relates to the lowering of the Coulomb energy as a result of the spatial separation between electrons with parallel spins, due to wavefunction antisymmetry; *correlation* refers to the lowering of the Coulomb energy owing to the spatial separation between electrons with opposite spins. The problem, then, reduces to solving a system of Schrödinger-like single particle equations:

$$\left[-\frac{\hbar^2}{2m}\nabla^2 + V_{\mathrm{ion}}\left(\boldsymbol{r}\right) + V_{\mathrm{H}}\left(\boldsymbol{r}\right) + V_{\mathrm{xc}}\left(\boldsymbol{r}\right)\right] \psi_i\left(\boldsymbol{r}\right) = \varepsilon_i \psi_i\left(\boldsymbol{r}\right) \tag{4.37}$$

where the $\{\varepsilon_i\}$ represent eigenvalues of the orbitals and V_{H} is the electronic Hartree potential given by

$$V_{\mathrm{H}}(\boldsymbol{r}) = e^2 \int \frac{n\left(\boldsymbol{r'}\right)}{|\boldsymbol{r} - \boldsymbol{r'}|} \,\mathrm{d}^3\boldsymbol{r'} \tag{4.38}$$

and V_{xc} is the exchange-correlation potential given by the functional derivative

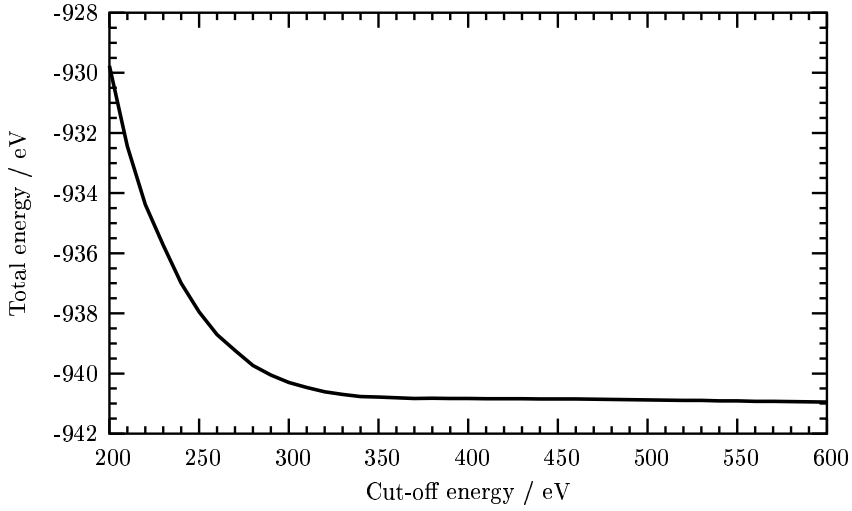

Figure 4.6: Total energy of the water dimer as a function of basis set size. The energy is sufficiently converged at about 380 eV.

$$V_{\mathrm{xc}}(\boldsymbol{r}) = \frac{\delta E_{\mathrm{xc}}\left[n(\boldsymbol{r})\right]}{\delta n(\boldsymbol{r})}. \tag{4.39}$$

Single point energies were calculated here using the Density Functional Theory code CASTEP (Segall *et al.*, 2002). The Perdew Burke Ernzerhof (PBE) functional (Perdew *et al.*, 1996) was chosen to handle electron exchange and correlation, in line with recent simulation (Schwegler *et al.*, 2000).

4.4.2 Converging energy & cell size

In theory, an infinitely large basis set size is required to fully match the wavefunction. In practice, properties such as total energy are sufficiently converged at some finite basis set size. Figure 4.6 shows the total energy of a water dimer as a function of basis set size.

We may further reduce the number of required plane waves by choosing a supercell which is just sufficiently large to prevent the dimer interacting with itself through periodic boundary conditions. Figure 4.7 shows the total energy of the dimer as a function of box size for each of the different dimensions. Here a box size of $(x, y, z) = 9 \times 9 \times 12$ was used, ensuring enough padding so that the dimer does not interact with itself for all configurations for which the energy was calculated.

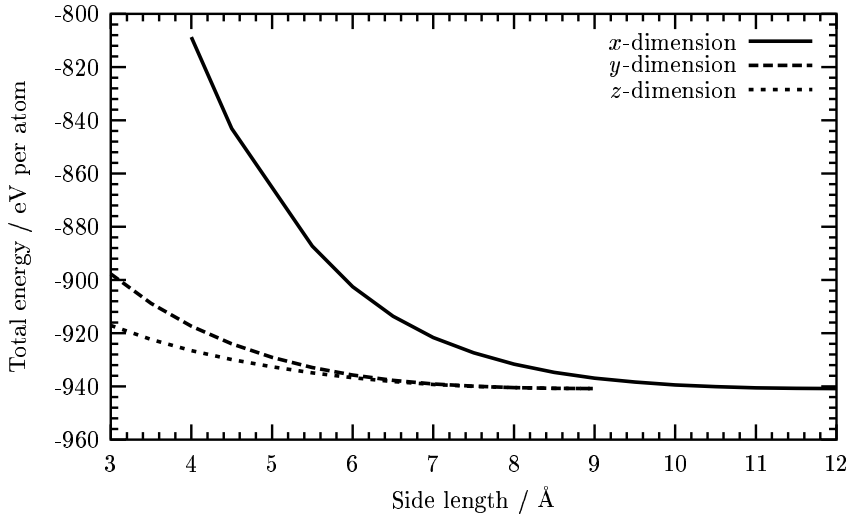

Figure 4.7: Total energy of the water dimer as a function of simulation cell size. The dimer lies along the x-axis.

4.4.3 Potential energy & bond bending

Figure 4.8 shows the potential energy as a function of oxygen-oxygen separation r_{OO} and bending angle in the water dimer[4], as calculated using the PBE functional. It is worthy of note that the surface shows a minimum at $r_{\mathrm{OO}} \simeq 2.8\,\text{Å}$, which as we shall see is the the position of the first peak in the radial distribution function in water close to the density maximum.

4.4.4 Comparison with TIP5P and SPC/E

Having calculated the potential energy surface with respect to bond bending angle, me may now compare the surface with those generated by the TIP5P and TIP5P(PI) potentials by subtracting the *ab initio* surfaces from them; these difference surfaces are presented in Figures 4.9(a) and 4.9(b). The TIP5P and TIP5P(PI) surfaces would appear to be relatively identical beyond an O-O distance of about 2.8 Å, below which very few molecules reside in the condensed phase!

4.5 Quantum corrections

Quantum effects may be cheaply accounted for, to some degree, through the Feynman-Hibbs variational treatment[5]. This method adds something something of quantum

[4]The acceptor angle was constrained to the value of $\frac{1}{2}\theta_{\mathrm{LOL}}$ as given by the TIP5P potential.
[5]Feynman and Hibbs (1965), Chapter 11.

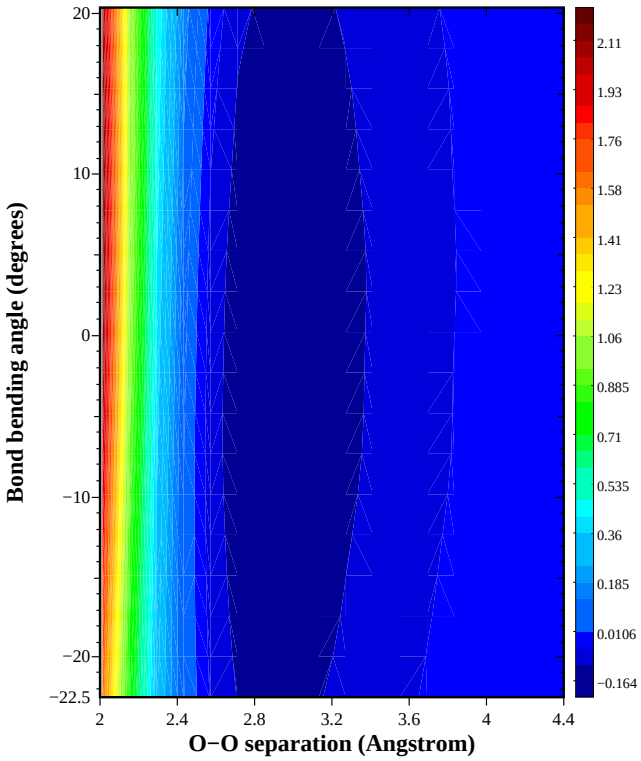

Figure 4.8: Potential energy surface from Density Functional Theory using the PBE functional.

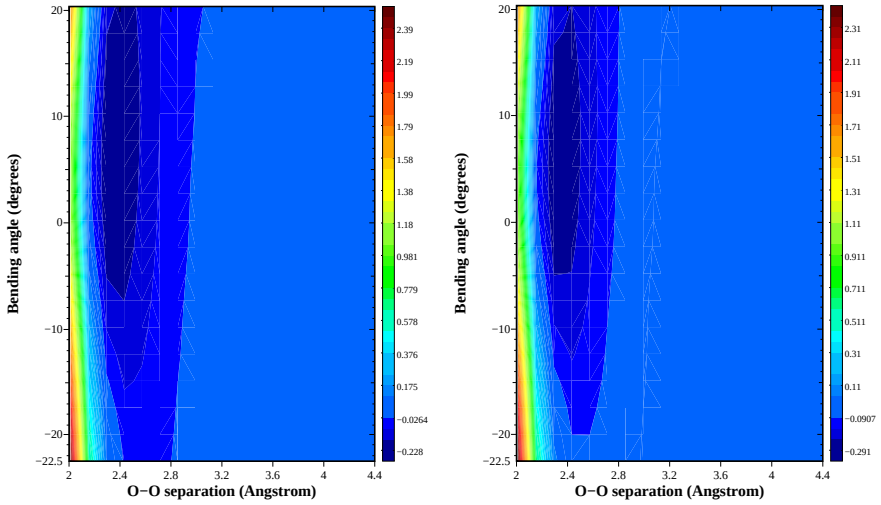

(a) TIP5P (b) TIP5P(PI)

Figure 4.9: Classical and quantum TIP5P minus *ab initio* difference surfaces.

effects to a classical intermolecular potential to form an *effective* potential. Guillot and Guissani (1998) applied this method to the simulation of water, and found good agreement *path integral* calculations. The advantage of the variational approach lies in the massively reduced computational load, though at the expense of also reducing the information which may be extracted from such simulations, such as the *radius of gyration* to be met in Chapter 5.

Grigera (2001) noted that some past attempts at the simulation of heavy water simply use the SPC/E model with doubled proton masses (Steinbach *et al.*, 1991; Guzzi *et al.*, 1999), which is not quite correct due to the important differences in nuclear quantum behaviour. Grigera gives credit to the simulations of Kuharski and Rossky (1985) and Del Buono *et al.* (1991) which used path integral techiques on top of classical potentials. The zero-point motion and tunnelling in the differing isotopes would therefore have a proper treatment. Grigera, then, has reparameterised the SPC/E potential for use with *heavy* water. This was necessary because a classical potential must capture at least something of the quantum mechanics when doubling the proton masses.

The TIP5P(PI) potential has never been tested for heavy water. Path integral calculations of heavy water have been attempted with the original TIP5P parameterisation (Mahoney and Jorgensen, 2001), and the density maximum was found to undergo an upward shift, though by an inflated amount when compared with experiment.

Such quantum differences are incorporated automatically as a result of performing a proper quantum treatment of nuclei; there is no need to attempt to build differences into the modelling potential. We may therefore apply the TIP5P(PI) potential to heavy water with a grounding of confidence.

4.6 Summary

Empirical models offer a comparatively inexpensive alternative to more rigorous methods such as *ab initio* simulation, which becomes important when faced with the computational demands of path integral simulation, to be met in Chapter 5.

The TIP5P model was chosen for this work, owing its very good density profile $\rho(T)$ as reported by Mahoney and Jorgensen (2000, 2001). 216 molecules were used in the simulations for this work, as dictated by the parameterisation of the TIP5P(PI) model.

The potential energy surfaces of both the TIP5P and TIP5P(PI) parameterisations

demonstrate excellent agreement with *ab initio* calculation above an O-O radial separation of $\simeq 2.8\,\text{Å}$.

Chapter 5

Path Integrals

5.1 Introduction

The path integral formulation of quantum mechanics (Feynman and Hibbs, 1965; Feynman, 1948) affords a computationally simple way of accounting for quantum mechanical zero point motion and tunnelling in molecular dynamics. In this chapter we shall explore the fundamentals of path integrals through to their application in computer simulation.

Sections 5.2 and 5.3 describe the path integral itself. Section 5.4 shows how the path integral may take on the form of a partition function and in so doing builds a bridge between quantum and statistical mechanics. The practical implementation of path integrals in molecular dynamics is the topic of Section 5.5, and Section 5.6 concerns itself with two particular cases: the harmonic oscillator and the free particle.

5.2 The path integral

Under the path integral scheme, the probability amplitude of a particle being at some particular position at some particular time is the summation of the probability amplitude of having come from some starting point, with all possible starting points summed over. This is expressed mathematically in Equation 5.1.

$$\Psi(x',t') = \int \mathrm{d}x\ \hat{u}(x',t';x,t)\Psi(x,t) \tag{5.1}$$

The term $\hat{u}(x',t';x,t)$ is called the *propagator*; it represents the probability of a

particle arriving at point (x', t') having travelled from point (x, t) on the assumption that it was certainly at (x, t) to begin with. The product of the propagator and the wavefunction $\Psi(x, t)$ represents the probability amplitude that the particle arrives at (x', t') having travelled from (x, t), since $\Psi(x, t)$ represents the probability amplitude of the particle being at (x, t) in the first instance. In this way, by summing over all possible positions, we may arrive at $\Psi(x', t')$ — the total probability amplitude at (x', t').

The path integral formulation of quantum mechanics, then, is concerned with likely paths between different points in space and time; we go on to develop this notion of likely and unlikely paths in the following section.

5.3 The propagator

The path integral propagator sums over possible paths between two points, and it is this to which we turn our attention now.

5.3.1 Principle of least action

In classical mechanics, the trajectory of a particle between two points is that which minimises the *action*; that is, the path $x(t)$ which minimises the functional $S[x]$:

$$S[x(t)] = \int_{t_1}^{t_2} dt\ \mathcal{L}[x(t)] \tag{5.2}$$

where $\mathcal{L}$ is the Lagrangian function $\mathcal{L} = T - V$.

The path represented in Figure 5.1 is an unlikely path for a free particle, for example; that would travel in a straight line between two points, because if it were to follow curved trajectory it would either have to travel at the same speed but take more time to complete the journey, or it would have to travel faster. Both of these act to push up the action. Figure 5.2 shows the height of a ball thrown upwards in a gravitational field as a function of time. While it is desireable for the ball to gain as much height as possible as quickly as possible — for this reduces the action through the negative potential term — a rapid height gain would necessitate a large kinetic energy, which acts to *increase* the action. The path we see is therefore a trade-off between maximising the potential energy and minimising the kinetic energy over the path.

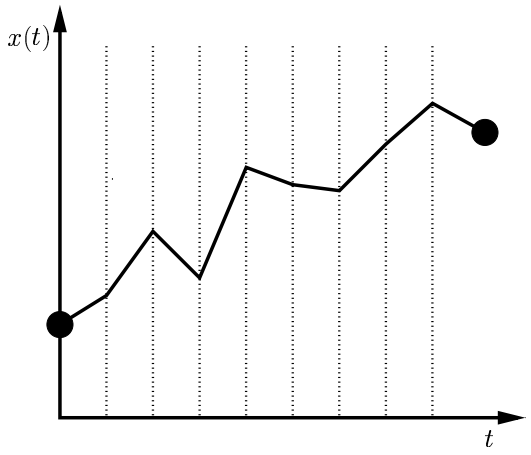

Figure 5.1: A possible path through space and time. The dotted lines indicate possible positions through which a path could pass at each time slice. The propagator integrates over all such possible positions, keeping the end points fixed.

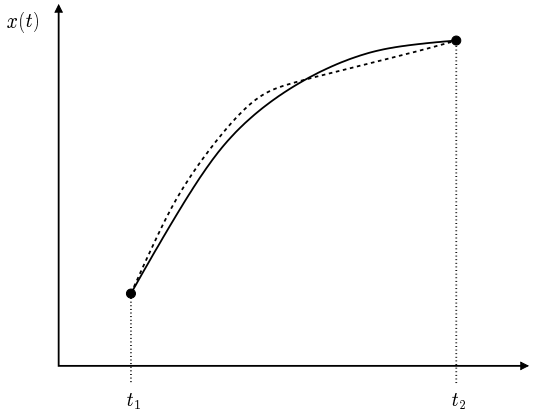

Figure 5.2: Height of a ball thrown upwards in a gravitational field as a function of time. The solid line shows the classical path, and the broken line shows a line which is *close* to the classical path. The trajectory is a trade-off between the desire for a large potential energy as soon as possible against the resulting large kinetic energy.

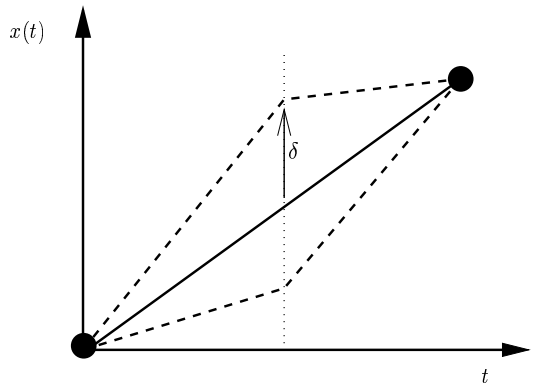

Figure 5.3: Illustration of the deviation δ from the classical path at a single slice in time.

5.3.2 Form of the propagator

Refer again to Figure 5.1, and note that time is divided into a series of slices. The summation over all possible paths is achieved by summing over all possible positions at each time slice. With this in mind, we examine the form of the propagator as given in Equation 5.3:

$$\hat{u}(x',t';x,t) = \int_{x(t)=x}^{x(t')=x'} \overline{\mathrm{D}}x(t'') \exp\left\{\frac{\mathrm{i}}{\hbar} S[x(t'')]\right\}. \tag{5.3}$$

$\overline{\mathrm{D}}x$ denotes integrations over all possible positions at each time slice. A rigorous derivation of this result starting from Schrödinger's equation is given in Appendix A.

When $S[x]$ is a minimum, its first order correction with respect to small changes in x is *zero*. The exponential terms corresponding to paths close to the $S[x] =$ minimum path have similar phases and will tend to *constructively* interfere, thereby increasing the value of $\hat{u}(x',t';x,t)$. Conversely, far away from the action minimum the larger phase difference between neighbouring paths will cause the exponentials to *destructively interfere*. The most probable paths are therefore those close to the $S[x]$ path.

Figure 5.3 defines a quantity δ which represents the magnitude of deviation from the straight line trajectory of a free particle at a single time slice. The real part of the complex exponential in the propagator is shown as a function of δ for two wildly different particle masses in Figure 5.4. Note that the spatial frequency of oscillation increases with increasing $|\delta|$. As the action is increased, neighbouring paths have more wildly different phases; when all possible paths are summed over, paths with

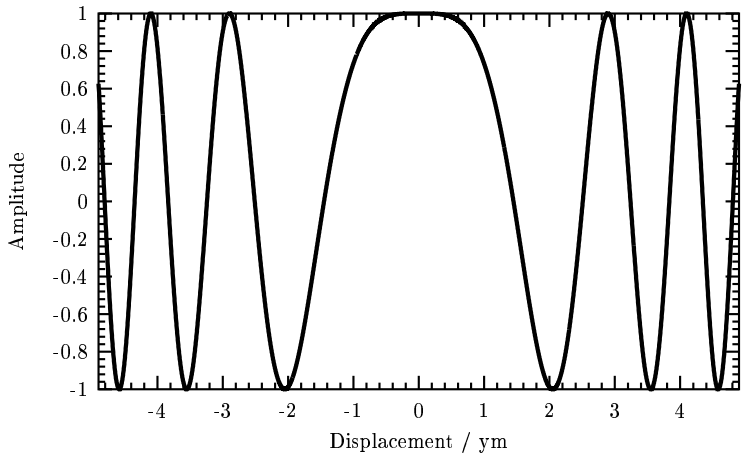

(a) 1 kg mass.

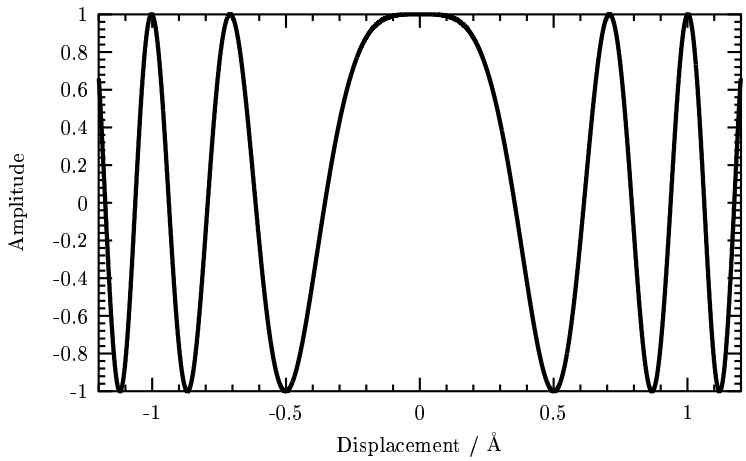

(b) Hydrogen nucleus.

Figure 5.4: Real part of the complex exponential for light and heavy free particles, both at room temperature.

high action tend to destructively interfere and cancel each other. On careful examination of the scales on the abscissa axes, there is a striking difference between the spatial frequency corresponding to the two masses. For the 1 kg mass, the magnitude of δ at which phase cancellation begins to set in is vanishingly small. This is not so for the hydrogen nucleus; here the magnitude of δ out to the first trough is about 0.5 Å, which is on a par with the length scales found in the microscopics of water. The quantum delocalisation of hydrogen nuclei — even at room temperature — can be seen to be non-negligible.

5.3.3 Classical and quantum regimes

We have seen the importance of the location of the action minimum and touched on differences between classical and quantum behaviour for the 1 kg mass and the hydrogen nucleus respectively. Let us now ponder further the significance of the *magnitude* the action at its minimum. We note that $S[x]$ is dimensionally equivalent to $\hbar$, and $[\hbar] =$ Js. Energies in the microscopic world are so very much smaller than in the macroscopic world ($k_{\mathrm{B}}T \approx \frac{1}{40}$ eV at room temperature), hence the action for a microscopic particle will also be very much smaller. We see, then, that we enter the quantum regime when the action becomes of the order of $\hbar$. The oscillation of the exponential term over neighbouring paths becomes much less wild, and there is more tolerance in how far a path can stray from the $S[x]$ = minimum or the classical path before cancellation between neighbouring paths begins to occur.

5.4 Path integrals in imaginary time

In this section we shall see that it is possible to express the trace over the quantum density matrix as a classical partition function in imaginary time.

5.4.1 Propagators as density matrices

We begin with the density matrix itself, as given in Equation 5.4:

$$\rho(x,y) = \sum_n \phi_n(x)\phi_n^*(y)\mathrm{e}^{-\beta E_n} \tag{5.4}$$

The partition function for the system is then given by

$$Z = \int_{-\infty}^{+\infty} \rho\left(x,x\right)\mathrm{d}x = \mathrm{Tr}\left[\rho\right]. \tag{5.5}$$

Consider now the quantum mechanical state vector expanded on a complete set of eigenstates of position. To evolve the state vector through time, the appropriate time evolution operator is applied to each of the eigenstates. Expressions for the wavefunction at time 0 and a later time t are given in Equation 5.6.

$$|\Psi(x,0)\rangle = \sum_{n=1}^{\infty} c_n |\phi_n(x)\rangle \tag{5.6a}$$

$$|\Psi(x,t)\rangle = \sum_{n=1}^{\infty} c_n \mathrm{e}^{-\frac{\mathrm{i}E_n t}{\hbar}} |\phi_n(x)\rangle \tag{5.6b}$$

We have that

$$c_n = \langle \phi_n(y) \, | \Psi(y,0) \rangle \tag{5.7}$$

and Equation 5.6b therefore becomes

$$|\Psi(x,t)\rangle = \sum_{n=1}^{\infty} |\phi_n(x)\rangle \, \langle \phi_n(y) \, | \Psi(y,0) \rangle \, \mathrm{e}^{-\frac{\mathrm{i}E_n t}{\hbar}}. \tag{5.8}$$

If we now make the time variable *imaginary* such that $t = -\mathrm{i}\beta\hbar$ and drop out of Dirac notation, we find

$$\Psi(x, -\mathrm{i}\beta\hbar) = \int_{-\infty}^{+\infty} \sum_{n=1}^{\infty} \phi_n(x)\phi_n^*(y)\mathrm{e}^{-\beta E_n} \Psi(y,0) \, \mathrm{d}y. \tag{5.9}$$

Note that Equation 5.9 takes the form of a path integral as expressed in Equation 5.1. Further, the corresponding propagator takes the form

$$\hat{u}(x, -\mathrm{i}\beta\hbar; y, 0) = \sum_{n=1}^{\infty} \phi_n(x)\phi_n^*(y)\mathrm{e}^{-\beta E_n} \tag{5.10}$$

which is nothing less than the quantum density matrix! This is a very important result. It tells us that the path of a particle through *imaginary* time describes its *quantum* characteristics. This notion is elucidated in Subsection 5.4.2.

5.4.2 Path integral as a partition function

We saw above that the path integral propagator is formally equivalent to the quantum density matrix when the time variable is imaginary.

Imaginary time may be thought of as a parameter which allows us to add quantum characteristics onto a classical world; if we were to look along the axis of imaginary

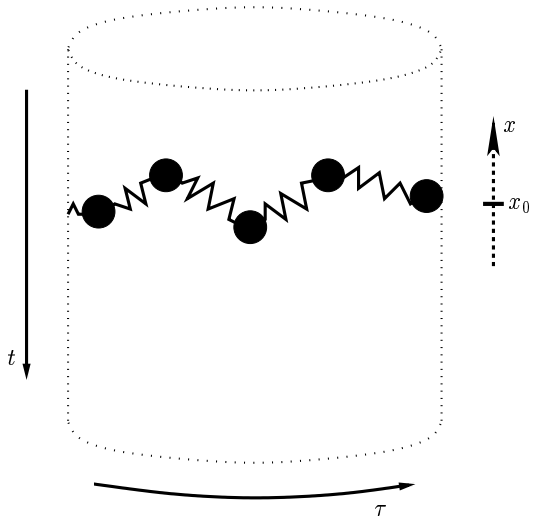

Figure 5.5: At any slice in *real* time t there is a range of positions in the quantum distribution of a particle parameterised by *imaginary* time τ. Black circles represent possible positions in the quantum spread, and the jagged lines which connect them represent harmonic springs. The position x_0 denotes the mean or *centroid* position of the particle.

time — as we do when we take a snapshot at a single slice in real time — we would see all possible positions of the particle at that moment in real time. This is illustrated in Figure 5.5. For a classical particle, the path would be a straight line; the position would remain to be x_0 for all points in imaginary time. However in the quantum world there is some freedom to deviate from this preferred path and we see some spread in position. We shall return to Figure 5.5 when we discuss path integral molecular dynamics in Section 5.5.

To show that the above concept is justified, we follow Simons (2000) and find the partition function for a piece of string in an external potential, as shown in Figure 5.6. The string represents the path of a quantum particle through imaginary time.

The ends of the string correspond to the same point in x. Let a small portion $\mathrm{d}\tau$ be displaced by an amount $\mathrm{d}\left[x(\tau)\right]$. Assuming that the displacement is sufficiently small to allow the tension T to remain constant, the potential energy stored in the string due to its extension $\mathrm{d}\tau$ is[1]

[1]Using the compact notation $\mathrm{d}_\tau x \equiv \frac{\mathrm{d}x}{\mathrm{d}\tau}$

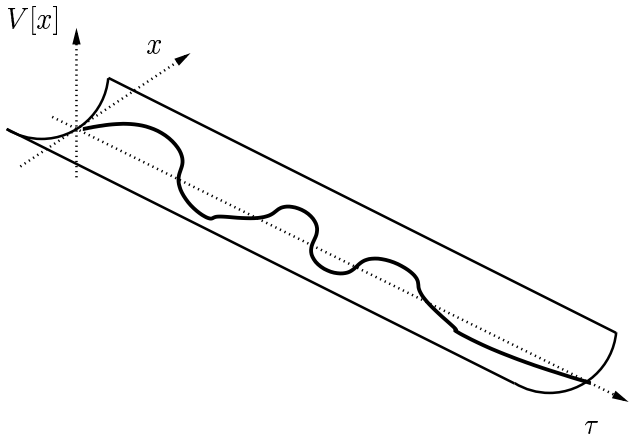

Figure 5.6: A piece of string in an external potential, representing a path through imaginary time. We will find that we can sample possible quantum states by considering the motion of this string dynamically in a simulation.

$$\begin{aligned}
\mathrm{d}V_1 &= T\left[\sqrt{\mathrm{d}\tau^2+\mathrm{d}x^2}-\mathrm{d}\tau\right] \\
&= T\mathrm{d}\tau\left[\sqrt{1+\left(\frac{\mathrm{d}x}{\mathrm{d}\tau}\right)^2}-1\right] \\
&\simeq T\mathrm{d}\tau\left\{1+\frac{1}{2}\left(\frac{\mathrm{d}x}{\mathrm{d}\tau}\right)^2+O\left[\left(\frac{\mathrm{d}x}{\mathrm{d}\tau}\right)^2\right]^2-1\right\} \\
&\simeq \frac{T}{2}\left(\mathrm{d}_\tau x\right)^2\mathrm{d}\tau
\end{aligned} \tag{5.11}$$

Integrating over the whole string,

$$V_1\left[\mathrm{d}_\tau x\right] = \frac{T}{2}\int_0^L \left(\mathrm{d}_\tau x\right)^2\mathrm{d}\tau \tag{5.12}$$

where L is the total length of the string.

We have a second contribution to the total potential energy from the *external* potential $V(x)$. If length element $\mathrm{d}\tau$ contributes an energy $V\left[x(\tau)\right]\mathrm{d}\tau$ to the total energy.

$$V_2\left[x(\tau)\right] = \int_0^L V\left[x(\tau)\right]\mathrm{d}\tau \tag{5.13}$$

The total potential energy is just $V_{\mathrm{tot}} = V_1 + V_2$. We may now write down the *partition function* for the string:

$$\begin{aligned} Z &= \int_{-\infty}^{+\infty} \mathrm{d}x_0 \int \mathrm{D}x(\tau) \exp\left(-\beta V_{\mathrm{tot}}\right) \\ &= \int_{-\infty}^{+\infty} \mathrm{d}x_0 \int \mathrm{D}x(\tau) \\ &\qquad \exp\left\{-\beta \int_0^L \mathrm{d}\tau \left[\frac{T}{2}\left(\frac{\mathrm{d}x}{\mathrm{d}\tau}\right)^2 + V\left[x(\tau)\right]\right]\right\}. \end{aligned} \tag{5.14}$$

Note that we must perform the function integral over all space *and* integrate over all possible start (and consequently end) points.

We may recover the classical limit by noting that if the kinetic term is small, access to positions x far from the average — corresponding to different potentials $V[x]$ — will be restricted. In other words so long as deviations from the straight path are small, the kinetic term becomes negligible and the potential will remain approximately constant. In this case we can write

$$Z = \int \mathrm{d}x_0 \, \mathrm{e}^{-\beta V(x_0)} \tag{5.15}$$

This is just the partition function familiar from classical statistical mechanics! Note that the functional integral has vanished, since there is no deviation in imaginary time from x_0.

Having found the partition function for the string, we now show that we may obtain the same result by considering the path integral in imaginary time. First recall the path integral propagator:

$$\hat{u}(x', t'; x, t) = \exp\left[\frac{\mathrm{i}}{\hbar}\int_t^{t'} \mathrm{d}t'' \left(\frac{m}{2}\dot{x}^2 - V(x)\right)\right] \tag{5.16}$$

Let us make the switch to *imaginary time*, such that $\tau = \mathrm{i}t$. It follows that

$$\frac{\mathrm{d}x}{\mathrm{d}t} = \mathrm{i}\frac{\mathrm{d}x}{\mathrm{d}\tau} \tag{5.17a}$$

$$\left(\frac{\mathrm{d}x}{\mathrm{d}t}\right)^2 = -\left(\frac{\mathrm{d}x}{\mathrm{d}\tau}\right)^2 \tag{5.17b}$$

Using Equation 5.17b in Equation 5.16 we obtain

$$\hat{u}(x', \tau'; x, \tau) = \int \overline{\mathrm{D}}x(\tau'') \exp\left\{-\frac{1}{\hbar}\int_{\tau}^{\tau'} \mathrm{d}\tau'' \left[\frac{m}{2}\left(\frac{\mathrm{d}x}{\mathrm{d}\tau''}\right)^2 + V[x]\right]\right\} \quad (5.18)$$

Compare this with Equation 5.14. The path integral has the analytic form of the partition function for the string when the "time" variable is imaginary!

Taking the kinetic (tension) contribution as being negligible

$$\hat{u}(x_0, \tau'; x_0, \tau) = \left(\frac{m}{2\pi\hbar(\tau' - \tau)}\right)^{\frac{1}{2}} \exp\left\{-\frac{(\tau' - \tau)}{\hbar} V(x_0)\right\} \quad (5.19)$$

Also, we integrate the propagator around a closed loop such that
$x_0 = x(\tau = 0) = x(\tau = \beta\hbar)$:

$$\hat{u}(x_0, \beta\hbar; x_0, 0) = \left(\frac{m}{2\pi\hbar(\beta\hbar - 0)}\right)^{\frac{1}{2}} \exp\left\{-\frac{(\beta\hbar - 0)}{\hbar} V(x_0)\right\} \quad (5.20)$$

If we now integrate the propagator over all possible beginning (and consequently end points), we observe

$$\int \hat{u}(x_0, \beta\hbar; x_0, 0)\, \mathrm{d}x = Z_{\text{classical}} = \sqrt{\frac{m}{2\pi\hbar^2\beta}} \int e^{-\beta V(x_0)} \mathrm{d}x_0 \quad (5.21)$$

which is again the classical partition function, only now the multiplicative constant is known - this was not possible in classical physics.

5.4.3 Topology

Recall that in Subsection 5.4.2 we integrated around a *closed loop* when evaluating the partition function; the paths which were integrated over began and ended on the same point in space.

Compare the expression for the partition function in Equation 5.5 with the propagator of Equation 5.10. We obtain *diagonal* elements of the quantum density matrix when paths begin and end on the same point; the partition function is then given by the sum of those diagonal elements.

So then the path integral has periodic boundary conditions in imaginary time, with a period of $\Delta\tau = \beta\hbar$. Refer again to Figure 5.5, there a path integral loop is stretched around the curved surface of a cylinder.

5.5 Path integral molecular dynamics

We now move on to discuss how path integrals may be incorporated into molecular dynamics simulation.

5.5.1 Discretisation

Section 5.4 revealed that a quantum particle may be thought of as a loop in real space and imaginary time, which begins and ends on the same point in space. As we traverse the axis of imaginary time we cycle though possible position realisations of the particle. In reality the loop is continuous, but we must discretise it in order to represent it inside a computer.

Denoting then number of points in imaginary time as P, the *continuous* path integral takes the form

$$\hat{u}(x',\tau';x,\tau) = \lim_{P\to\infty} \int \mathrm{d}x_P \cdots \mathrm{d}x_1 \left(\frac{m}{2\pi\hbar\Delta\tau}\right)^{\frac{P}{2}} \exp\left\{-\frac{1}{\hbar}\int_{\tau}^{\tau'} \mathrm{d}\tau'' \left[\frac{m}{2}\left(\frac{\mathrm{d}x}{\mathrm{d}\tau''}\right)^2 + V[x]\right]\right\}. \quad (5.22)$$

Since we are integrating over an imaginary time period of $\tau' - \tau = \beta\hbar$, it then follows that $\Delta\tau'' = \frac{\beta\hbar}{P}$. We may then write down the discrete form of the imaginary time propagator, and hence the discrete partition function Z_P:

$$\begin{aligned} Z \simeq Z_P &= \left(\frac{mP}{2\pi\beta\hbar^2}\right)^{\frac{P}{2}} \int \mathrm{d}x_P \cdots \mathrm{d}x_1 \\ &\qquad \exp\left\{-\frac{1}{\hbar}\sum_{s=1}^{P} \frac{\beta\hbar}{P}\left[\frac{m}{2}\left(\frac{\Delta x}{\Delta\tau''}\right)^2 + V[x]\right]\right\} \\ &= \left(\frac{mP}{2\pi\beta\hbar^2}\right)^{\frac{P}{2}} \int \mathrm{d}x_P \ldots \mathrm{d}x_1 \\ &\qquad \exp\left\{-\beta\sum_{s=1}^{P}\left[\frac{mP}{2\beta^2\hbar^2}(x_{s+1}-x_s)^2 + \frac{V(x_s)}{P}\right]\right\} \end{aligned} \quad (5.23)$$

Note that the exponential term in Equation 5.23 as the form $\exp -\beta H$ with Hamiltonian

$$H = \frac{1}{2}\frac{mP}{\beta^2\hbar^2}(x_{s+1} - x_s)^2 + \frac{V(x_s)}{P}. \tag{5.24}$$

That is to say, upon discretisation we may represent a path integral loop as a series of balls in a loop topology connected with springs. We may easily read off the required spring constant from Equation 5.24:

$$C = \frac{mP}{\beta^2\hbar^2} = \frac{mP(k_{\mathrm{B}}T)^2}{\hbar^2} \tag{5.25}$$

We shall address the question as to how many path integral beads are required in Subsection 5.5.6.

5.5.2 The classical limit

As temperature is increased, the length of the path through imaginary time — given by $\beta\hbar = \frac{\hbar}{k_{\mathrm{B}}T}$ — becomes smaller, tending to zero in the limit of infinitely high temperature. In addition, the spring constant expressed in Equation 5.25 increases. So then, we may recover the classical particle by considering the high temperature path integral loop; stiff springs prevent the position from deviating very far from the centroid position x_0 over the path and the path itself becomes shorter, reducing to a point in the limit of infinite temperature.

We also note that the spring constant is mass dependent. Small masses result in floppy springs, allowing greater deviation from the centroid position x_0; lighter particles suffer greater delocalisation.

5.5.3 Sampling

Refer again to Figure 5.5. There we see a schematic representation of a quantum particle in molecular dynamics simulation. At any slice in real time t, the chain of balls and springs which form the path integral loop take one path through imaginary time; a path sampled from the distribution of possible paths. As real time progresses — that is, as the path integral loop slides down the "tube" in Figure 5.5, the *centroid* or "classical" position of the particle x_0 samples possible points in phasespace. At the same time, the shape of the path through imaginary time is constantly changing, hence sampling possible paths through imaginary time. In sampling possible paths through *imaginary* time, possible positions are sampled of a quantum particle at a

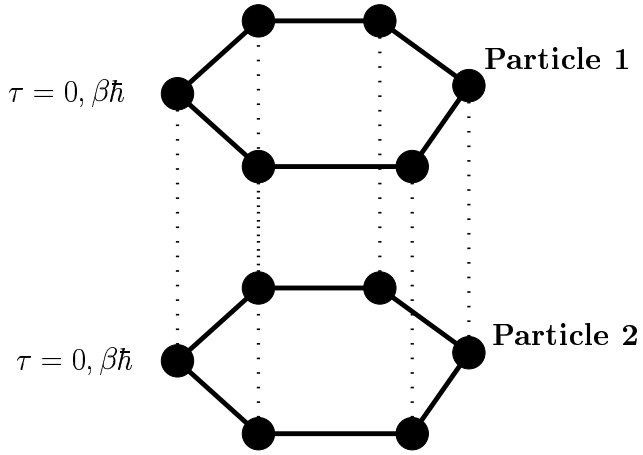

Figure 5.7: Two rings in imaginary time representing two quantum particles. The solid lines indicate harmonic interactions, whereas the dotted lines indicate interactions due to the external potential.

single slice in *real* time. Note that we do not see *real time quantum dynamics*, since we only ever sample one path through imaginary time for any slice in real time.

In Chapter 3 the idea of phasespace sampling was introduced; through the ergodic hypothesis, time averages from molecular dynamics simulation become equivalent to ensemble averages. We may now take this idea a little further and say that by averaging over all real *and* imaginary time, we have access to *quantum* ensemble averages.

5.5.4 Interactions

We have already discussed how the beads for a single particle experience harmonic interactions with adjacent beads in imaginary time. Figure 5.7 illustrates how the *external* potential enters the scene.

Just as the potential energy and forces depend on the phasespace configuration at a single slice real time only, the same is true through imaginary time. As far as the external potential is concerned, path integral particles only interact with one another for independent slices in imaginary time; beads on the necklace for one particle only see their counterparts on other atoms corresponding to the same point in imaginary time. Note that Equation 5.24 tells us that each path integral bead only feels one P^{th} of the calculated external potential.

5.5.5 Radius of gyration

The *radius of gyration* (RGY) of a particle is defined as the root mean square displacement of its path integral beads from the centroid position. We can define a radius-of-gyration matrix, given in Equation 5.26,

$$\Delta^2_{\alpha\beta} = \frac{1}{P}\left\langle \sum_{s=1}^{P} (r_s^\alpha - \overline{r}^\alpha)(r_s^\beta - \overline{r}^\beta) \right\rangle \tag{5.26}$$

where α and β are Cartesian directions (x, y, z), $\overline{r}$ represents the centroid position of the particle, and P is the number of path integral beads. Equation 5.26 can be rearranged for ease of computation to the form given in Equation 5.27

$$\Delta^2_{\alpha\beta} = \frac{1}{P}\left\langle \sum_{s=1}^{P} r_s^\alpha r_s^\beta \right\rangle - \left\langle \overline{r}^\alpha \overline{r}^\beta \right\rangle \tag{5.27}$$

To allow for the possibility that a path integral ring for a single particle lies across the simulation cell boundary, all beads for that particle must have the minimum image criterion applied to them with respect to the first bead in imaginary time.

5.5.6 Convergence

In Subsection 5.5.1 it was seen that the path integral loop for a quantum particle must be discretised in order to represent it inside a computer. How many beads are required on the path integral loop? The radius of gyration provides a convenient indicator of this; the number must be high enough to converge the degree of quantum delocalisation. It would be a waste of resources to perform a path integral calculation with many more path integral beads than strictly necessary, as such a calculation would not yield any more physical insight than a calculation with a *sufficient* number of beads.

In applying path integral methods to TIP5P water, Mahoney and Jorgensen (2001) note that $P = 5$ is a sufficient number for convergence. Further, the TIP5P(PI) potential used presently was paratmeterised by Mahoney and Jorgensen using discretisation of this degree. It is therefore the $P = 5$ prescription which we use here.

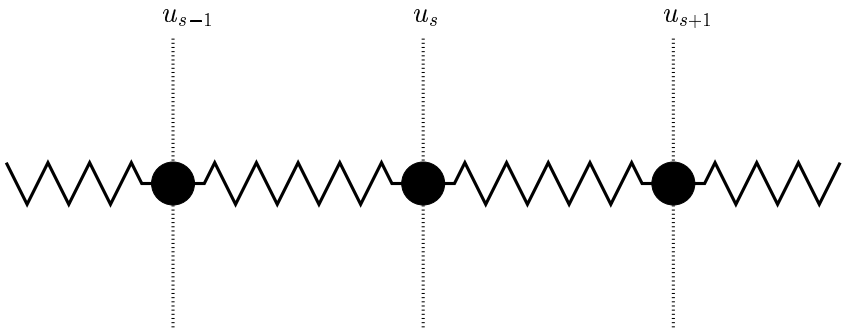

Figure 5.8: Illustration of a path integral segment. The circles represent path integral beads, and the jagged lines represent the connecting springs. u_s denotes the displacement of bead s from its equilibrium position.

5.5.7 Vibrational modes

In order to ensure ergodicity in both real *and* imaginary time, the Langevin thermostat described in Chapter 3 was applied separately for each point in imaginary time; that is to say, the same random forces were *not* applied to all beads corresponding to a given particle.

In the same way in which it is desirable for the Langevin damping time to be about a factor of ten larger than the the slowest mode of interest in a classical system, we also desire that the Langevin damping time is a similar relation to the slowest vibrational mode of a path integral loop. To evaluate the slowest mode we may borrow mathematics familiar from solid state physics, such as that given by Kittel (1996) which we shall follow here.

We first write down the equation of motion for a single bead of a path integral loop, as illustrated in Figure 5.8:

$$m\frac{\mathrm{d}^2 u_s}{\mathrm{d}t^2} = C\left(u_{s-1} - u_s\right) + C\left(u_{s+1} - u_s\right). \tag{5.28}$$

Trying solutions of the form

$$u_{s\pm1} = u_0 \mathrm{e}^{+\mathrm{i}ska}\mathrm{e}^{\pm\mathrm{i}ka} \tag{5.29}$$

we find

$$-m\omega^2 u_s = C\left(u_{s+1} + u_{s-1} - 2u_s\right) \tag{5.30}$$

and hence

$$\omega^2 = \frac{2C}{m}\left[1 - \cos(ka)\right] \tag{5.31}$$

or

$$\omega = \left(\frac{4C}{m}\right)^{\frac{1}{2}} \left|\sin\left(\frac{ka}{2}\right)\right|. \tag{5.32}$$

Recall that the path integral ring has a "circumference" of $\tau = \beta\hbar$. The allowed wavenumbers are then given by

$$k\beta\hbar = 2n\pi \tag{5.33}$$

The lowest wavenumber corresponds to $n = 1$, and we may therefore write

$$\omega = \left(\frac{4C}{m}\right)^{\frac{1}{2}} \left|\sin\left(\frac{\pi}{P}\right)\right|. \tag{5.34}$$

Substituting in the spring constant revealed in Equation 5.25, we find

$$\omega = \frac{\sqrt{4P}}{\beta\hbar} \left|\sin\left(\frac{\pi}{P}\right)\right|. \tag{5.35}$$

Of course, a path integral *loop* cannot be linear everywhere, rendering the above analysis nothing more than an approximation. However, it may be seen from Equation 5.28 that the resultant force on any one bead due to the harmonic interaction is *smaller* than if it were attached to only one nearest neighbour; the forces due to both nearest neighbours in Figure 5.8 partially cancel, resulting in a smaller frequency of oscillation in simple harmonic oscillator theory. The linear chain, then, represents the configuration which yields the vibrational mode with the lowest possible frequency or longest possible period. This is sufficient for our needs, as we wished to ensure that the Langevin damping time of Section **??** is *longer* than the lowest frequency mode of the path integral loop.

For a temperature T = 275 K (the lowest used presently) and five path integral beads, the lowest possible period of oscillation was found to be t_{lowest} = 0.2 ps, which is at least a factor of ten smaller than the Langevin damping times used for both light and heavy water, as given in Section **??**. It should be noted that this figure is the same for both light and heavy water, since the bead mass drops out of the equations above.

5.6 Particular cases

In Subsection 5.5.5 we met the radius of gyration of a quantum particle. Here we consider the theoretical radius of gyration for the simplest non-zero external potential — the harmonic potential — and also that for the free particle.

5.6.1 Harmonic oscillator

The expression for the radius of gyration for the harmonic oscillator in one dimension is given by Gillan (1988), and its functional form is derived in Appendix A:

$$\Delta^2 = \frac{1}{\beta m \omega_0^2}\left[\frac{1}{2}\beta\hbar\omega_0 \coth\left(\frac{1}{2}\beta\hbar\omega_0\right) - 1\right]. \tag{5.36}$$

In Chapter 6 we shall be concerned not only with the magnitude of Δ, but also with its uncertainty; we therefore find here derivatives required for the estimation of uncertainties.

Noting the relation $\omega_0 = \sqrt{C/m}$ we may propagate the error in the spring constant C to find the corresponding theoretical error on the radius of gyration in a given direction. Defining

$$\alpha = \frac{\beta\hbar C^{\frac{1}{2}}}{2m^{\frac{1}{2}}} \tag{5.37}$$

and noting that $\omega_0 = \sqrt{C/m}$ for the harmonic oscillator, we may re-write Equation 5.36 as

$$\Delta^2 = \frac{k_\mathrm{B}T}{C}\left[\alpha\coth(\alpha) - 1\right]. \tag{5.38}$$

The required derivatives are then:

$$\frac{\partial\Delta}{\partial C} = \left(\frac{1}{4\beta C^3}\right)^{\frac{1}{2}}\left[\alpha\coth(\alpha) - 1\right]^{\frac{1}{2}} + \frac{\hbar}{8C}\left(\frac{\beta}{m}\right)^{\frac{1}{2}}\frac{\left[\coth(\alpha) - \alpha\,\mathrm{csch}^2(\alpha)\right]}{\left[\alpha\coth(\alpha) - 1\right]^{\frac{1}{2}}} \tag{5.39}$$

and

$$\frac{\partial \Delta}{\partial T} = \left(\frac{k_{\mathrm{B}}}{4TC}\right)^{\frac{1}{2}} \left[\alpha \coth(\alpha) - 1 + \frac{\alpha^2 \operatorname{csch}^2(\alpha) - \alpha \coth(\alpha)}{\alpha \coth(\alpha) - 1}\right]. \tag{5.40}$$

5.6.2 Free particle

The radius of gyration for the free particle may be found by taking the limit as $\omega_0 \to 0$ of the expression for the harmonic oscillator seen in Equation 5.36.

Substituting for $\cosh(x)$ & $\sinh(x)$ with their exponential representations and keeping only leading terms, we find

$$\Delta^2 = \frac{\hbar^2}{12mk_{\mathrm{B}}T}. \tag{5.41}$$

Further, the derivative with respect to the temperature T is also of interest for estimating the uncertainty on Δ in Chapter 6.

$$\frac{\partial \Delta}{\partial T} = -\frac{1}{2}\frac{\hbar}{\sqrt{12mk_{\mathrm{B}}T^3}} \tag{5.42}$$

5.7 Summary

The path integral formulation of quantum mechanics concerns itself with possible paths through space and time; likely paths are those which constructively interfere with their neighbours. The trace of the quantum density matrix may be expressed as a classical partition function in imaginary time, thus providing a neat bridge between the domains of quantum and statistical mechanics. Motion in imaginary time may be thought of as a way of adding quantum effects to a classical world.

Incorporating path integrals into molecular dynamics allows a particle to explore likely paths through imaginary time, and further to explore possible centroid positions; this extends the ensemble averages of classical molecular dynamics to *quantum ensemble averages* for the system.

Chapter 6

Delocalisation

6.1 Introduction

In this chapter we shall take a look at the magnitude of quantum delocatisation on activation of the quantum treatment of nuclei. Figure 6.1 shows a shapshot of water taken from such a calculation. The white hydrogen atoms take on a "cloud-like" character; each one is seen there as a few possible position realisations at a single slice in real time.

Our principal tool for measuring the magnitude of delocalisation will be the radius of gyration tensor, as introduced in Subsection 5.5.5. For non-spherical delocalisation, the RGY tensor will be in general highly non-diagonal. To extract meaningful information from PI simulation, the RGY matrix was diagonalised, yielding a set of three eigenvalues representing the magnitude of delocalisation in three orthogonal spatial directions. The mean square delocalisation — or deviation from the centroid position — is represented in the following sections by relative frequency plots. There are three such plots for each atomic species: the lowest eigenvalue[1] for each atom, followed by the second lowest and finally the highest.

Section 6.3 looks at the behaviour of the RGY at temperatures surrounding the TMD. The effect of compression and isotopic substitution is addressed in Sections 6.4 and 6.5 respectively, Section 6.6 considers radii of gyration from harmonic oscillator theory and Section 6.7 brings the chapter to close.

[1] That is to say, the eigenvalue with the lowest *magnitude*.

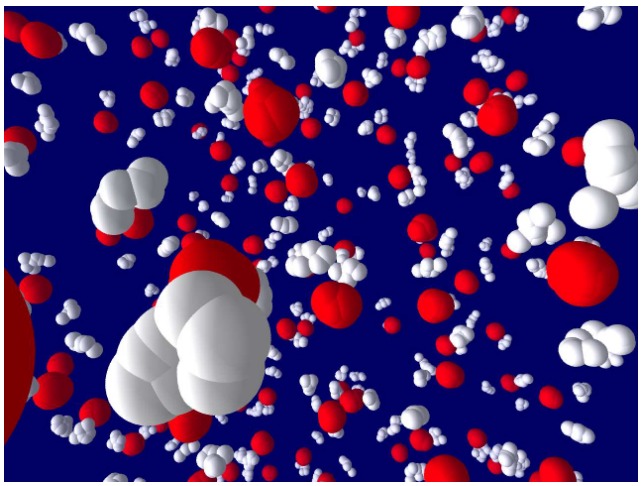

Figure 6.1: Path integral water. All points in imaginary time corresponding to a single slice in real time are compacted into one image. Oxygen atoms are shown in red, and hydrogen atoms in white.

6.2 General features

Figure 6.2(a) shows the magnitude of the delocalisation present in hydrogen atoms at temperatures spanning the TMD. We first note that the quantum distribution for hydrogen atoms takes on a distinctly non-spherical shape; if atoms were delocalised in a spherical manner, the distributions for all three spatial directions would peak at the same location. The different magnitudes are characterised by three eigenvalues $(\lambda_1, \lambda_2, \lambda_3)$, with λ_1 and λ_3 representing the smallest and largest delocalisations respectively.

The smallest delocalisation maintains a finite probability at zero deviation from the centoid position. This may understood by noting that the hydrogen atoms are part of geometrically constrained water molecules, restricting scope for delocalisation in the intramolecular OH bond direction. Inspection of the equivalent curves for oxygen atoms in Figure 6.2(b) reveal a peak in a comparable position to that for the smallest hydrogen delocalisation; the molecule is effectively delocalised as one particle — a point to which we shall return in Subsection 6.6.3.

We may analyse further the relationship between anisotropic delocalisation and the behaviour of the molecule as a whole using the molecule-fixed axes illustrated in Figure 6.3; the effect these delocalisations have on the wider molecule is summarised in Table 6.1. Referring to Figure 6.4(a) we see the distribution of scalar products between eigenvectors of the RGY tensor and molecule-fixed axes for each hydrogen atom.

First note that the peak corresponding to the direction $\boldsymbol{y}$ is drawn by the eigenvector

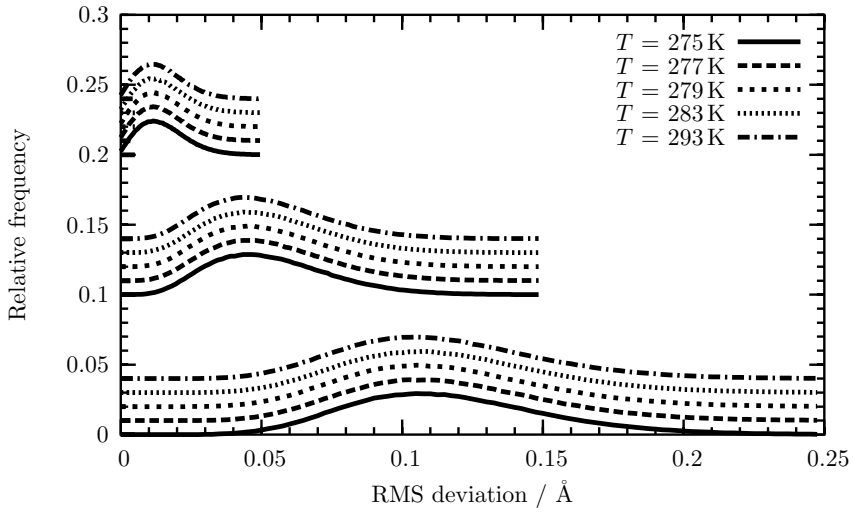

(a) Hydrogen.

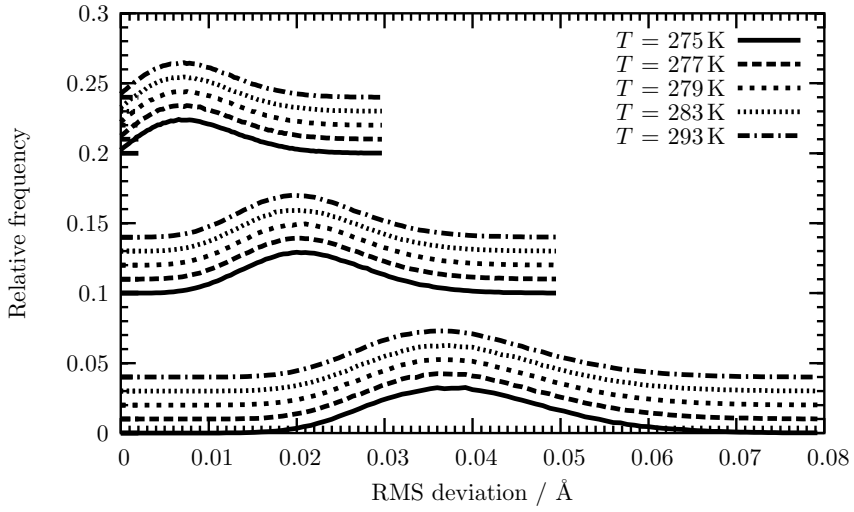

(b) Oxygen.

Figure 6.2: Distribution of the RMS delocalisation of atoms along the three principal axes for a range of different temperatures, including a vertical separation of 0.01 for clarity. Top to bottom: λ_1, λ_2 and λ_3 within each figure. The water was at $\rho = 1.0\,\mathrm{g\,cm^{-3}}$ density.

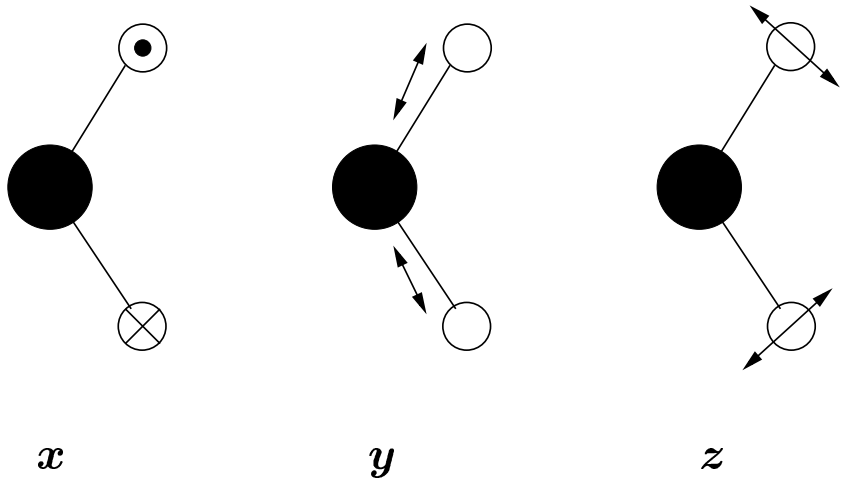

Figure 6.3: Directions of basis axes used for studying quantum delocalisation. For each atom, an orthogonal basis set was constructed using the molecular geometry. Only the magnitude of the delocalisation in each direction is of interest; as such, each axis here is bi-directional. It should be noted that arrows do not indicate indicate motion around the oxygen atom, but rather the molecular centre of mass; as such there are equivalent degrees of freedom for the oxygen atom.

corresponding to the lowest eigenvalue. This confirms the earlier observation that the OH bond constraint is indeed restricting the magnitude of delocalisation in that direction.

Delocalisation in the other two orthogonal directions is not so clearly tied to any one eigenvalue. That is to say, there is some overlap as to which direction commands the largest delocalisation at a given instant; this is evident in the upward inflection of the curves corresponding to λ_2 *and* λ_3 in Figure 6.4(a). We may, however, deduce that the largest delocalisation represented by λ_3 is largely in the x direction. This correponds to uncertainty of molecular orientation either about an axis parallel to the HH separation and/or the line of reflective symmetry (*flapping* and/or *twisting*). The medium eigenvalue λ_2 may be seen to be largely tied to delocalisation in the z direction, which serves to induce uncertainty in molecular orientation about the axis normal to the plane defined by the nuclei.

6.3 Effect of temperature

While it is clear that inclusion of path integrals results in quantum delocalisation with a spread up to a few tenths of an Angstrom for hydrogen, Figure 6.2(a) shows *no* clear variation of the magnitude of delocalisation with temperature as the anomalous region is entered. The eye might suppose that there is a minute shift to larger

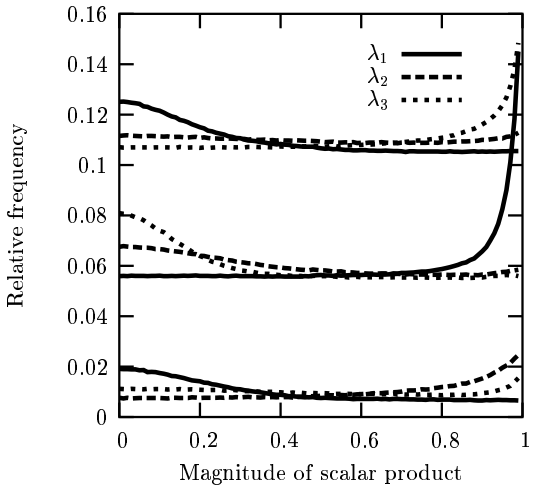

(a) Hydrogen.

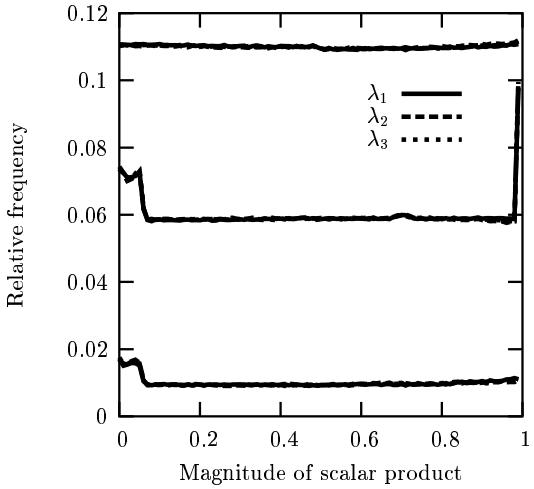

(b) Oxygen.

Figure 6.4: Distributions obtained when each of the three eigenvectors of the RGY tensor for hydrogen are projected onto axes constructed using the molecular geometry, as illustrated in Figure 6.3. The λ_i denote the eigenvalues corresponding to the eigenvectors, with λ_1 being the lowest in magnitude and λ_3 the largest. Relative frequencies corresponding to each axis have been separated by 0.05 for clarity. Top to bottom: $\boldsymbol{x}$, $\boldsymbol{y}$ and $\boldsymbol{z}$ axes. The water was at $\rho = 1.0\,\mathrm{g\,cm^{-3}}$ density and was thermostatted to T = 275 K.

Molecule fixed axis	Description of molecular delocalisation
x	**Twisting** — molecule rotates around line of reflective symmetry. **Flapping** — molecule rotates around axis parallel to the HH separation.
y	**Translation** — molecule translates along directions shown.
z	**Rocking** — rotation around axis perpendicular to the plane of the molecule.

Table 6.1: Descriptions of molecular delocalisation illustrated in Figure 6.3.

values, but it is not at all well resolved.

Figure 6.5(a) shows distributions of scalar product magnitudes in water at room temperature; they bear a striking resemblence to those calculated at T = 275 K. Not only is the magnitude of delocalisation essentially unchanged by varying temperature, but the direction in which those delocalisations occur is similarly unchanged.

6.4 Effect of compression

Further to the lack of significant variation with temperature, there is no apparent change in the radius of gyration when the density is increased by 20% as demonstrated in Figure 6.6; note that the density of *heavy* water at its density maximum is 10% greater than that of light water. Possible differences in the RGY between light and heavy water therefore may not be attributed to the differing densities of the two systems.

Figure 6.7 shows the distribution of scalar product magnitudes of the delocalisation eigenvectors with the fixed molecular axes; the latter does not show any clear differences when compared with the lower density case.

6.5 Isotopic substitution

It has been seen that the radius of gyration measuring the magnitude of the quantum delocalisation in *light* water is essentially unchanged over a range of densities and temperatures with values surrounding those of the density maxima of both light and heavy water.

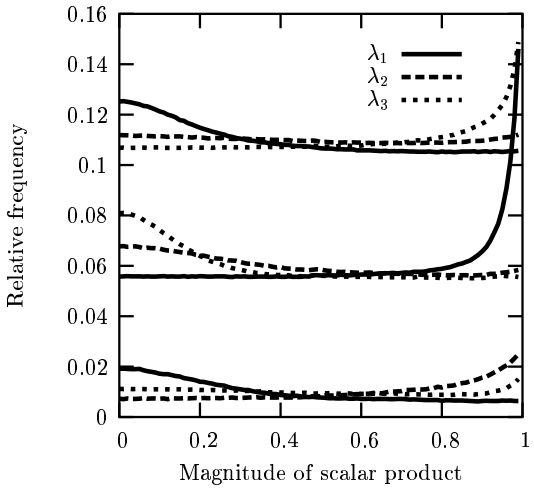

(a) Hydrogen.

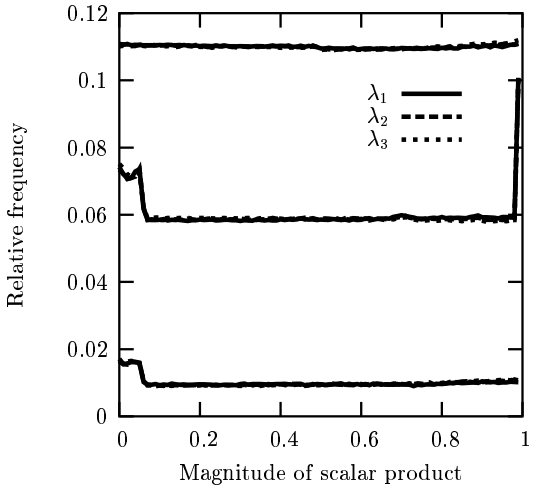

(b) Oxygen.

Figure 6.5: Distributions obtained when each of the three eigenvectors of the RGY tensor for hydrogen are projected onto axes constructed using the molecular geometry, as illustrated in Figure 6.3. The λ_i denote the eigenvalues corresponding to the eigenvectors, with λ_1 being the lowest in magnitude and λ_3 the largest. Relative frequencies corresponding to each axis have been separated by 0.05 for clarity. Top to bottom: $\boldsymbol{x}$, $\boldsymbol{y}$ and $\boldsymbol{z}$ axes. The water was at $\rho = 1.0\,\mathrm{g\,cm^{-3}}$ density and was thermostatted to T = 293 K.

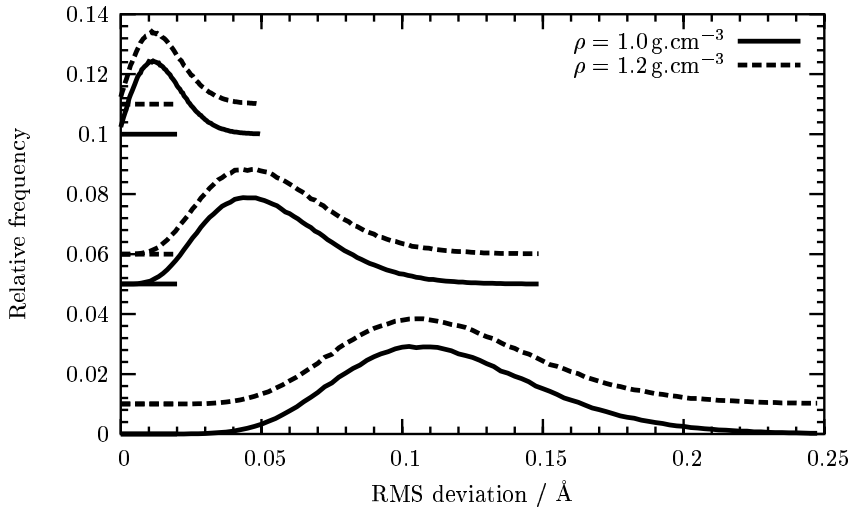

(a) Hydrogen.

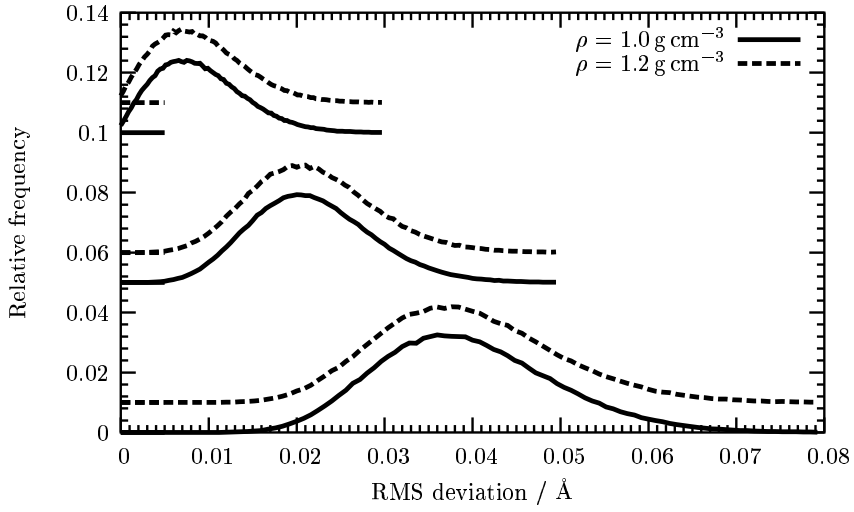

(b) Oxygen.

Figure 6.6: Comparison of the RMS delocalisation of oxygen atoms along the three principal axes at the density maximum compared with water at higher density. The water was thermostatted to T = 277 K in both cases.

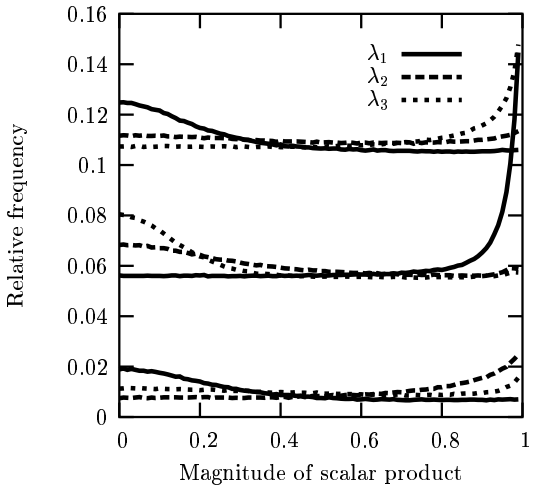

(a) Hydrogen.

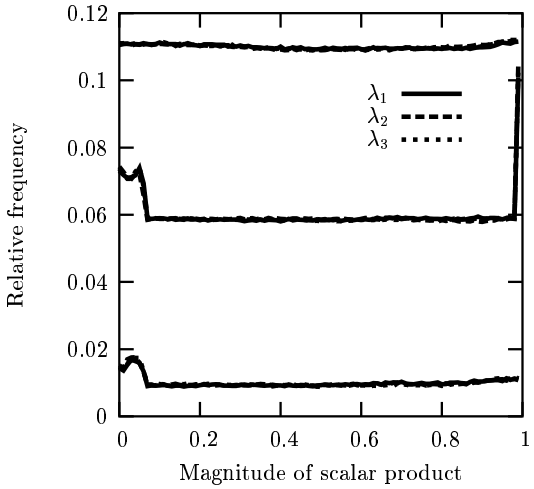

(b) Oxygen.

Figure 6.7: Distributions obtained when each of the three eigenvectors of the RGY tensor for high density water are projected onto axes constructed using the molecular geometry, as illustrated in Figure 6.3. The λ_i denote the eigenvalues corresponding to the eigenvectors, with λ_1 being the lowest in magnitude and λ_3 the largest. Relative frequencies corresponding to each axis have been separated by 0.05 for clarity. Top to bottom: $\boldsymbol{x}$, $\boldsymbol{y}$ and $\boldsymbol{z}$ axes. The density was $\rho = 1.2\,\mathrm{g\,cm^{-3}}$ and the water was thermostatted to $T = 277\,\mathrm{K}$.

Water type	λ_1 / Å	λ_2 / Å	λ_3 / Å
Hydrogen / deuterium delocalisation			
Light *	0.016 ± 0.008	0.05 ± 0.02	0.12 ± 0.04
Heavy †	0.014 ± 0.007	0.04 ± 0.02	0.09 ± 0.03
Oxygen delocalisation			
Light *	0.010 ± 0.005	0.022 ± 0.007	0.04 ± 0.01
Heavy †	0.009 ± 0.007	0.022 ± 0.007	0.04 ± 0.01

* ρ = 1.0 g.cm^{-3} ; T = 277 K
† ρ = 1.1 g.cm^{-3} ; T = 284 K

Table 6.2: Mean values of the eigenvalues of delocalisation λ_1,λ_2 and λ_3 as measured by simulation, together with RMS fluctuations.

We now turn our attention to the effect of doubling the protonic masses, or the effect of replacing hydrogen with deuterium atoms to form *heavy* water. Figure 6.8 shows the distribution of RGY eigenvalues as seen previously for light water. Mean values are given in Table 6.2. Immediately we see that there has been a 25% reduction in the magnitude of the largest eigenvalue, and no clear change in the smallest. There is also a small decrease in the spread in the λ_3 distribution. It is noteworthy that the spread decreases in proportion to the decrease in the mean; that is to say, the spread decreases such that the *relative* fluctuations remain at 33%. We shall put the oxygen delocalisation aside, since there is no well-resolved change there.

Distributions of scalar product magnitudes between the delocalisation eigenvectors and the molecule fixed axes of Figure 6.3 are shown in Figure 6.9. The plots are qualitatively the same as those for light water, indicating that delocalisation is occurring in a similar fashion as in the light water case, with the largest eigenvalue λ_3 corresponding to twisting/flapping.

6.6 Theoretical considerations

It shall be the aim of this section to persue a theoretical justification of the magnitude and the spread in the radius of gyration from harmonic oscillator theory.

Recall from Chapter 5 that the theoretical radius of gyration for the harmonic oscillator may be expressed as:

$$\Delta^2 = \frac{1}{\beta m \omega_0^2} \left[\frac{1}{2} \beta \hbar \omega_0 \coth \left(\frac{1}{2} \beta \hbar \omega_0 \right) - 1 \right]. \tag{6.1}$$

or, expressing Δ^2 in terms of the characteristic spring constant, C we may write

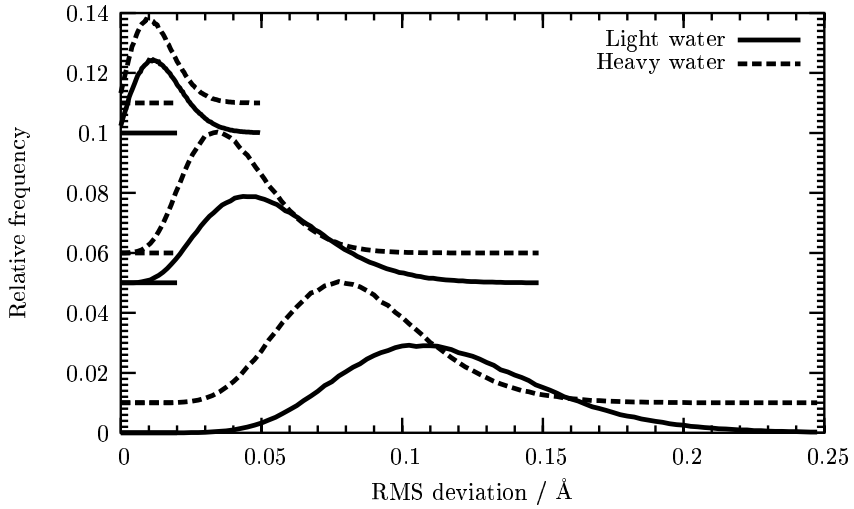

(a) Hydrogen/Deuterium.

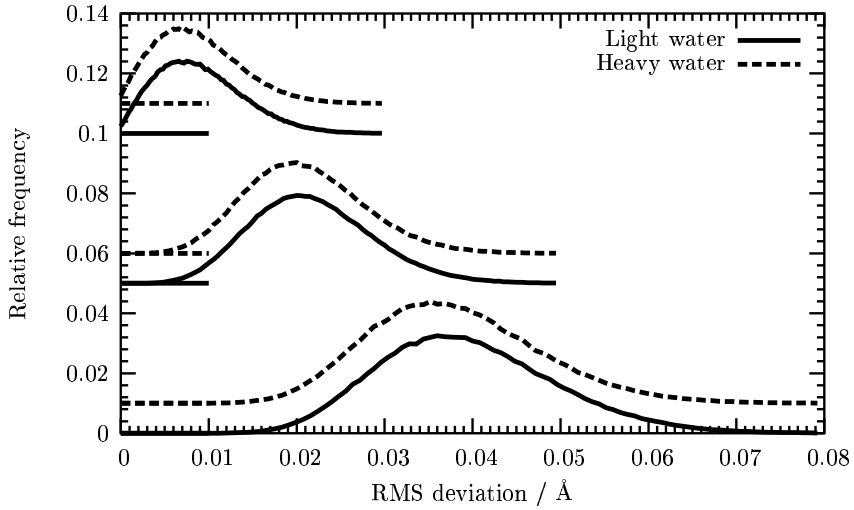

(b) Oxygen.

Figure 6.8: Comparison of the RMS delocalisation of atoms along their three principal axes for light and heavy water at their respective density maxima: $\rho = 1.0\,\mathrm{g\,cm^{-3}}$, $T = 277\,\mathrm{K}$ for light water, and $\rho = 1.1\,\mathrm{g\,cm^{-3}}$, $T = 284\,\mathrm{K}$ for heavy water.

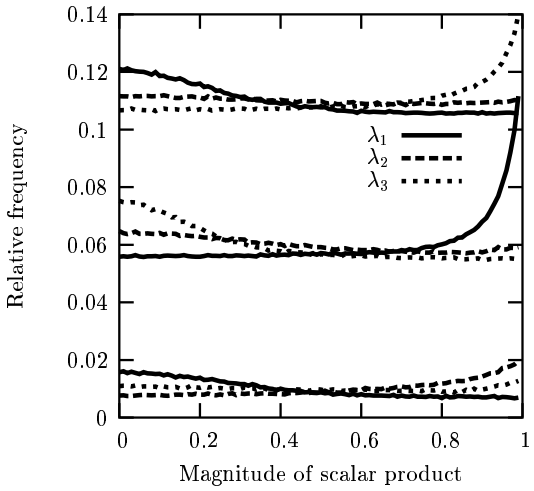

(a) Deuterium.

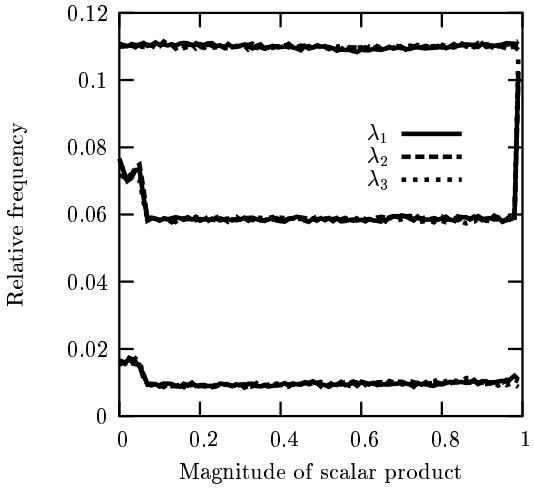

(b) Oxygen.

Figure 6.9: Distributions obtained when each of the three eigenvectors of the RGY tensor for heavy water are projected onto axes constructed using the molecular geometry, as illustrated in Figure 6.3. The λ_i denote the eigenvalues corresponding to the eigenvectors, with λ_1 being the lowest in magnitude and λ_3 the largest. Relative frequencies corresponding to each axis have been separated by 0.05 for clarity. Top to bottom: $\boldsymbol{x}$, $\boldsymbol{y}$ and $\boldsymbol{z}$ axes. The density was $\rho = 1.1\,\mathrm{g\,cm^{-3}}$ and the heavy water was thermostatted to $T = 284\,\mathrm{K}$.

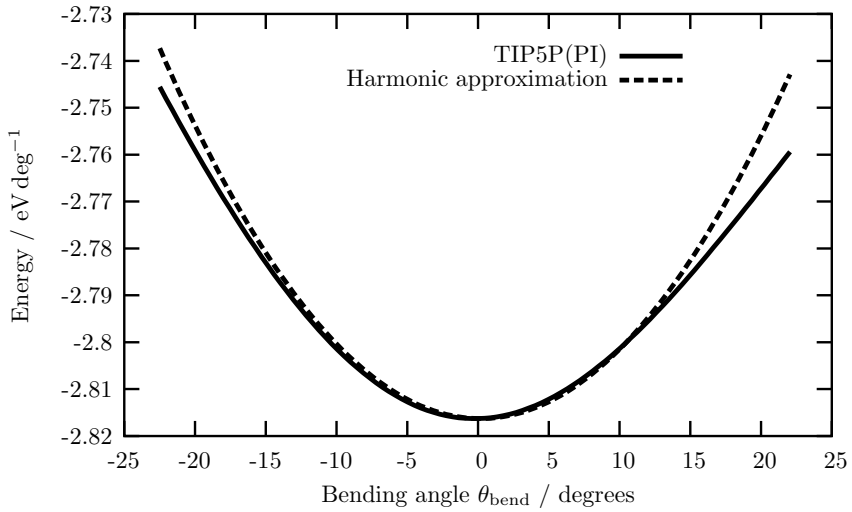

Figure 6.10: Potential energy against bond bending angle in the TIP5P(PI) water dimer, together with the correspondng harmonic approximation. R_{OO} = 2.8 Å.

Equation 6.1 as

$$\Delta^2 = \frac{k_{\mathrm{B}}T}{C}\left[\alpha\coth(\alpha) - 1\right] \tag{6.2}$$

with

$$\alpha = \frac{\beta\hbar}{2}\left(\frac{C}{m}\right)^{\frac{1}{2}} \tag{6.3}$$

Approximating the bond bending potential energy surface with a harmonic potential yields a theoretical value for α, and thus an approximate value for the radius of gyration in the dimer by theoretical means.

6.6.1 Evaluating the spring constant

The value of the spring constant used for the harmonic approximation is a function of the oxygen-oxygen separation R_{OO} and is plotted as such in Figure 6.11.

If we are to make comparisons between harmonic behaviour in the dimer and the RGY as measured by simulation, we need to obtain a suitably averaged value of the spring constant C. That is to say, we must take an average in which the most probable R_{OO} makes a larger contribution to the average, and vice versa. This may be achieved by using the RDF as a weighting function, as shown in Equation 6.4.

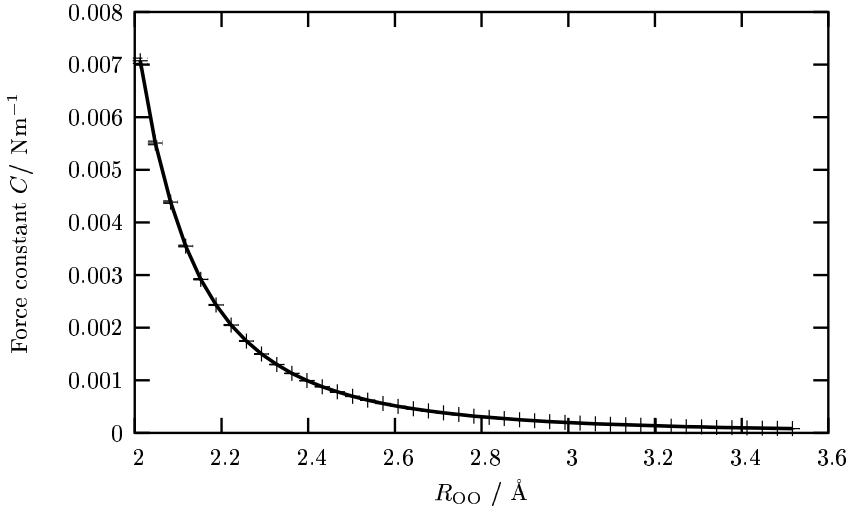

Figure 6.11: Harmonic spring constant as a function of the oxygen-oxygen separation R_{OO} in the TIP5P(PI) dimer. Error bars for each R_{OO} are shown, but are too small to resolve.

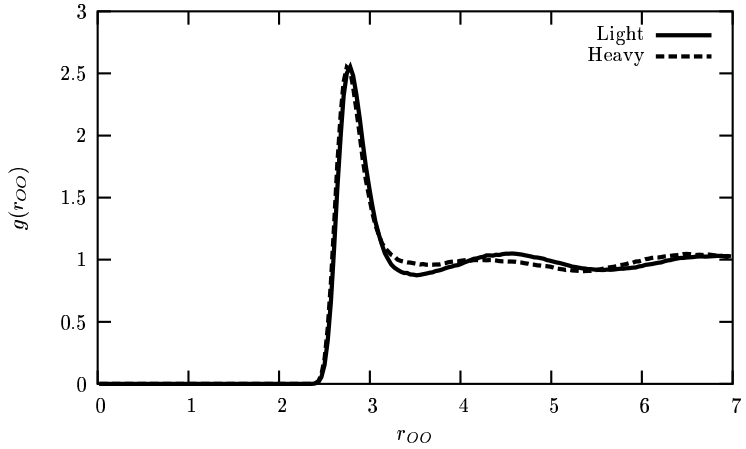

Figure 6.12: O-O radial distribution functions of light and heavy water at their density maxima.

$$\overline{C} = \frac{\int_0^{r_{\min}} C(r')\, g(r')\, (r')^2\, \mathrm{d}r'}{\int_0^{r_{\min}} g(r')\, (r')^2\, \mathrm{d}r'} \tag{6.4}$$

where $\overline{C}$ denotes the averaged spring constant. The radial distribution functions from the simulation of light and heavy water are shown in Figure 6.12.

We may further estimate the *uncertainty* on the spring constant induced by variations in R_{OO} through Equation 6.5; note that the uncertainty on the spring constant arising from the least squares fitting is neglible on the scale of this:

$$\varepsilon_C^2 = \frac{\int_0^{r_{\min}} C^2(r')\, g(r')\, (r')^2\, \mathrm{d}r'}{\int_0^{r_{\min}} g(r')\, (r')^2\, \mathrm{d}r'} - \overline{C}^2. \tag{6.5}$$

Water type	Spring constant / Nm^{-1}
Light*	12 ± 7
Heavy†	6 ± 6

* ρ = 1.0 g.cm^{-3} ; T = 277 K
† ρ = 1.1 g.cm^{-3} ; T = 284 K

Table 6.3: RDF weighted spring constants for light and heavy water.

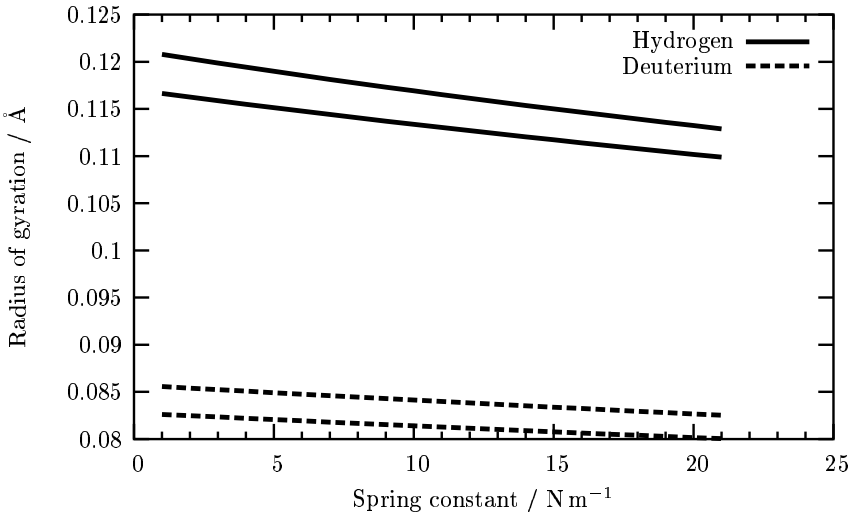

Figure 6.13: Theoretical radius of gyration Δ in one dimension as a function of the spring harmonic spring constant $\overline{C}$. Curves are plotted for temperatures of 273 K (top curves) and 293 K (bottom curves) for both hydrogen and deuterium in their respective waters.

$r_{\min}$ is the distance out to the first minimum in the RDF, which was taken to be 3.5 Å for both light and heavy water. Knowledge of the uncertainty in the spring constant affords a handle on the uncertainty on the radius of gyration — that is, the magnitude of the spread we might expect to see.

Evaluating the force constant at the values of R_{OO} for which $g_{\mathrm{OO}}(r)$ was known, and performing the weighted averaging procedure as expressed in Equations 6.4 and 6.5 we may obtain the desired values for the force constants, which are given in Table 6.3.

6.6.2 Theoretical RGY

Having evaluated the required spring constants, we may now move on to find the RGY from harmonic oscillator theory.

Figure 6.13 shows the theoretical radius of gyration in the finite temperature har-

Delocalisation type	Mass / amu	RGY magnitude / Å	Temperature uncertainty / Å	Spring constant uncertainty / Å
Light water				
Translation	18.0	0.0285*	0.0003*	—
Rocking	1.01	0.115	0.005	0.007
Twisting	1.01	0.115	0.005	0.007
Flapping	1.01	0.115	0.005	0.007
Heavy water				
Translation	20.0	0.0270*	0.0002*	—
Rocking	2.01	0.084	0.005	0.006
Twisting	2.01	0.084	0.005	0.006
Flapping	2.01	0.084	0.005	0.006

* Calculated using free particle theory.

Table 6.4: Theoretical radii of gyration in the harmonic approximation.

monic oscillator plotted as a function of the characteristic spring constant. The RGY shows a difference of but a few percent over the 20 K range between the two temperature curves for each isotope. There is a similarly small variation in the RGY over the shown range of spring constants. This allows us to understand the invariance of the RGY with temperature and density; in the higher density water, the spring constant may be modified due to a different RDF in the weighting procedure, yet the RGY shows little variation with the spring constant and as such is relatively unchanged.

Table 6.4 gives the calculated radii of gyration for each of the types of molecular delocalisation — translation, rocking, twisting and flapping — in both light and heavy water. The values for rocking, twisting and flapping are identical owing to a cylindrically symmetric potential with respect to bond bending in the harmonic approximation. The values for translation were calculated using free particle theory $\left(\overline{C} = 0\right)$ since this component of translation is only weakly connected to bond bending — a point which we shall discuss further in Subsection 6.6.3.

It is interesting to note that the radius of gyration in the harmonic calculations for λ_3 in light and heavy water is not at all significantly different to values found by free particle theory. Using protonic masses, the radius of gyration in any single dimension is given in Table 6.4 as 0.115 Å, and yet the equivalent value using free particle theory works out as 0.120 Å; again, the external potential modifies the radius of gyration by just 4%. The radius of gyration, then, is insensitive to the harmonic spring constant in the water system.

Though λ_3 matches simulation, λ_1 and λ_2 do not. It should be noted that there is

Delocalisation type	Effective mass / amu	RGY magnitude / Å	Temperature uncertainty / Å	Spring constant uncertainty / Å
Light water				
Translation	18.0	0.0285*	0.0003*	—
Rocking	2.04	0.083	0.005	0.005
Twisting	2.02	0.083	0.005	0.005
Flapping	2.09	0.082	0.006	0.005
Heavy water				
Translation	20.0	0.0270*	0.0002*	—
Rocking	4.06	0.060	0.006	0.004
Twisting	4.03	0.060	0.006	0.004
Flapping	4.10	0.059	0.006	0.004

* Calculated using free particle theory.

Table 6.5: Theoretical radii of gyration in the harmonic approximation using modified effective masses in place of proton masses; the new masses are such that a single proton generates the same moment of inertia as that on the complete molecule.

some overlap in the distibutions: the peaks are not distinctly resolved. Eigenvalues were sorted into increasing magnitudes, and their contributions to the respective distributions were made. It is possible that there has been some fluctuation in the eigenvalue sorting process when the distributions were formed. Further, molecular constraints may have affected radii of gyration — a point which we shall pick up on now.

6.6.3 Constraint effects

The TIP5P molecule has rigid molecule constraints which may be expected to have an impact upon the nuclear quantum properties, since the molecule is effectively delocalised as a whole. Two possible effects are discussed here.

Effective masses

Constraints in the TIP5P molecule serve to increase the moment of inertia of the molecule and hence the effective mass of the particle taking part in the hydrogen bonding.

The radii of gyration given in Table 6.4 were recalculated using modified masses; these mimic the effect of the other proton, and indeed the oxygen atom in the molecule, by generating the same moment of interia as if the other two atoms were present. The new RGY values are presented in Table 6.5.

Note now that the values for twisting and flapping are too small when compared with values from simulation. However, this may be understood if we think of uncertainty of the molecule about an axis perpendicular to the arm of the molecule which is forming the H-bond; now the other hydrogen atom lies very close to the axis of rotation, and does not contribute quite so much to the molecule moment of inertia about that axis. The effective masses for twisting and flapping as presented in Table 6.5 may then be thought of as a worst case scenario as regards the molecule constraint influence on the effective mass. The values for rocking and translation, however, remain too high in varying degrees.

6.6.4 The condensed phase

It should be remembered that a molecule in liquid water is part of a condensed phase system, and as such may be expected to show different characteristics of delocalisation.

The lesser value for translation delocalisation from simulation is likely to result from Lennard-Jones interactions; note that the RDF peak at 2.8 Å is less than the zero of Lennard-Jones force at 3.12 Å, and hence lies within the strongly repulsive region of the potential. This delocalisation, however, is small and hence unimportant, so we shall not persue it further.

A molecule may be H-bonded with up to four other molecules. We have already noted, however, the insensitivity of the radius of gyration to the harmonic spring constant. As such, at least in theory, the number of hydrogen bonds formed makes little difference the twisting, rocking and flapping delocalisations.

Twisting, rocking and flapping result in an uncertainty in the bond bending angle; a detailed study of path integral effects on hydrogen bonds in the liquid will be the subject of the next chapter.

6.7 Summary

Upon diagonalisation of the RGY tensor, hydrogenic quantum delocalisation was seen to occur with three characteristic magnitudes corresponding to three different directions when projected onto axes defined by the molecular geometry. The smallest degree of delocalisation corresponded to translation of the molecule as a whole, and the largest was connected with both twisting and flapping of the molecule.

While virtually unaffected by temperature and density over the range of values studied, the degree of delocalisation showed a 25% reduction in the magnitude of the largest eigenvalue upon isotopic substitution. It was possible to predict the scale of this reduction by applying harmonic oscillator theory to bond bending. This serves to suggest that the harmonic approximation remains valid in the condensed phase. While the magnitude of the largest eigenvalue agrees with theory, the *spread* in that value is, by theory, underestimated.

The invariance of the degree of delocalisation with temperature and density indicates that it cannot itself be responsible for the density maximum. However, the RGY of $\simeq 0.1$ Å is non-negligible; nuclear quantum effects provide a form of background delocalisation of the structure and must therefore be accounted for in the simulation of liquid water.

Chapter 7

Neighbours

7.1 Introduction

Chapter 6 revealed that when employing the path integral treatment, water molecules show a significant uncertainty in orientation. Since the hydrogen bond is directionally dependent, it is a logical step to suppose that quantum delocalisation has real implications for the degree of hydrogen bonding in the water system.

Recall from Chapter 2 that the density maximum is thought to be the result of an inward collapse of the second neighbour shell, leaving the first nearest neighbour shell comparatively unchanged. The present chapter will focus on characteristics of local structure as described in Section 3.11. Comparisons are drawn between quantum and classical simulation, but also structural changes under isotopic substitution.

Section 7.2 describes first nearest neighbour behaviour in classical and quantum water; the equivalent analysis of second neighbour characteristics is given in Section 7.3. Changes in neighbour distance upon isotopic substition are the subject Section 7.4, and Section 7.5 analyses first neighbour orientational characteristics. Section 7.6 draws the chapter to a close.

7.2 First NN distance

We start, then, with *first* nearest neighbour molecules, as determined via the method described in Section 3.11. Figures 7.1 and 7.2 show the relative frequency distribution of the bond bending angle θ_{bend} plotted against the first NN separation from classical and quantum simulation respectively.

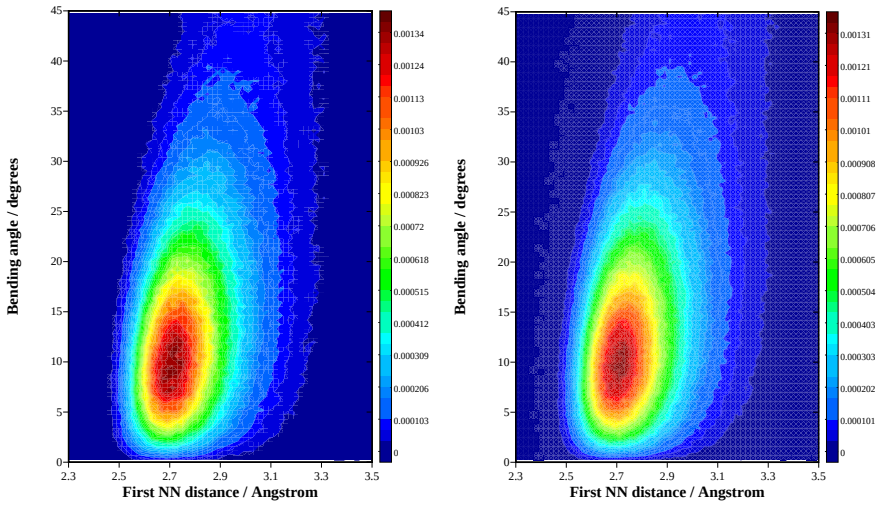

(a) T = 275 K (b) T = 277 K

(c) T = 279 K (d) T = 283 K

Figure 7.1: Relative frequency of bond bending angle θ_{bend} plotted against the first NN distances. The data represents water at $\rho = 1.0\,\mathrm{cm}^{-3}$ from *classical* simulation.

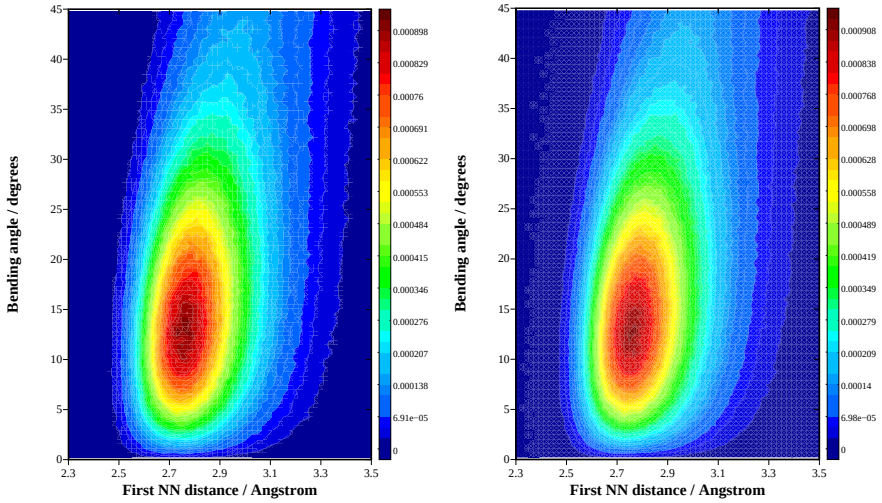

(a) T = 275 K (b) T = 277 K

(c) T = 279 K (d) T = 283 K

Figure 7.2: Relative frequency of bond bending angle θ_{bend} plotted against the first NN distances. The data represents water at $\rho = 1.0\,\mathrm{cm}^{-3}$ from *path integral* simulation.

On comparison of the two figures, it is apparent that the path integral treatment has two effects here. Firstly, the mode of the first NN (R_{OO}) distribution is shifted from $\simeq 2.7\,\text{Å}$ to $\simeq 2.8\,\text{Å}$, which has been seen previously from RDF observations (Mahoney and Jorgensen, 2001). However, here we see that the relaxation in H-bond length is accompanied by a shift in the bending angle distribution from $\simeq 10^\circ$ to $\simeq 12^\circ$. That is to say, each are shifted closer towards the experimental values presented in Table 2.9.

Note that these surfaces reflect something of the potential energy surface presented in Figure 4.8. The relative frequency gradient is much steeper close to the oxygen-oxygen repulsive core. Hydrogen bonds, then, show a preference to be bent rather than stretched, and further a preference to be *longer* rather than shorter.

We may also analyse the *quantum minus classical* difference surfaces, as presented in Figure 7.3; taking the difference surfaces in this way highlights the qualitative differences between the classical and the path integral treatment. A relaxation in the bond bending angle appears to be accompanied by a lengthening of the first NN distance. It is a matter of debate whether molecules forming the maxima remain hydrogen bonded. The cut-off employed by Martí *et al.* (1996) was $\theta_{\mathrm{bend}} = 30^\circ$, and here we see the maxima span this angle. In any case, it is clear that there exists a reduction of the number of the more linear hydrogen bonds with $\theta_{\mathrm{bend}} \lesssim 10^\circ$. An additional point is that the maximum in the distribution at $T = 277\,\text{K}$ is more broad than those seen at the other three temperatures, signalling a degree of bond weakening which is not present in the classical fluid. We shall return to this point in Section 7.3. It is interesting for now to take difference surfaces between two different temperatures. Such surfaces for both classical and quantum simulation are shown in Figure 7.4; note that the introduction of quantum effects generates similar structural changes to those observed upon an increase of temperature, a point made by Kuharski and Rossky (1985).

The surfaces of 7.1 and 7.2 allow us a handle on the degree of hydrogen bonding in the system. Integrating over the region for which R_{OO} is less than $3.6\,\text{Å}$ and θ_{bend} is less that a 30° cut-off angle yields an estimate for the instantaneous proportion of intact hydrogen bonds averaged over many configurations, as described in Chapter 3; such values are shown in Figure 7.5. Simulation shows that $\simeq$ 3–7% of hydrogen bonds are counted as broken, which is in good agreement with the the 5% degree of broken bonds quoted by Cho *et al.* (1997), though higher than the figure of 0.3% implied by Sciortino *et al.* (1990). Path integrals increase the proportion of broken bonds from $\simeq 3\%$ to $\simeq 7\%$. The instantaneous number of intact hydrogen bonds, then, remains very high. A point to note here is that the high proportion

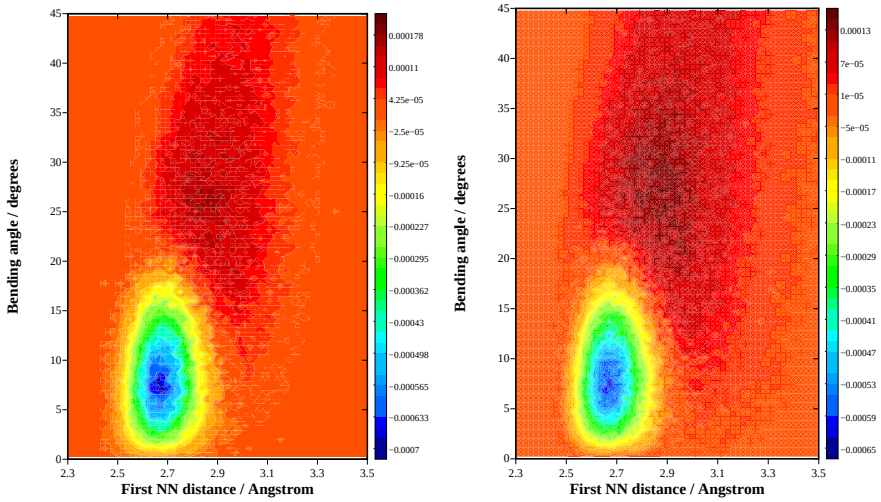

(a) T = 275 K (b) T = 277 K

(c) T = 279 K (d) T = 283 K

Figure 7.3: Surfaces formed by subtracting the classical from the quantum bond bending data presented in Figures 7.1 and 7.2. The data represents water at ρ = 1.0 cm^{-3}.

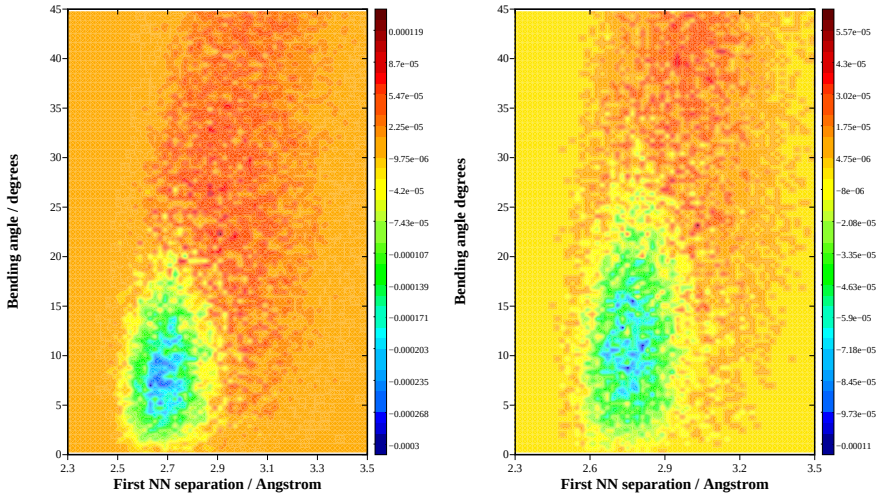

(a) Classical (b) Quantum

Figure 7.4: Difference surfaces for first NN molecules between simulation at T = 293 K and T = 275 K from both classical and quantum simulation.

affords a degree of justification for the techniques of local structure analysis employed here, since they were constructed on the assumption of an approximately tetrahedral system.

7.3 Second NN distance

Having analysed the first NN configuration, we now move on to look at the *second* nearest neighbours — *first nearest neighbours of the first nearest neighbours*. Before analysing *local* structure in more detail, we first take a glance at the RDFs for the classical and the quantum fluid shown in Figure 7.6. We note the broadening of the second neighbour peak, as seen in water simulations such as those of Mahoney and Jorgensen (2001), indicating a decay of the number of molecules at the tetrahedral second NN distance in the the quantum liquid as compared with classical simulation.

Figures 7.7 and 7.8 show relative frequency surfaces of bending angle against *second* NN distance in classical and path integral water respectively. Perhaps the most visible change under activation of path integrals is the already familiar shift in the mode with respect to the first NN bond bending angle θ_{bend}. The eye might further perceive a shift in the mode towards larger second NN separations.

The qualitative changes are highlighted when we take the *quantum minus classi-*

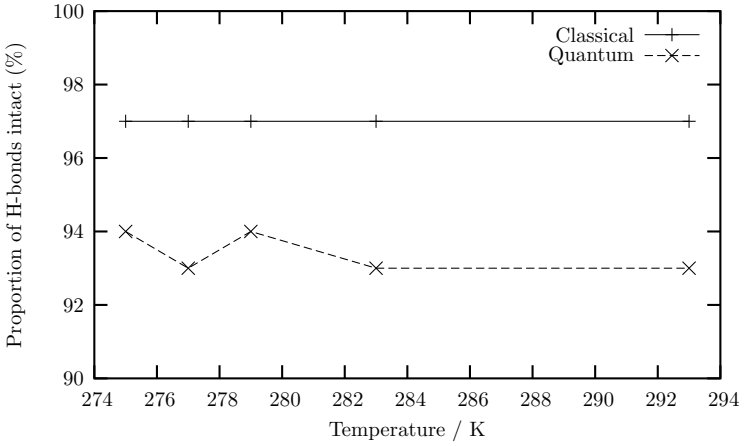

Figure 7.5: Instantaneous proportion of intact hydrogen bonds averaged over many configurations. The density was $\rho = 1.0\,\mathrm{g\,cm^{-1}}$.

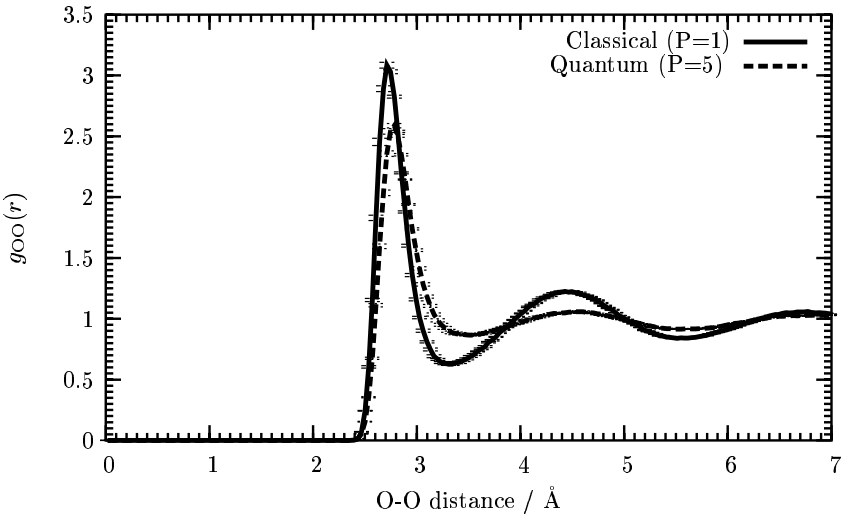

Figure 7.6: O-O radial distribution functions for classical and path integral water at $T = 277\,\mathrm{K}$.

cal difference surfaces, as presented in Figure 7.9. There we see something of the broadening of the second neighbour shell under application of path integrals; we find a larger number of molecules at both $\simeq 3.4\,\text{Å}$ and $\simeq 5.5\,\text{Å}$. In general, an increased or decreased second NN distance is attached to a less linear H-bond. We might therefore conclude that the displacement of second neighbours from the positions consistent with a tetrahedral lattice come about as a result of increased hydrogen bond bending, resulting in bond *weakening* and a corresponding breakdown in local structure.

It is interesting to analyse the RDFs in the region of 3.4 Å. The RDFs from classical and quantum simulation are shown in Figures 7.10 and 7.11. A careful inspection affords a hint at the value of the TMD for classical and quantum simulation. The RDF is inflated in the region of interest at $T = 277\,\text{K}$ in *quantum* simulation, with those for the two adjacent temperatures tracing curves which are systematically lower; thus hinting that the density maximum was correctly located at $T = 277\,\text{K}$. The same in not quite mirrored in the classical data. There we see two very similar curves at $T = 279\,\text{K}$ and $T = 289\,\text{K}$, suggesting that perhaps the TMD lies between these temperatures. However, note that the first minimum in the RDF for each occurs in different locations; looking at the expansions of the region of interest, the minimum occurs at approximately 3.3 Å and 3.5 Å in classical and quantum simulation respectively, for all temperatures studied. This serves to echo the point that the structural changes introduced by applying path integrals are far greater than those incurred by temperature changes in the range with which we are concerned here.

The above analysis gives us a hint at the microscopic reasoning behind the inflated TMD in *heavy* water. Recall from Section 7.2 that the influence of quantum effects were more marked at lower temperatures; the same is true in the *second* NN difference surfaces. We must not over-analyse here, since Figure 7.10 suggested that the density maximum was slightly shifted in the classical data. However, Figures 7.10 and 7.11 further show an inflated height at approximately 3.4 Å which is not present to as high an extent in either of the surrounding temperatures, serving to suggest that the broadened maximum in the difference surface at $T = 277\,\text{K}$ is generated by a quirk of the path integral rather than the classical data; indeed, the classical curve is undergoing significant modification in a single direction for temperatures spanning 277 K. The RDFs also show the first minimum for classical water beginning to assume a form more similar to that of the quantum counterpart in Figure 7.11(b) as temperature is increased. Nuclear quantum effects, then, may be inferred to aid the process of tetrahedral lattice breakdown; the lesser degree of

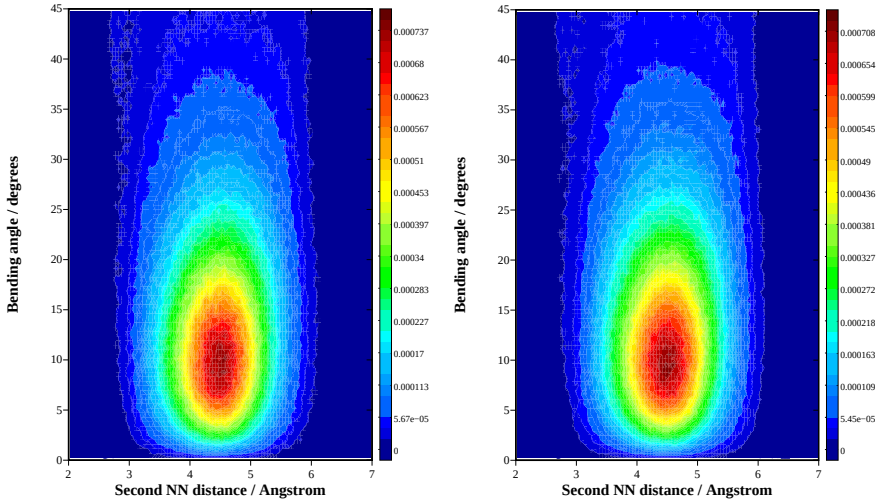

(a) T = 275 K (b) T = 277 K

(c) T = 279 K (d) T = 283 K

Figure 7.7: Relative frequency of the bond bending angle θ_{bend} plotted against second NN neighbour distances. The data represents water at $\rho = 1.0\,\mathrm{cm}^{-3}$ from *classical* simulation.

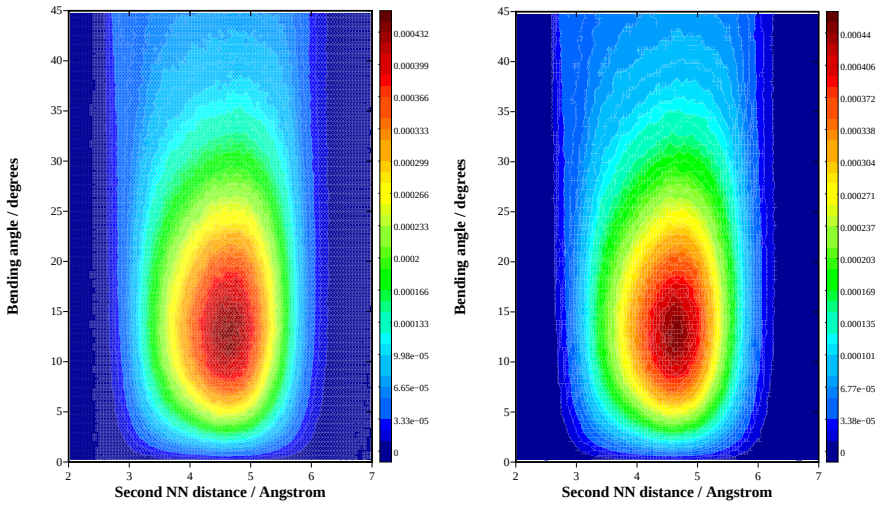

(a) T = 275 K

(b) T = 277 K

(c) T = 279 K

(d) T = 283 K

Figure 7.8: Relative frequency of the bond bending angle θ_{bend} plotted against second NN neighbour distances. The data represents water at $\rho = 1.0\,\mathrm{cm}^{-3}$ from *path integral* simulation.

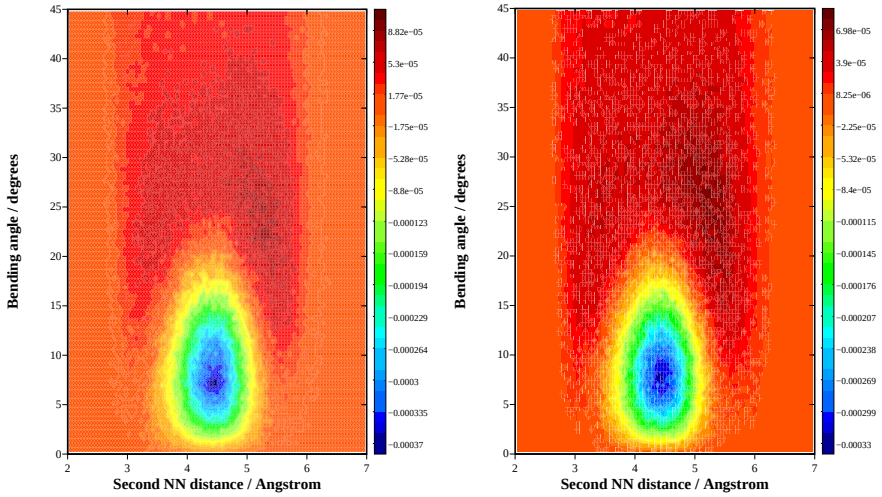

(a) T = 275 K (b) T = 277 K

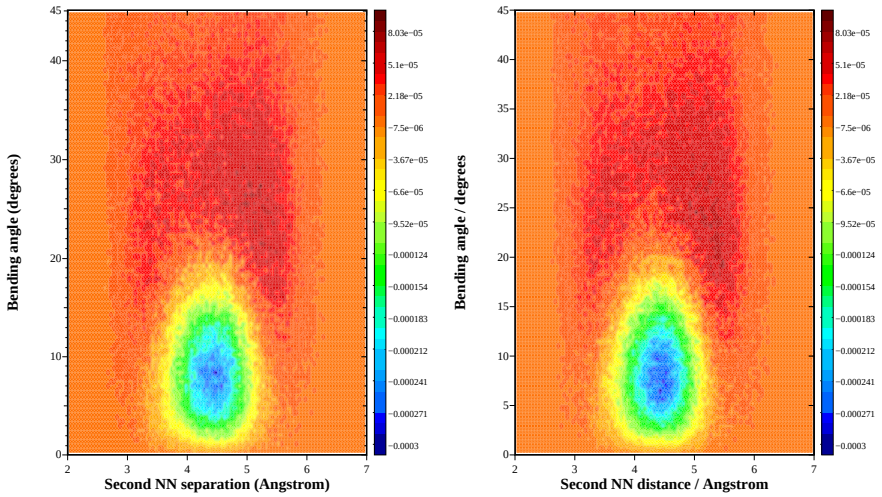

(c) T = 279 K (d) T = 283 K

Figure 7.9: Surfaces formed by subtracting the classical from the quantum bond bending data presented in Figures 7.7 and 7.8. The data represents water at ρ = 1.0 cm^{-3}.

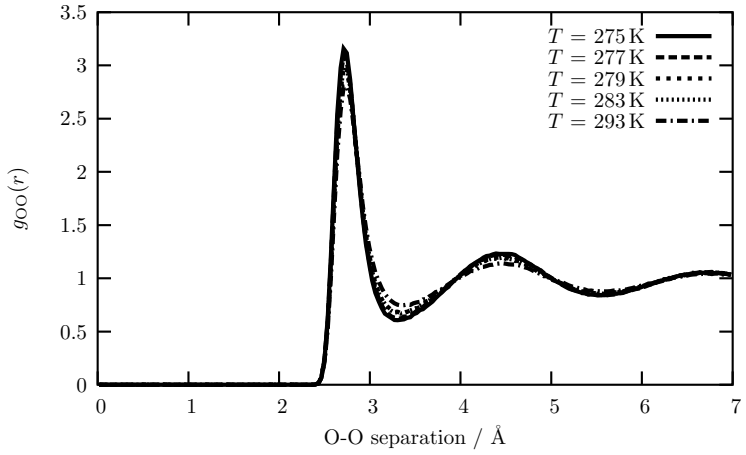

(a) Radial distribution functions.

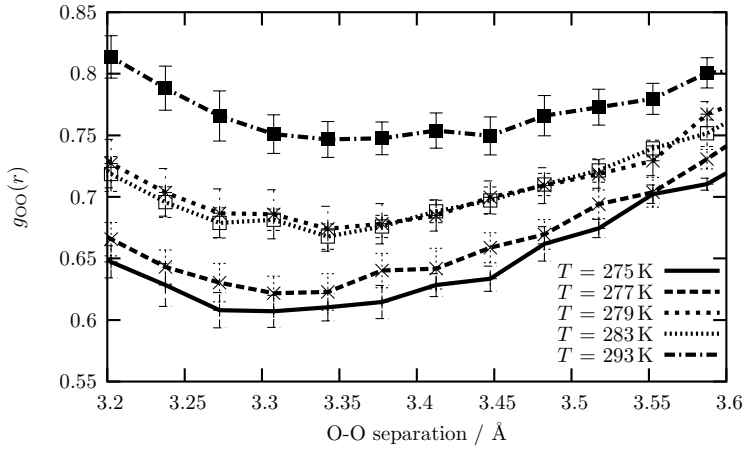

(b) Region of interest.

Figure 7.10: Radial distribution functions at $\rho = 1.0\,\mathrm{g\,cm^{-3}}$ density. The region of interest refers to the region $\simeq 3.4\,\text{Å}$. Calculated from *classical* simulation.

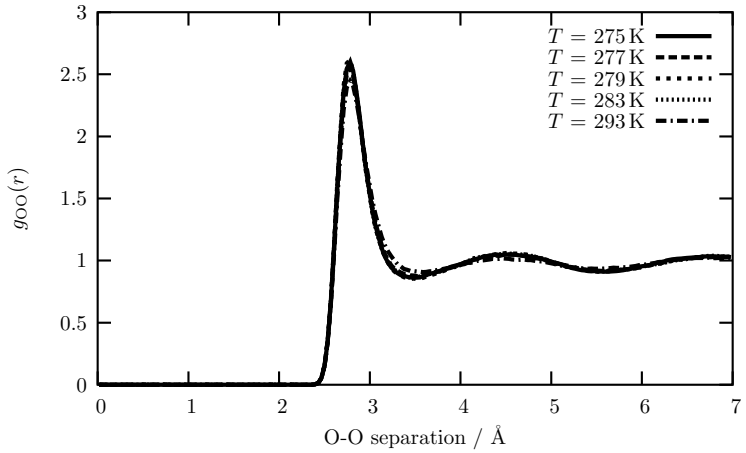

(a) Radial distribution functions.

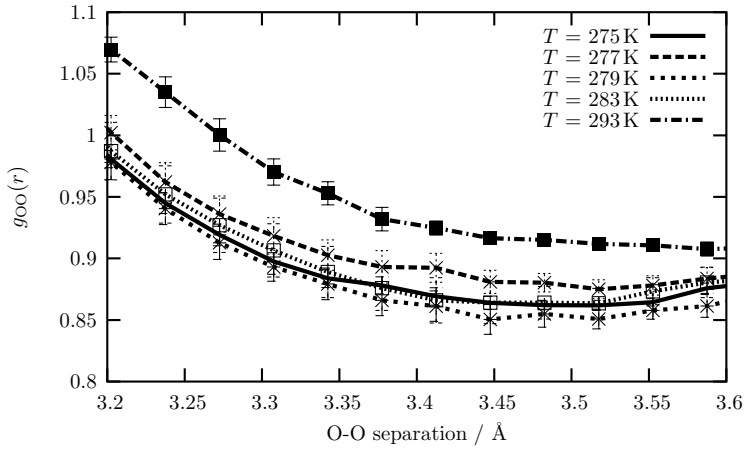

(b) Region of interest.

Figure 7.11: Radial distribution functions at $\rho = 1.0\,\mathrm{g\,cm^{-3}}$ density. The region of interest refers to the region $\simeq 3.4\,\text{Å}$. Calculated from *path integral* simulation.

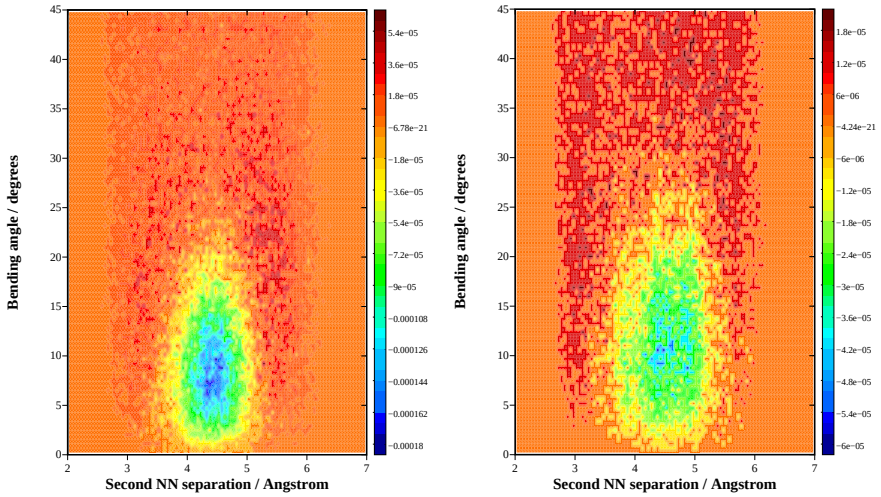

(a) Classical (b) Quantum

Figure 7.12: Difference surfaces for second NN molecules between simulation at T = 293 K and T = 275 K from both classical and quantum simulation.

quantum delocalisation in classical water means that a higher degree of thermal excitation is required to agitate molecules out of the lattice. A glance at Figure 7.12 indicates again that quantum fluctuations indeed generate similar structural changes as those due to thermal fluctuations. Note that as the liquid is heated, the differences between classical and quantum simulation become less well resolved. It is as if thermal fluctuations present in the classical simulation are giving chase to fluctuations present in the quantum liquid.

7.4 Heavy water

Recall from Chapter 2 that the density of heavy water is higher than that of light water, by approximately 10%. The radial distribution functions presented in Figure 7.13 indicate the effect of compression on the liquid structure is much more significant than that due to temperature. Density changes, together with nuclear quantum delocalisation, have major influences on the liquid structure. Since heavy water was simulated close to its experimental density maximum, we must keep in mind structural reorderings due to changes in *density* when comparing heavy with light water simulation at their respective density maxima.

Figure 7.13 shows the RDFs of light and heavy water at their density maxima, together with that for light water at T = 277 K, but with a 20% increase in density over the ordinary. Also shown in the curve from classical simulation of light water. First

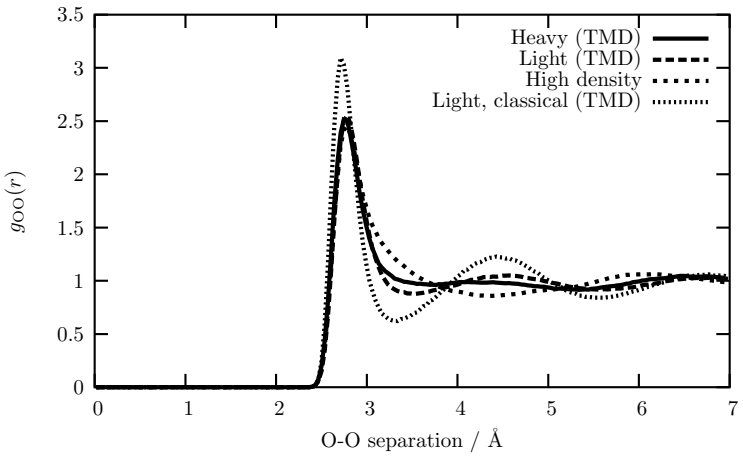

Figure 7.13: O-O RDFs for light and heavy water at their density maxima, and also for water at high density ($\rho = 1.2\,\mathrm{g\,cm^{-3}}, T = 277\,\mathrm{K}$).

note that the curve for heavy water does not lie between the quantum and classical data for light water, as seen in ST2 water by Kuharski and Rossky (1985); it should be emphasised, however, that there is a differential in density between the light and heavy water simulation here which was not present in the simulations of Kuharski and Rossky. It is interesting to note that the curve for high density water demonstrates an *outward* shift in the first minimum of the RDF. Further, the peak heights and trough depths retain the same approximate magnitude in high density water when compared with those at ordinary density. On the basis of density increase, it is therefore surprising that the lesser increase of 10% in density when moving to the study of heavy water should apparently subdue much of the liquid structure; the curve for heavy water is much more flat beyond the first NN peak than is the case for light water at ordinary or high density. Further, we have already noted that the effect of an increase in temperature on the RDF was not at all dramatic. The flatter curve, therefore, must result from a change in nuclear quantum delocalisation.

We may analyse the local structure of high density and heavy water by means of the first and second NN surfaces. Figure 7.14 shows the first NN surfaces for each, and the surfaces obtained when each has the quantum data corresponding to light water at the TMD subtracted away appear in Figure 7.16. While the compression of light water acts to promote hydrogen bond bending (and breaking), the heavy water difference surface shows a *reversal* of this behaviour. The reduced quantum effects of deuterium result in a stronger *deuterium* bond network than the equivalent in light water. Note that the mode of the first NN distribution remains at approximately 2.7 Å. As calculated in Chapter 2, the preferred tetrahedral second neighbour distance would therefore be 4.4 Å.

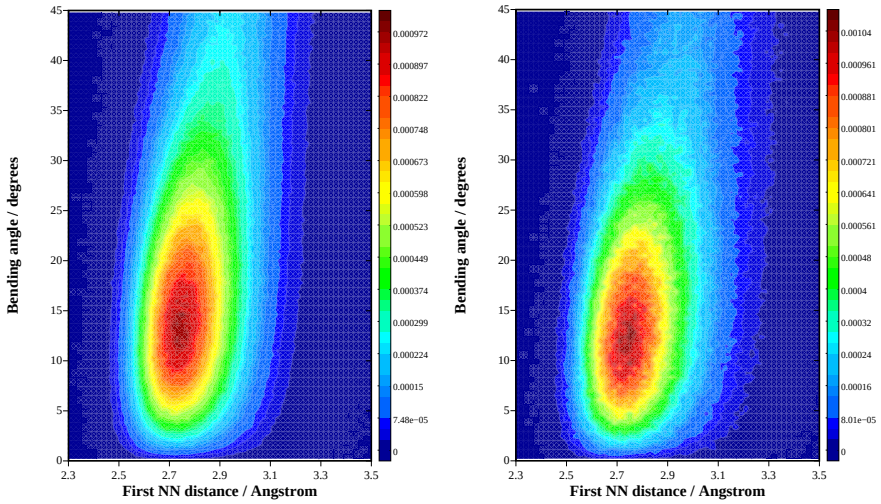

(a) High density water. (b) Heavy water.

Figure 7.14: Difference surfaces of both high density and heavy water with those for light water at the density maximum.

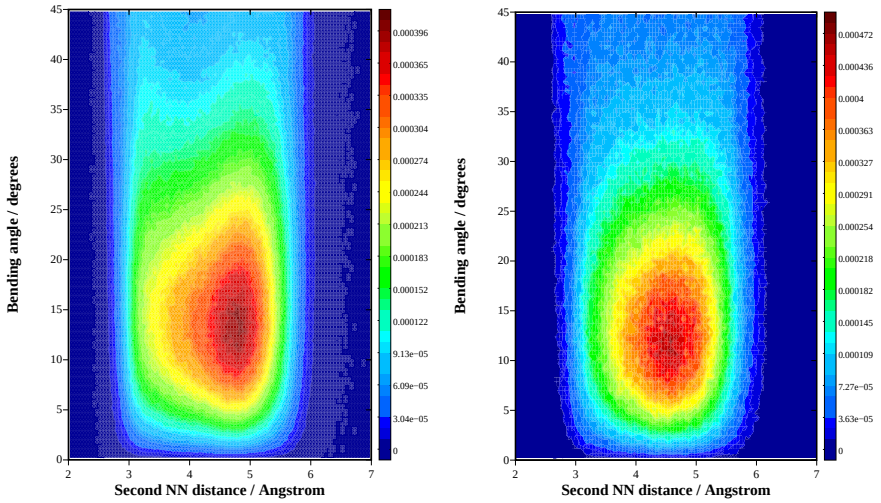

(a) High density water. (b) Heavy water.

Figure 7.15: Difference surfaces of both high density and heavy water with those for light water at the density maximum.

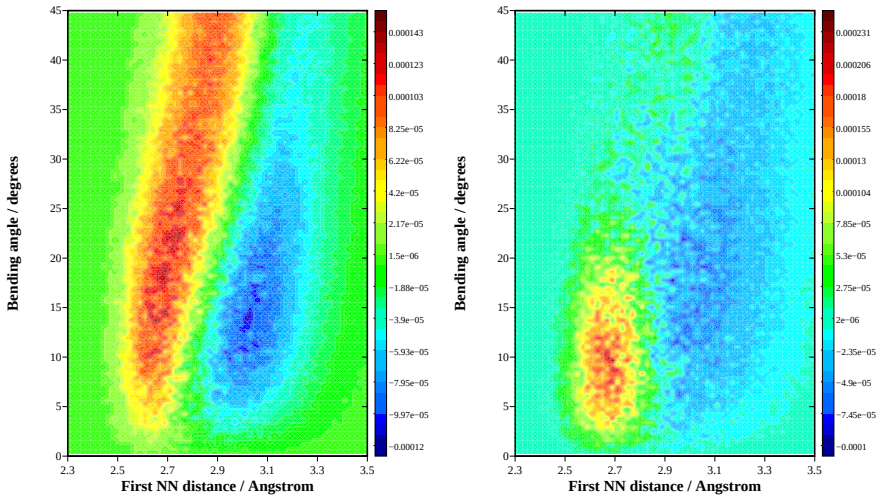

(a) High density water. (b) Heavy water.

Figure 7.16: Difference surfaces of both high density and heavy water with those for light water at the density maximum.

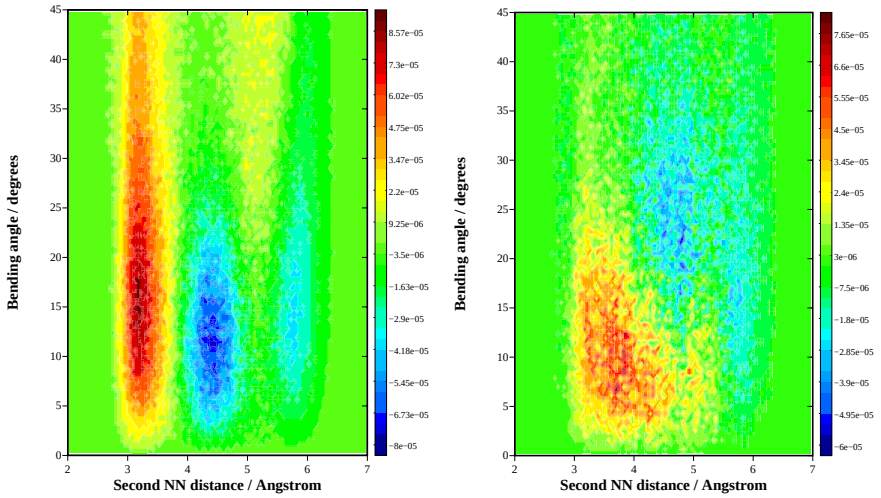

(a) High density water. (b) Heavy water.

Figure 7.17: Difference surfaces of both high density an heavy water with those for light water at the density maximum.

Moving on to look at characteristic *second* neighbours distances, as presented in Figure 7.15, we note that the high density light water demonstrates an *upward* shift in the mode. That is to say, second neighbour molecules tend to be *further away* from the central molecule in high density water. This surface, however, is very anisotropic. A comparatively gentle slope exists to the left of the mode; this is not easily seen in the equivalent surface for heavy water. The surfaces of Figure 7.15 differenced with those for light water at the density maximum are given in Figure 7.17. Now we see that plain compression acts to force molecules out of the tetrahedral configuration and into interstitial positions. While there is no evidence for any correlation between the second NN distance and first NN bond bending angles in moving from ordinary to high density water, the shift to *heavy* from light water divides Figure 7.17(b) in two along a *diagonal* axis. Second NN molecules at interstitial radial distances tend to surround *first* NN molecules which themselves form approximately linear H-bonds with the central molecule. That is, it would appear that the formation of molecular interstitials is aided by the presence of a surrounding tetrahedral order, perhaps by promoting the existence of cavities open to prospective interstitials.

This analysis may explain why the density of heavy water at its TMD is greater than that seen in light water. Recall from Chapter 2 that the density maximum is thought to mark the watershed between the formation of interstitial molecules in a surrounding tetrahedral configuration and familiar thermal expansion. We may perhaps think of the tetrahedral structure with interstitials present as a more closely packed and space efficient structure than that to which thermal expansion is attempting to drive the system. In heavy water, strong, approximately linear deuterium bonds persist to higher temperatures. They encourage the persistence of tetrahedral structure upon heating, and in doing so they maintain a higher number of cavities into which interstitials may fall. We may, therefore, picture the heavy water structure as being similar to light water, though more fully saturated with interstitial molecules.

Indeed, the results presented here would seem to blow uniformist and mixture models out of the water. The inward movement of second nearest neighbours is linked to *straighter* first NN hydrogen bonds, casting a shadow over uniformist models. Further, second NN molecules are correlated to regions of higher local tetrahedral order, thus discrediting mixture models. The phenomena seen here are very much consistent with an *interstitial* model.

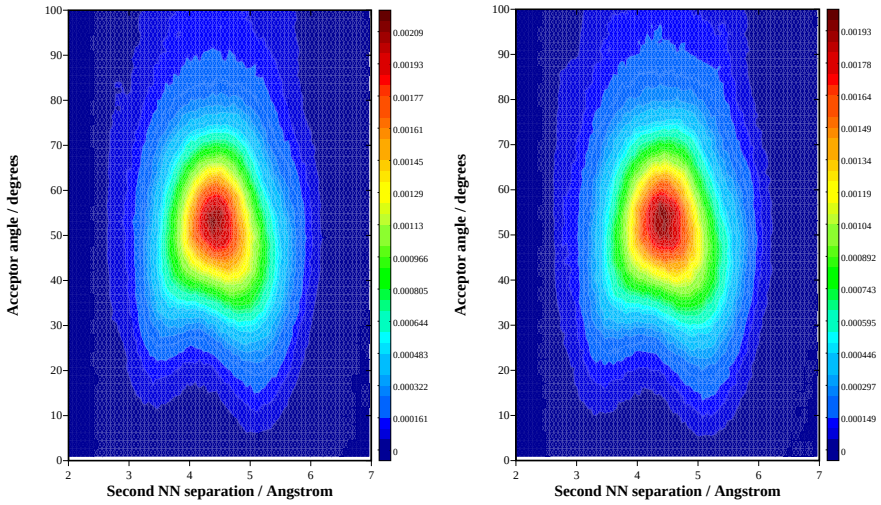

(a) T = 277 K (b) T = 283 K

Figure 7.18: Relative frequency distributions of acceptor angle against second NN separation from *classical* simulation. The density was $\rho = 1.0\,\mathrm{g\,cm^{-3}}$. Two surfaces are shown as a representative sample.

7.5 First NN orientation

As we saw in Chapter 4, Mahoney and Jorgensen (2000) made a point of demonstrating the double potential well in the water dimer with respect to the acceptor angle — the double well is shown in Figure 4.5. Such a double well acts to promote tetrahedral order.

Indeed, the orientational properties of the first nearest neighbours have the potential to influence the second neighbour shell, given the directionality of the hydrogen bond. In addition, Chapter 6 revealed that molecular delocalisation termed there as *flapping* commanded the greatest magnitude. We might therefore expect path integrals to have a significant impact on the first NN orientation and potentially the structural characteristics of the second neighbour shell. Such surfaces are shown in Figures 7.18 and 7.19. The *quantum minus classical* difference surfaces are presented in Figure 7.20.

We first see that the mode of the distributions occurs at $\simeq 55^\circ$, which is just half the angle between the lone pair sites of the TIP5P molecule. A preference is shown, then, for the lone pairs of the first NN acceptor molecule to point towards the central molecule even in the condensed phase.

There is an interesting feature which we shall mention in passing: an indentation at small acceptor angles is seen in the frequency distributions of Figures 7.18 and

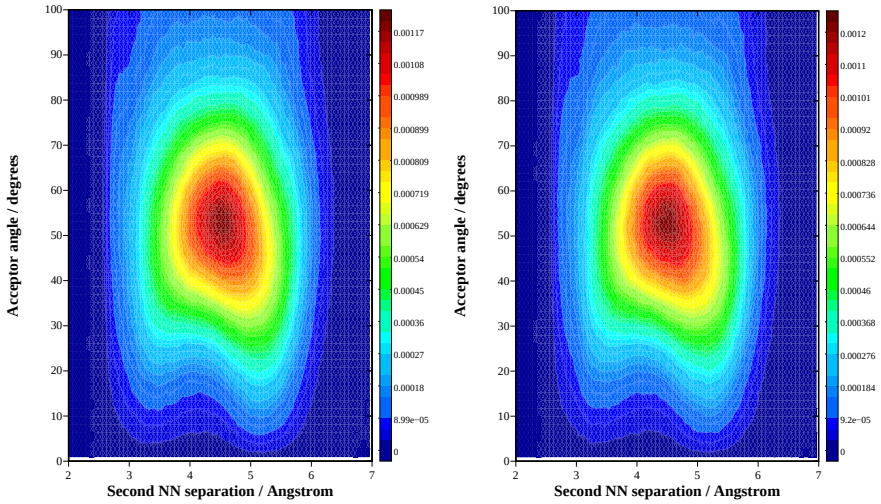

(a) T = 277 K (b) T = 283 K

Figure 7.19: Relative frequency distributions of acceptor angle against second NN separation from *path integral* simulation. The density was ρ = 1.0 g cm^{-3}. Two surfaces are shown as a representative sample.

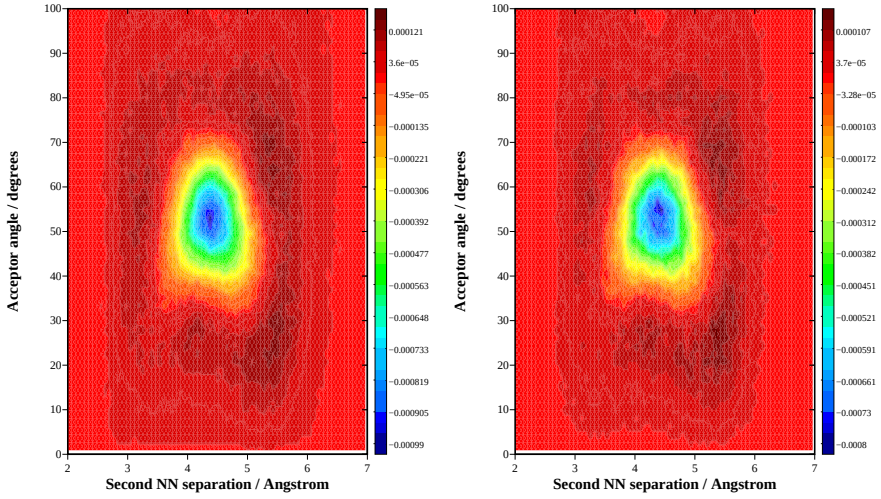

(a) T = 277 K (b) T = 283 K

Figure 7.20: Quantum minus classical difference surfaces formed from the data in Figures 7.18 and 7.19. Two surfaces are shown as a representative sample.

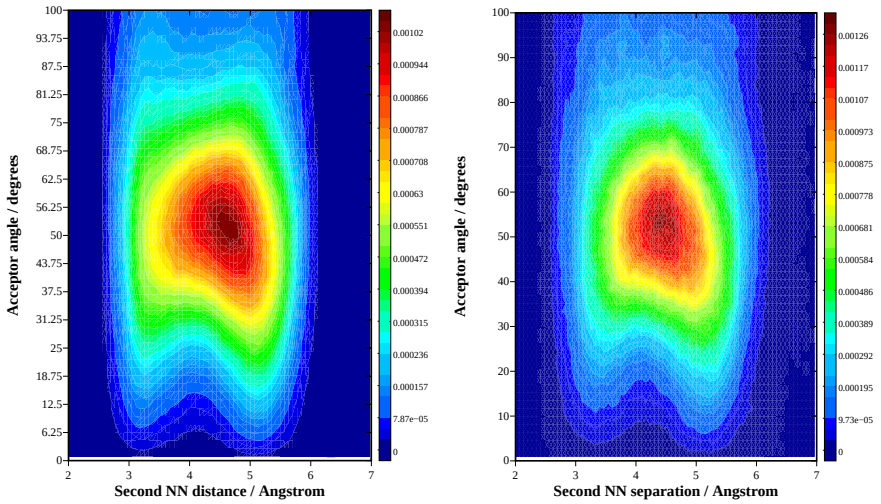

(a) High density water. (b) Heavy water.

Figure 7.21: Relative frequency distributions of acceptor angle against second NN distance for water at high density (ρ = 1.2 g cm^{-3}, T = 277 K) and also for heavy water at its experimental density maximum.

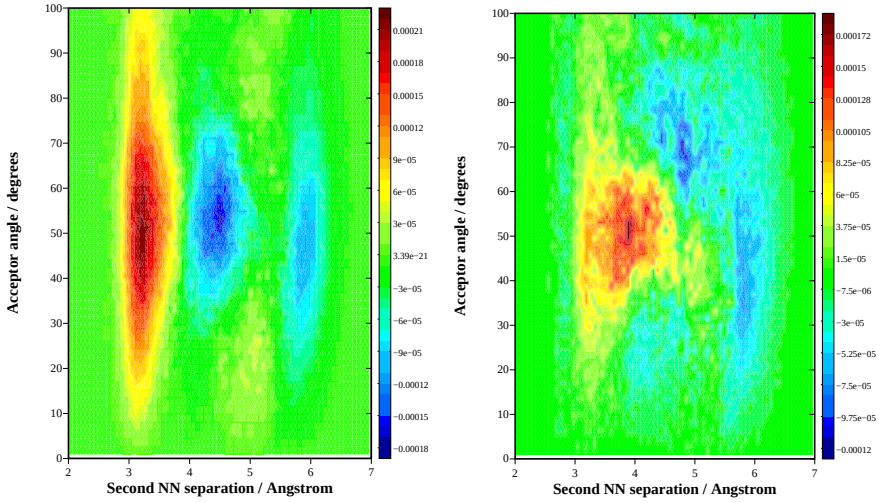

(a) High density water. (b) Heavy water.

Figure 7.22: Difference surfaces of both high density and heavy water with those for light water at the density maximum.

7.19; in other words, for low acceptor angles there emerge two preferred second NN distances. One such preferred distance occurs at $\simeq 3.4$ Å, and the other at $\simeq 5.3$ Å—precisely those values whose relative frequency increases upon activation of path integrals.

While it is difficult to resolve any systematic changes in the distribution upon activation of path integrals when compared with classical simulation, we may again compare the surfaces from high density and heavy water quantum simulation with those for path integral light water at the density maximum. Relative frequency distributions are shown in Figure 7.21, and difference surfaces are presented in Figure 7.22. Now we see further evidence of the increased tetrahedral structure in the heavy water system. Whereas compression acts to generate a peak with a less localised acceptor angle, the reverse is true when we make the transition to heavy water. Figure 7.22 suggests that interstitial second neighbour molecules tend to surround first nearest neighbour molecules which themselves have a particular acceptor angle of $\simeq 55^\circ$, which is consistent with a tetrahedral configuration. Again we see that in heavy water second NN interstitials are correlated to local tetrahedral structure.

7.6 Summary

In both classical and path integral simulation, the proportion of unbroken hydrogen bonds present was in the region of 95%, fuelling support for the notion of a high degree of tetrahedral order in the liquid.

Upon activation of the path integral treatment, the first NN peak was shifted out from $\simeq 2.7$ Å to $\simeq 2.8$ Å when compared with classical simulation; further, this occured with a corresponding shift in the mode of the bond bending distribution from $\simeq 10^\circ$ to $\simeq 12^\circ$. That is to say, each moved closer to the experimental values of Modig *et al.* (2003). The path integral description of TIP5P water, then, would seem to more accurately represent the microscopics of the real liquid over classical simulation.

Analysis of *second* NN behaviour revealed that the broadening in the second neighbour RDF peak due to nuclear quantum effects is accompanied by an increase in *first* NN bond bending angles. Nuclear quantum delocalisation may be seen to induce a greater number of molecules to appear at interstitial-like radial distances as a consequence of a breakdown in tetrahedral structure, with thermal effects in classical simulation perhaps beginning to match the structural changes added by the

path integral treatment with increasing temperature. The inflated TMD in heavy water may then be understood in terms of the lesser degree of quantum delocalisation present in the liquid; a greater degree of thermal excitation is required to break down the tetrahedral character of the liquid structure.

The consequences of switching to *heavy* water were analysed alongside those of light water compression. While the effect of a straight density increase was to break down the hydrogen bond network, the reverse effect was seen in heavy water: the reduced quantum effects of deuterium resulted in *stronger* hydrogen bond network, counteracting any effect which the density increase demanded. Moreover, a correlation was seen between the *second* NN distance and *first* NN bending angle when the heavy water surface was differenced with that from light water simulation; this point fits the interpretation in which persistent hydrogen bonds in the liquid maintain the presence of cavities which may be filled by molecular interstitials. Evidence of a stronger local structure did not just come about through the study of bond bending, but also from the analysis of acceptor angles, which showed a comparatively narrow peak in the relative frequency distribution at interstitial second NN separations and a tetrahedrally consistent angle when the surface for heavy water was differenced with that of light water. A space efficient nature of the tetrahedral lattice with interstitials would also serve to explain the greater density seen in heavy water at its density maximum over light water: a greater saturation of the tetrahedral-like lattice may be achieved before thermal expansion begins to take hold.

So, then, while light water exhibits a density maximum at a lower temperature, the maximum of density which it reaches is not as great as in the case of *heavy* water, for there the increased thermal fluctuations are perhaps able to form interstitials within a tetrahedral which has not decayed so rapidly under the effect of nuclear quantum delocalisation.

Chapter 8

Conclusion

The quantum delocalisation of atoms in constrained water molecules has been analysed in liquid water close to the density maximum, and indicated an ellipsoidal form with three characteristic magnitudes of delocalisation along three principal axes.

The direction relative to the water molecule which commanded the largest degree of delocalisation was that normal to the plane of the molecule, and hence perpendicular to all constrained intramolecular distances. Here the radius of gyration was seen to be described very well by harmonic oscillator theory in both light and heavy water, and further was very close to the free particle value — a point which perhaps serves to indicate that the degree of hydrogen bond bending is always sufficiently small to maintain the validity of the harmonic approximation.

A more rigorous analysis of hydrogen bond bending revealed that $\simeq 95\%$ of hydrogen bonds in the system were unbroken at any instant. Further, the familiar outward shifting of the first peak in the oxygen-oxygen RDF under the path integral treatment of nuclei was seen to be accompanied by a relaxation in the hydrogen bond bending angle; both the first RDF peak and the average bond bending angle were shifted closer to their experimental values.

The influence of nuclear quantum effects on the *second* nearest neighbour characteristics was to displace molecules from the tetrahedral position of 4.5 Å, with an accompanying weakening of hydrogen bonding manifested through an increase in bending angles. The effect of temperture changes on the water structure was miniscule: much smaller than changes caused by the activation of path integrals.

Heavy water structure under quantum simulation was compared with that of light water. The key findings are summarised by Figure 8.1. Isotopic substitution does not only encourage a stronger intermolecular bonding network; increased numbers

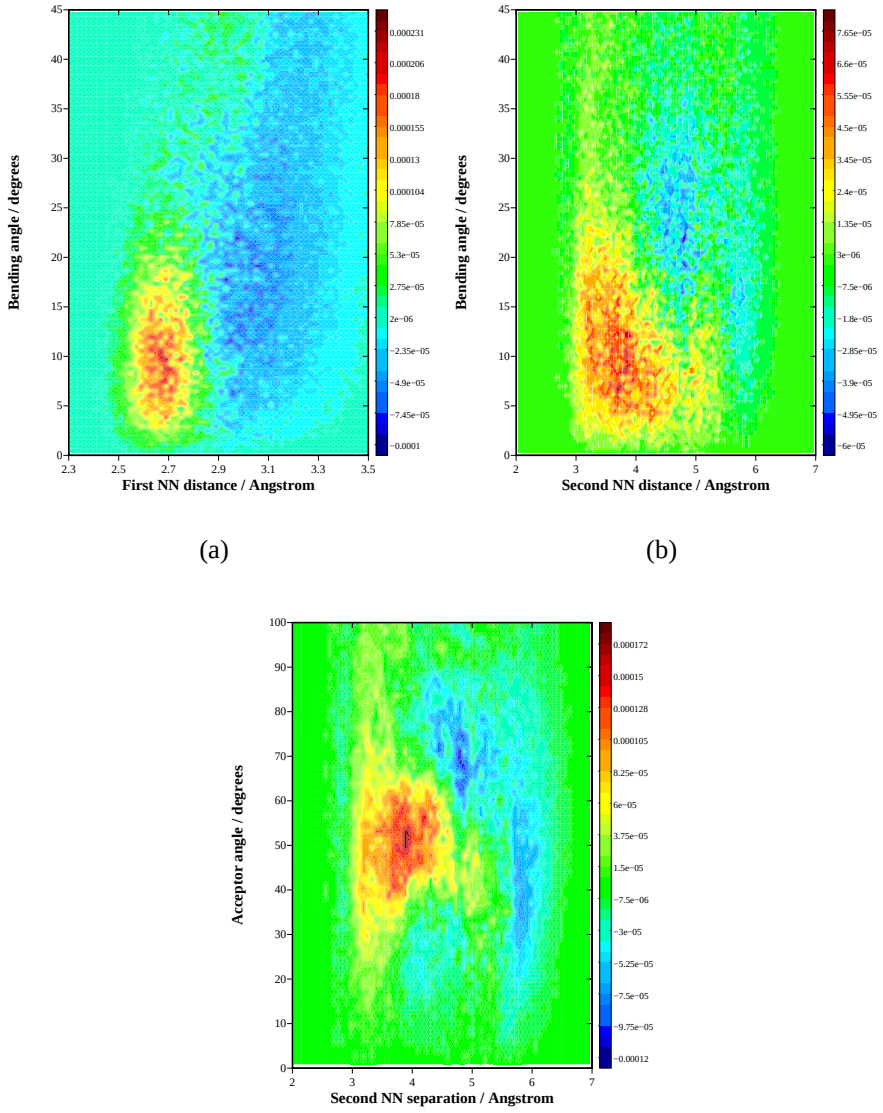

(a) (b)

(c)

Figure 8.1: *Heavy minus light water* difference surfaces as presented in Chapter 7. The systems were simulated at their respective density maxima.

of second neighbour molecules at interstitial-like radial distances may be seen to be correlated with regions of stronger local tetrahedral order.

The simulations presented here, then, support the notion that the anomalous density behaviour is caused by a collapse of the second neighbour shell on heating to form molecular interstitials, with nuclear quantum effects assisting the process. However, the present work further suggests that an increased degree of local tetrahedral order in heavy water leaves scope for an increased level of saturation with interstitial molecules before thermal expansion takes control, thus explaining the increased maximum of density in heavy water.

Future work

While differences have been found between water with and without a quantum treatment of atomic nuclei, the data presented are ensemble averages. The path integral methodology employed in the present simulations does not strictly represent real time quantum dynamics. However, the presence of quantum tunnelling may be detected be searching for instances of unusually large stretching of the path integral loop corresponding to a quantum particle. It would, then, be of huge interest to compare the frequency of quantum tunnelling events in the heavy and light water systems.

It should be emphasised that *all* explicit treatment of quantum mechanical behaviour presented here related only to atomic *nuclei*; electronic behaviour was described by a crude system of interaction sites. There is a case, then, for an *ab initio* verification of the results presented in this thesis, particularly in light of the directional dependence and partial covalency of the hydrogen bond.

Appendices

Appendix A

Path Integral Formalism

A.1 Derivation

Here we shall follow the derivation of the path integral starting from Schrödinger's equation as given by Simons (2000).

The time evolution of a state vector is given by Schrödinger's equation:

$$\mathrm{i}\hbar\frac{\partial}{\partial t}\left|\Psi\right\rangle = \hat{H}\left|\Psi\right\rangle \tag{A.1}$$

We can integrate this to get the time evolution operator (for time independent Hamiltonians) such that

$$\left|\Psi(t')\right\rangle = \hat{U}(t',t)\left|\Psi(t)\right\rangle \tag{A.2}$$

$$\hat{U}(t',t) = \exp\left[-\frac{\mathrm{i}}{\hbar}\hat{H}(t'-t)\right] \tag{A.3}$$

Resolving the state vector on to a continuous set of eigenstates of position

$$\begin{aligned}\Psi(x',t') &= \left\langle x'\left|\Psi(t')\right.\right\rangle \\ &= \left\langle x'\left|\hat{U}(t',t)\right|\Psi(t)\right\rangle \\ &= \left\langle x'\right|\hat{U}(t',t)\int dx\left|x\right\rangle\left\langle x\right|\Psi(t)\right\rangle \\ &= \int \mathrm{d}x\left\langle x'\left|\hat{U}(t',t)\right|x\right\rangle\left\langle x\right|\Psi(t)\right\rangle\end{aligned} \tag{A.4}$$

so that

$$\Psi(x',t') = \int \mathrm{d}x\, \hat{u}(x',t';x,t)\Psi(x,t) \tag{A.5}$$

with

$$\hat{u}(x',t';x,t) = \left\langle x' \left| \hat{U}(t',t) \right| x \right\rangle \tag{A.6}$$

Now divide the time evolution into a number of smaller evolutions in time

$$\hat{U}(t',t) = \hat{U}(t',t_{N-1})\hat{U}(t_{N-1},t_{N-2})\cdots\hat{U}(t_2,t_1)\hat{U}(t_1,t) \tag{A.7}$$

$$\begin{aligned}\hat{u}(x',t';x,t) = \int \mathrm{d}x_{N-1} \int \mathrm{d}x_{N-2} ..... \int \mathrm{d}x_1 \left\langle x' \left| \hat{U}(t',t_{N-1}) \right| x_{N-1} \right\rangle \\ \left\langle x_{N-1} \left| \hat{U}(t_{N-1},t_{N-2}) \right| x_{N-2} \right\rangle \cdots \left\langle x_1 \left| \hat{U}(t_1,t) \right| x \right\rangle\end{aligned} \tag{A.8}$$

Note that the end points x_0 and x_N are not integrated over, because they correspond to two fixed end points.

For a single term we have[1]

$$\begin{aligned}&\left\langle x_{k+1} \left| \hat{U}(t_{k+1},t_k) \right| x_k \right\rangle \\ &\quad\equiv \left\langle x_{k+1} \left| \exp\left[-\frac{\mathrm{i}}{\hbar}\Delta t \hat{H}\right] \right| x_k \right\rangle \\ &\quad= \int \mathrm{d}p_k \, \langle x_{k+1} \mid p_k \rangle \left\langle p_k \left| \exp\left[-\frac{\mathrm{i}}{\hbar}\Delta t \hat{H}\right] \right| x_k \right\rangle \\ &\quad= \int \mathrm{d}p_k \, \langle x_{k+1} \mid p_k \rangle \exp\left[-\frac{\mathrm{i}}{\hbar}\Delta t\, H(p_k,x_k)\right] \langle p_k \mid x_k \rangle \\ &\quad= \int \frac{\mathrm{d}p_k}{2\pi\hbar} \exp\left[\frac{\mathrm{i}}{\hbar}p_k x_{k+1}\right] \exp\left[-\frac{\mathrm{i}}{\hbar}\Delta t\, H(p_k,x_k)\right] \exp\left[-\frac{\mathrm{i}}{\hbar}p_k x_k\right]\end{aligned} \tag{A.9}$$

We then make the *primitive approximation*

[1] Two factors of $\frac{1}{\sqrt{2\pi\hbar}}$ arise from normalisation: we demand $\langle p' \mid p \rangle = \delta(p'-p) = \frac{1}{2\pi}\int_{-\infty}^{+\infty} \mathrm{d}\left(\frac{p}{\hbar}\right) \exp\left[\mathrm{i}\frac{p}{\hbar}(p'-p)\right]$

$$x_{k+1} \simeq x_k + \dot{x}_k \Delta t \tag{A.10}$$

The propagator over a small time step now becomes

$$\begin{aligned}
&\left\langle x_{k+1} \left| \hat{U}(t_{k+1}, t_k) \right| x_k \right\rangle \\
&\quad = \int \frac{\mathrm{d}p_k}{2\pi\hbar} \exp\left[\frac{\mathrm{i}}{\hbar}\Delta t\, p_k \dot{x}_k\right] \exp\left[-\frac{\mathrm{i}}{\hbar}\Delta t\, H(p_k, x_k)\right] \\
&\quad = \int \frac{\mathrm{d}p_k}{2\pi\hbar} \exp\left[\frac{\mathrm{i}}{\hbar}\Delta t\ (p_k \dot{x}_k - H(p_k, x_k))\right]
\end{aligned} \tag{A.11}$$

Now, the kinetic part of the Hamiltonian is $-\frac{p^2}{2m}$

$$p\dot{x} - \frac{p^2}{2m} = -\frac{1}{2m}(p - m\dot{x})^2 + \frac{m}{2}\dot{x}^2 \tag{A.12}$$

Using this in Equation we find[2]

$$\begin{aligned}
&\int \frac{\mathrm{d}p_k}{2\pi\hbar} \exp\left[\frac{\mathrm{i}}{\hbar}\Delta t \left(p_k \dot{x}_k - \frac{p_k^2}{2m}\right)\right] \\
&\quad = \int \frac{\mathrm{d}p_k}{2\pi\hbar} \exp\left[\frac{\mathrm{i}}{\hbar}\Delta t \left(-\frac{1}{2m}(p_k - m\dot{x}_k)^2 + \frac{m}{2}\dot{x}_k^2\right)\right] \\
&\quad = \int \frac{\mathrm{d}p_k}{2\pi\hbar} \exp\left[-\frac{\mathrm{i}}{\hbar}\Delta t \frac{1}{2m}(p_k - m\dot{x}_k)^2\right] \exp\left[\frac{\mathrm{i}}{\hbar}\Delta t \frac{m}{2}\dot{x}_k^2\right] \\
&\quad = \frac{1}{2\pi\hbar}\left(\frac{2\pi m\hbar}{\mathrm{i}\Delta t}\right)^{\frac{1}{2}} \exp\left[\frac{\mathrm{i}}{\hbar}\Delta t \left(\frac{m}{2}\dot{x}_k^2\right)\right]
\end{aligned} \tag{A.13}$$

$$\begin{aligned}
\hat{U}(x', t'; x, t) &= \int \frac{\mathrm{d}p_{N-1}}{2\pi\hbar} \int \frac{\mathrm{d}p_{N-2}}{2\pi\hbar} \cdots \int \frac{\mathrm{d}p_0}{2\pi\hbar} \int \mathrm{d}x_{N-1} ..... \int \mathrm{d}x_1 \\
&\qquad \exp\left[\frac{\mathrm{i}}{\hbar}\Delta t \sum_{k=0}^{N-1} (p_k \dot{x}_k - H(p_k, x_k))\right] \\
&= \left(\frac{m}{2\pi \mathrm{i}\hbar\Delta t}\right)^{\frac{N}{2}} \int \mathrm{D}x_{k\neq 0, k\neq N} \exp\left[\frac{\mathrm{i}}{\hbar}\Delta t \sum_{k=0}^{N-1} \left(\frac{m}{2}\dot{x}^2 - V(x)\right)\right]
\end{aligned} \tag{A.14}$$

[2] We use the fact that the area under a Gaussian curve is the same, to wherever its maximum is translated. $\int_{-\infty}^{+\infty} \mathrm{e}^{-ax^2} \mathrm{d}x = \sqrt{\frac{\pi}{a}}$

where we have used the notation

$$\mathrm{D}x \equiv \mathrm{d}x_{N-1}\mathrm{d}x_{N-2}\ldots\mathrm{d}x_1. \tag{A.15}$$

Now let the number of timesteps tend to infinity to obtain[3]

$$\hat{u}(x',t';x,t) = \lim_{N\to\infty\,\Delta t\to 0}\left(\frac{m}{2\pi\mathrm{i}\hbar\Delta t}\right)^{\frac{N}{2}}\int_{x(t)=x}^{x(t')=x'}\mathrm{D}x(t'') \exp\left[\frac{\mathrm{i}}{\hbar}\int_t^{t'}\mathrm{d}t''\left(\frac{m}{2}\dot{x}^2 - V(x)\right)\right] \tag{A.16}$$

Examine the integral in Equation A.16. It is just the integral of the Lagrangian over time - the *action* $S[x]$.

$$\hat{u}(x',t';x,t) = \int\overline{\mathrm{D}}x(t'')\exp\left[\frac{\mathrm{i}}{\hbar}S(x)\right] \tag{A.17}$$

$$\overline{\mathrm{D}}x \equiv \lim_{N\to\infty,\Delta t\to 0}\left(\frac{m}{2\pi\mathrm{i}\hbar\Delta t}\right)^{\frac{N}{2}}\mathrm{d}x_{N-1}\mathrm{d}x_{N-2}\ldots\mathrm{d}x_1 \tag{A.18}$$

Now that we have the propagtor, we have the probability amplitude at the new point in time and space through Equation 5.1, namely

$$\Psi(x',t') = \int\mathrm{d}x\,\hat{u}(x',t';x,t)\Psi(x,t) \tag{A.19}$$

A.2 Harmonic oscillator

By considering the path integral in imaginary time, we now derive the functional form of the radius of gyration for a particle in a harmonic potential.

The following identities are required:

[3]The limits on the integral are intended to show that x at the beginning and the end points (x and x') are fixed, and are therefore not integrated over in the functional.

$$\int_0^{2\pi} \cos mx \cos nx \, \mathrm{d}x = \frac{1}{2}\int_0^{2\pi} \cos(m+n)x \, \mathrm{d}x + \frac{1}{2}\int_0^{2\pi} \cos(m-n)x \, \mathrm{d}x = \pi\delta_{mn} \tag{A.20}$$

$$\int_0^{2\pi} \sin mx \sin nx \, \mathrm{d}x = \frac{1}{2}\int_0^{2\pi} \cos(m-n)x \, \mathrm{d}x - \frac{1}{2}\int_0^{2\pi} \cos(m+n)x \, \mathrm{d}x = \pi\delta_{mn}. \tag{A.21}$$

The radius of gyration squared is given by

$$\begin{aligned} \Delta^2 &= \left\langle (r(\tau) - \overline{r})^2 \right\rangle \\ &= \int \overline{\mathrm{D}}r \int_0^{\beta\hbar} \left[r(\tau) - \frac{1}{\beta\hbar}\int_0^{\beta\hbar} \mathrm{d}\tau' r(\tau') \right]^2 \\ &\quad \exp\left[-\frac{1}{\hbar}\int_0^{\beta\hbar} \mathrm{d}\tau'' \left(\frac{m}{2}\dot{r}^2 + \frac{m}{2}\omega_0^2 r^2 \right) \right]. \end{aligned} \tag{A.22}$$

We now expand $r(\tau)$ as a Fourier sine series with periodic boundary conditions in τ:

$$r(\tau) = r_0 + \sum_{n=1}^{\infty} a_n \sin\left(\frac{2n\pi\tau}{\beta\hbar} \right) \tag{A.23}$$

Noting that

$$\frac{1}{\beta\hbar}\int_0^{\beta\hbar} \mathrm{d}\tau' r(\tau') = r_0 \tag{A.24}$$

and also that

$$\begin{aligned}
&\int_0^{\beta\hbar} \mathrm{d}\tau \left[r(\tau) - \frac{1}{\beta\hbar} \int_0^{\beta\hbar} \mathrm{d}\tau' r(\tau') \right]^2 \\
&\quad = \int_0^{\beta\hbar} \mathrm{d}\tau \left[\sum_{n=1}^{\infty} a_n \sin\left(\frac{2n\pi\tau}{\beta\hbar}\right) \right]^2 \\
&\quad = \sum_{n'=1}^{\infty} \sum_{n=1}^{\infty} a_{n'} a_n \int_0^{\beta\hbar} \mathrm{d}\tau \sin\left(\frac{2n'\pi\tau}{\beta\hbar}\right) \sin\left(\frac{2n\pi\tau}{\beta\hbar}\right) \\
&\quad = \frac{\beta\hbar}{2\pi} \sum_{n'=1}^{\infty} \sum_{n=1}^{\infty} a_{n'} a_n \int_0^{2\pi} \mathrm{d}x \sin\left(n'x\right) \sin\left(nx\right)
\end{aligned} \tag{A.25}$$

where we have used $x = \frac{2\pi\tau}{\beta\hbar}$. We now use the fact that

$$\int_0^{2\pi} \mathrm{d}x \ \sin n'x \sin nx = \pi\delta_{nn'} \tag{A.26}$$

to see that

$$\begin{aligned}
&\int_0^{\beta\hbar} \mathrm{d}\tau \left[r(\tau) - \frac{1}{\beta\hbar} \int_0^{\beta\hbar} \mathrm{d}\tau' r(\tau') \right]^2 \\
&\quad = \frac{\beta\hbar}{2\pi} \sum_{n'=1}^{\infty} \sum_{n=1}^{\infty} a_{n'} a_n \int_0^{2\pi} \mathrm{d}x \sin\left(n'x\right) \sin\left(nx\right) \\
&\quad = \frac{\beta\hbar}{2\pi} \sum_{n'=1}^{\infty} \sum_{n=1}^{\infty} a_{n'} a_n \pi\delta_{n'n} \\
&\quad = \frac{\beta\hbar}{2} \sum_{n=1}^{\infty} a_n^2
\end{aligned} \tag{A.27}$$

Now we turn our attention to the integral in the argument of the exponential term as seen in Equation A.22. Noting that

$$r(\tau) = r_0 + \sum_{n=1}^{\infty} a_n \sin\left(\frac{2n\pi\tau}{\beta\hbar}\right) \tag{A.28a}$$

$$\dot{r}(\tau) = \sum_{n=1}^{\infty} a_n \frac{2n\pi}{\beta\hbar} \cos\left(\frac{2n\pi\tau}{\beta\hbar}\right) \tag{A.28b}$$

we may write

$$\begin{aligned}
&\int_0^{\beta\hbar} d\tau'' \left(\frac{m}{2}\dot{r}^2 + \frac{m}{2}\omega_0^2 r^2\right) \\
&\quad = \int_0^{\beta\hbar} \mathrm{d}\tau'' \frac{m}{2} \left[\sum_{n=1}^{\infty} a_n \left(\frac{2n\pi}{\beta\hbar}\right)^2 \cos\left(\frac{2n\pi\tau}{\beta\hbar}\right)\right]^2 \\
&\qquad + \int_0^{\beta\hbar} \mathrm{d}\tau'' \frac{m\omega_0^2}{2} \left[r_0 + \sum_{n=1}^{\infty} a_n \sin\left(\frac{2n\pi\tau}{\beta\hbar}\right)\right]^2
\end{aligned} \tag{A.29}$$

the cross terms between r_0 and the sine expansion in Equation A.29 vanish, since

$$\int_0^{\beta\hbar} \mathrm{d}\tau \sin\left(\frac{2n\pi\tau}{\beta\hbar}\right) = 0 \tag{A.30}$$

so that

$$\begin{aligned}
&\int_0^{\beta\hbar} \mathrm{d}\tau'' \left(\frac{m}{2}\dot{r}^2 + \frac{m}{2}\omega_0^2 r^2\right) \\
&\quad = \frac{\beta\hbar}{2\pi}\frac{m}{2}\left(\frac{2\pi}{\beta\hbar}\right)^2 \sum_{n'=1}^{\infty}\sum_{n=1}^{\infty} a_{n'} a_n n' n \int_0^{2\pi} \mathrm{d}x \cos n'x \cos nx \\
&\qquad + \frac{\beta\hbar}{2\pi}\frac{m\omega_0^2}{2} \sum_{n'=1}^{\infty}\sum_{n=1}^{\infty} a_{n'} a_n \int_0^{2\pi} \mathrm{d}x \sin n'x \sin nx \\
&\qquad + \frac{\beta\hbar}{2} m\omega_0^2 r_0^2
\end{aligned} \tag{A.31}$$

and finally

$$\begin{aligned}
&\int_0^{\beta\hbar} \mathrm{d}\tau'' \left(\frac{m}{2}\dot{r}^2 + \frac{m}{2}\omega_0^2 r^2\right) \\
&\quad = \frac{\beta\hbar}{2} \sum_{n=1}^{\infty} \left[\frac{m}{2}\left(\frac{2n\pi}{\beta\hbar}\right)^2 + \frac{m\omega_0^2}{2}\right] a_n^2 + \frac{\beta\hbar}{2} m\omega_0^2 r_0
\end{aligned} \tag{A.32}$$

The radius of gyration squared Δ^2 may now be written as

$$\Delta^2 \sim \int \mathrm{d}r_0 \int \mathrm{D}a_{n''} \left[\frac{\beta\hbar}{2}\sum_{n=1}^{\infty} a_{n'}^2\right] \exp\left\{-\frac{\beta}{2}\sum_{n=1}^{\infty}\left[\frac{m}{2}\left(\frac{2n\pi}{\beta\hbar}\right)^2 + \frac{m\omega_0^2}{2}\right] a_n^2\right\} \exp\left[-\frac{\beta}{2} m\omega_0^2 r_0^2\right]. \tag{A.33}$$

The integral over r_0 yields a constant factor of $\sqrt{\frac{2\pi}{\beta m\omega_0^2}}$.

Defining

$$\alpha = \frac{\beta}{2}\left[\frac{m}{2}\left(\frac{2n'\pi}{\beta\hbar}\right)^2 + \frac{m\omega_0^2}{2}\right] \tag{A.34}$$

and concentrating next on the functional integral[4]

$$\begin{aligned}
&\int \mathrm{D}a_{n''}\left(\frac{1}{2}\sum_{n'} a_{n'}^2\right)\exp\left\{-\frac{\beta}{2}\sum_{n=1}^{\infty}\left[\frac{m}{2}\left(\frac{2n\pi}{\beta\hbar}\right)^2 + \frac{m\omega_0^2}{2}\right] a_n^2\right\} \\
&= \sum_{n'}\int \mathrm{d}a_{n'}\, a_{n'}^2 \exp\left\{-\frac{\beta}{2}\left[\frac{m}{2}\left(\frac{2n'\pi}{\beta\hbar}\right)^2 + \frac{m\omega_0^2}{2}\right] a_{n'}^2\right\} \\
&\qquad \cdot \frac{1}{2}\int \mathrm{D}a_{n''\neq n'} \exp\left\{-\frac{\beta}{2}\sum_{n\neq n'}\left[\frac{m}{2}\left(\frac{2n\pi}{\beta\hbar}\right)^2 + \frac{m\omega_0^2}{2}\right] a_n^2\right\} \\
&= \sum_{n'} \frac{\pi^{\frac{1}{2}}}{4\left\{\frac{\beta}{2}\left[\frac{m}{2}\left(\frac{n'\pi}{\beta\hbar}\right)^2 + \frac{m\omega_0^2}{2}\right]\right\}^{\frac{3}{2}}} \\
&\qquad \cdot \int \mathrm{D}a_{n''\neq n'} \exp\left\{-\frac{\beta}{2}\sum_{n\neq n'}\left[\frac{m}{2}\left(\frac{2n\pi}{\beta\hbar}\right)^2 + \frac{m\omega_0^2}{2}\right] a_n^2\right\} \\
&= \sum_{n'} \frac{\pi^{\frac{1}{2}}}{4\left\{\frac{\beta}{2}\left[\frac{m}{2}\left(\frac{2n'\pi}{\beta\hbar}\right)^2 + \frac{m\omega_0^2}{2}\right]\right\}^{\frac{3}{2}}} \prod_{n''\neq n'}\left\{\frac{\pi}{\frac{\beta}{2}\left[\frac{m}{2}\left(\frac{2n''\pi}{\beta\hbar}\right)^2 + \frac{m\omega_0^2}{2}\right]}\right\}^{\frac{1}{2}} \\
&= \sum_{n'} \frac{1}{4\left\{\frac{\beta}{2}\left[\frac{m}{2}\left(\frac{2n'\pi}{\beta\hbar}\right)^2 + \frac{m\omega_0^2}{2}\right]\right\}} \prod_{n''}\left\{\frac{\pi}{\frac{\beta}{2}\left[\frac{m}{2}\left(\frac{2n''\pi}{\beta\hbar}\right)^2 + \frac{m\omega_0^2}{2}\right]}\right\}^{\frac{1}{2}}
\end{aligned} \tag{A.35}$$

[4] We use the fact that $\int_{-\infty}^{+\infty} x^2 e^{-\alpha x^2} = \frac{1}{2\alpha}\sqrt{\frac{\pi}{\alpha}}$.

Concentrating on the summation, we note that

$$\sum_{n'} \frac{1}{4\left\{\frac{\beta}{2}\left[\frac{m}{2}\left(\frac{2n'\pi}{\beta\hbar}\right)^2+\frac{m\omega_0^2}{2}\right]\right\}} = \frac{\beta\hbar^2}{4m\pi^2}\sum_{n'}\frac{1}{(n')^2+\left(\frac{\beta\hbar\omega_0}{2\pi}\right)^2} \tag{A.36}$$

We now require the identity

$$\coth(\pi x) = \frac{1}{\pi x} + \frac{2x}{\pi}\sum_{k=1}^{\infty}\frac{1}{k^2+x^2} \tag{A.37}$$

which rearranges to

$$\left(\frac{1}{2x^2}\right)\{\pi x\coth(\pi x)-1\} = \sum_{k=1}^{\infty}\frac{1}{k^2+x^2}. \tag{A.38}$$

We may now write Equation A.36 as

$$\sum_{n'} \frac{1}{4\left\{\frac{\beta}{2}\left[\frac{m}{2}\left(\frac{2n'\pi}{\beta\hbar}\right)^2+\frac{m\omega_0^2}{2}\right]\right\}} = \frac{1}{2\beta m\omega_0^2}\left\{\left(\frac{1}{2}\beta\hbar\omega_0\right)\coth\left(\frac{1}{2}\beta\hbar\omega_0\right)-1\right\} \tag{A.39}$$

and hence the radius of gyration squared Δ^2 has the form

$$\Delta^2 \sim \left\{\frac{\beta\hbar\omega_0}{2}\coth\left(\frac{\beta\hbar\omega_0}{2}\right)-1\right\}. \tag{A.40}$$

Glossary

Abbreviations

CCN Cumulative Coordination Number.

CM Centre of Mass.

DFT Density Functional Theory.

FCC Face Centered Cubic.

GGA Generalised Gradient Approximation.

H Hydrogen.

HB Hydrogen Bond.

HDA High Density Amorphous.

HDL High Density Liquid.

LDA Low Density Amorphous.

LDL Low Density Liquid.

LJ Lennard-Jones.

MD Molecular Dynamics.

MPI Message Passing Interface.

MUDPIES MolecUlar Dynamics using Path Integrals for Empirical Systems.

NN Nearest Neighbour.

O Oxygen.

PBC Periodic Boundary Conditions.

PI Path Integral.

PPC Polarisable Point Charge.

RGY Radius of Gyration.

RMS Root Mean Square.

SLC Stability Limit Conjecture.

SPC Simple Point Charge.

SPC/E Extended Simple Point Charge.

TIPnP Transferable Intermolecular Potential with n Points.

TIP5P(PI) TIP5P — Path Integral parameterisation.

TMD Temperature of Maximum Density.

VACF Velocity Auto-Correlation Function.

Definitions

Canonical Constant particle number, volume and temperature.

Centroid Mean or "classical" position of a quantum particle.

Coexistence curve Separates stable and metastable states.

Ergodic Fair and representative sampling of phasespace.

Isochoric Constant volume.

Microcanonical Constant particle number, volume and energy.

Reentrant Re-enters positive pressures as temperature is decreased.

Spinodal Separates metastable and unstable states.

Symbols

$\boldsymbol{v}$	Particle velocity.
$\boldsymbol{G}$	Reciprocal space lattice vector.
$\boldsymbol{R}$	Radius of gyration tensor.
$\boldsymbol{\Delta}$	Radius of gyration tensor.
$\boldsymbol{\sigma}$	Stress tensor.
$\boldsymbol{\tau}$	Torque.
$\boldsymbol{\varepsilon}$	Strain tensor.
$\boldsymbol{l}$	Real space lattice vector.
κ_{T}	Coefficient of isothermal expansion.
$\mathcal{L}$	Classical Lagrangian function.
$\mathsf{J}_{\alpha\beta}$	Components of the pressure tensor.
P	Scalar pressure.
Ω	Simulation cell volume.
$\Psi(\boldsymbol{r}_1, \boldsymbol{r}_2, \ldots, \boldsymbol{r}_N)$	Many body wavefunction.
ψ_i	Kohn-Sham orbital.
$\sigma(A)$	Root mean square fluctuation on the quantity A.
τ	Imaginary time.
C_{p}	Isobaric heat capacity.
E	Total energy.
E_{ion}	Ion-ion interaction energy.
E_{xc}	Exchange-correlation interaction energy.
m	Particle mass.
N	Particle number.
$n(\boldsymbol{r})$	Electron density.

P	Number of path integral beads.
$S[x]$	Classical action as a functional of x.
t	Real time.
V_{H}	Hartree potential.
V_{ion}	Ion-ion interaction potential.
V_{xc}	Exchange-correlation potential.
β	$\frac{1}{k_{\mathrm{B}}T}$.
ρ	Number density.

Bibliography

Allen, M. P. and Tildesley, D. J. (1987). *Computer Simulation of Liquids.* Clarendon Press, Oxford.

Andersen, H. C. (1983). Rattle: A "velocity" version of the shake algorithm for molecular dynamics calculations. *J. Comput. Phys.*, **52**, 24–34.

Baez, L. A. and Clancy, P. (1994). Existence of a density maximum in extended simple point-charge water. *J. Chem. Phys.*, **101**, 9837–9840.

Berendsen, H. J. C., Grigera, J. R., and Straatsma, T. P. (1987). The missing term in effective pair potentials. *J. Phys. Chem.*, **91**, 6269–6271.

Bernal, J. D. and Fowler, R. H. (1933). A theory of water in ionic solution, with particular reference to hydrogen and hydroxyl ions. *J. Chem. Phys.*, **1**(8), 515–548.

Billeter, S. R., King, P. M., and Gunsteren, W. F. (1994). Can the density maximum of water be found by computer simulation? *J. Chem. Phys.*, **100**(9), 6692–6699.

Borick, S. S. and Debenedetti, P. G. (1993). Equilibrium, stability, and density anomalies in a lattice model with core-softening and directional bonding. *J. Phys. Chem.*, **97**, 6292–6303.

Bosio, L., Chen, S., and Teixeira, J. (1983). Isochoric temperature differential of the x-ray structure factor and structural rearrangements in low temperature heavy water. *Phys. Rev. A*, **27**, 1468–1475.

Chandrasekhar, S. (1943). Stochastic problems in physics and astronomy. *Rev. Mod. Phys.*, **15**(1), 1–89.

Cho, Singh, and Robinson (1996a). An explanation of the density maximum in water. *Phys. Rev. Lett.*, **76**(10), 1651–1654.

Cho, C. H., Singh, S., and Robinson, G. W. (1996b). The Royal Society of Chemistry Faraday division general discussion. (103).

Cho, C. H., Singh, S., and Robinson, G. W. (1997). Understanding all of water's anomalies with a nonlocal potential. *J. Chem. Phys.*, **107**(19), 7979–7988.

Coulson, C. A. (1961). *Valence*. Oxford University Press, second edition.

Del Buono, G. S., Rossky, P., and Schnitker, J. J. (1991). Model dependence of quantum isotope effects in liquid water. *J. Chem. Phys.*, **95**, 3728–3737.

Ding, K., Chandler, D., Smithline, S. J., and Haymet, A. D. J. (1987). Density-functional theory for the freezing of water. *Phys. Rev. Lett.*, **59**(15), 1698–1701.

Dyke, T. R., Mack, K. M., and Muenter, J. S. (1977). The structure of the water dimer from molecular beam electric resonance spectroscopy. *J. Chem. Phys.*, **66**, 498–510.

Einsenberg, D. and Kauzmann, W. (1969). *The Structure and Properties of Water*. Oxford University Press.

Errington, J. and Debenedetti, P. (2001). Relationship between stuctural order and the anomalies of liquid water. *Nature*, **409**, 318–321.

Errington, J., Debenedetti, P., and Torquato, S. (2002). Cooperative origin of low-density domains in liquid water. *Phys. Rev. Lett.*, **89**(21), 25503–1.

Espinosa, E., Molins, E., and Lecomte, C. (1998). Hydrogen bond strengths revealed by topological analyses of experimentally observed electron densities. *Chem. Phys. Lett.*, **285**, 170–173.

Ewald, P. P. (1921). Die berechnung optischer und elektrostatischer gitterpotentiale. *Ann. Phys.*, **64**, 253–287.

Feynman, R. P. (1948). Space-time approach to non-relativistic quantum mechanics. *Rev. Mod. Phys.*, **20**(2), 367–387.

Feynman, R. P. and Hibbs, A. R. (1965). *Quantum Mechanics & Path Integrals*. McGraw-Hill.

Flyvbjerg, H. and Petersen, H. G. (1989). Error estimates on averages of correlated data. *J. Chem. Phys.*, **91**, 461–466.

Frank, H. S. (1958). Covalency in the hydrogen bond and the properties of water and ice. *Proc. Roy. Soc. (London)*, **A247**, 481–492.

Frank, H. S. (1972). *Water: A Comprehensive Treatise.*, volume 1. Plenum, New York. Chapter 14.

Frank, H. S. and Wen, W. Y. (1957). Structural aspects of ion-solvent interaction in aqueous solutions: A suggested picture of water structure. *Disc. Faraday. Soc.*, (24), 133–140.

Franks, F. (1972). *Water: A Comprehensive Treatise.*, volume 1. Plenum, New York. Chapter 1.

Franks, F. (1983). *Water.* Royal Society of Chemistry.

Franks, F. (2000). *Water. A Matrix of Life.* Royal Society of Chemistry, Cambridge., second edition.

Frenkel, D. and Smit, B. (1996). *Understanding Molecular Simulation.* Academic Press.

Friedberg, R. and Cameron, J. E. (1970). Test of the Monte Carlo method: Fast simulation of a small Ising lattice. *J. Chem. Phys.*, **64**, 6049–6058.

Gillan, M. J. (1988). The quantum simulation of hydrogen in metals. *Phil. Mag. A*, **58**(1), 257–283.

Ginnings, D. C. and Corruccini, R. J. (1947). An improved ice calorimeter — the determination of its calibration factor and the density of ice at 0°C. *Journal of Research of the National Bureau of Standards.*, **38**, 583–591.

Goldblatt, M. (1964). The density of liquid T_2O. *J. Phys. Chem.*, **68**, 147–151.

Grigera, J. R. (2001). An effective pair potential for heavy water. *J. Chem. Phys.*, **114**(18), 8064–8067.

Guillot, B. (2002). A reappraisal of what we have learnt during three decades of computer simulations on water. *J. Mol. Liquids*, **101**, 219–260.

Guillot, B. and Guissani, Y. (1998). Quantum effects in simulated water by the Feynmann-Hibbs approach. *J. Chem. Phys.*, **108**(24), 10162–10174.

Guzzi, R., Arcangeli, C., and Bizzarri, A. R. (1999). A molecular dynamics simulation study of the solvent isotope effect on copper plastocyanin. *Biophys. Chem.*, **82**, 9–22.

Haile, J. M. (1992). *Molecular Dynamics Simulation. Elementary Methods.* J. Wiley & Sons. Inc.

Heath, D. F. and Linnett, J. W. (1948). Molecular force fields. I. the structure of the water molecule. *Trans. Faraday. Soc.*, (44), 556–561.

Hohenberg, P. and Kohn, W. (1964). Inhomogeneous electron gas. *Phys. Rev.*, **136**, B864–B871.

Isaacs, E. D., Shukla, A., Platzman, P. M., Hamann, D. R., Barbiellini, D., and Tulk, C. A. (2000). Compton scattering evidence for covalency of the hydrogen bond in ice. *J. Phys. Chem. Solids*, **61**, 403–406.

Jedlovszky, P. and Vallauri, R. (2001). Thermodynamic and structural properties of liquid water around the temperature of maximum density in a wide range of pressures: A computer simulation study with a polarizable potential model. *J. Chem. Phys.*, **115**, 3750–3672.

Jedlovszky, P., Mezei, M., and Vallauri, R. (2000). A molecular level explanation of the density maximum of liquid water from computer simluations with a polarizable potential model. *Chem. Phys. Lett.*, **318**, 155–160.

Kell, G. S. (1967). Precise representation of volume properties of water at one atmosphere. *J. Chem. Eng. Data*, **12**, 66–69.

Khan, A. (2000). A liquid water model: Density variation from supercooled to superheated states, prediction of h-bonds, and temperature limits. *J. Phys. Chem.*, **104**, 11268–11274.

Kirshenbaum, I. (1951). *Physical Properties and Analysis of Heavy Water.* McGraw-Hill, New York.

Kittel, C. (1996). *Introduction to Solid State Physics*. Wiley, seventh edition.

Kohn, W. and Sham, L. J. (1965). Self-consistent equations including exchange and correlation effects. *Phys. Rev.*, **140**, A1133–A1138.

Kuharski, R. A. and Rossky, P. (1985). A quantum mechanical study of structure in liquid H_2O and D_2O. *J. Chem. Phys.*, **82**, 5164–5177.

Latimer, M. and Rodebush, W. H. (1920). Polarity and ionization from the standpoint of the Lewis theory of valence. *J. Am. Chem. Soc.*, **42**, 1419–1433.

Lísal, M., Kolafa, J., and Nezbeda, I. (2002). An examination of the five-site potential (TIP5P) for water. *J. Chem. Phys.*, **2002**(19), 8892–8897.

Lobaugh, J. and Voth, G. A. (1997). A quantum model for water: Equilibrium and dynamical properties. *J. Chem. Phys.*, **106**, 2400.

Mahoney, M. W. and Jorgensen, W. L. (2000). A five-site model for liquid water and the reproduction of the density anomaly by rigid, nonpolarizable potential functions. *J. Chem. Phys.*, **112**(20), 8910–8922.

Mahoney, M. W. and Jorgensen, W. L. (2001). Quantum, intramolecular flexibility, and polarizability effects on the reproduction of the density anomaly of liquid water by simple potential functions. *J. Chem. Phys.*, **115**(23), 10758–10768.

Mandl, F. (1988). *Statistical Physics*. The Manchester physics series. Wiley, second edition.

Martí, J., Padro, J. A., and Guardia, E. (1996). Molecular dynamics simulation of water along the coexistence curve: Hydrogen bonds and vibrational spectra. *J. Chem. Phys.*, **105**, 639–649.

Megaw, H. D. (1934). *Nature*, **134**, 900.

Mishima, O. (1994). Reversible first-order transition between two H_2O amorphs at ~ 0.2 GPa and ~ 135 K. *J. Chem. Phys.*, **100**, 5910–5912.

Mishima, O. (2000). Liquid-liquid critical point in heavy water. *Phys. Rev. Lett.*, **85**(2), 334–336.

Modig, K., Pfrommer, P. G., and Halle, B. (2003). Temperature-dependent hydrogen-bond geometry in liquid water. *Phys. Rev. Lett.*, **90**(7), 075502.

Morgan, J. and Warren, B. E. (1938). X-ray analysis of the structure of liquid water. *J. Chem. Phys.*, **6**, 666—673.

Myneni, S., Luo, Y., Näslund, L. r., Cavalleri, M., L., O., Ogasawara, H. Pelmenschikov, A., Wernet, P., Väterlein, P., Heske, C., Hussain, Z., Pettersson, L. G. M., and Nilsson, A. (2002). Spectroscopic probing of local hydrogen-bonding structures in liquid water. *J. Phys.: Condens. Matter*, **14**, L213–L219.

Narten, A. H., Danford, M. D., and Levy, H. A. (1967). X-ray diffraction study of liquid water in the temperature range 4–200°c. *Discuss. Faraday Soc.*, **43**, 97–107.

Némethy, G. and Scheraga, H. A. (1962). Structure of water and hydrophobic bonding in proteins. I. a model for the thermodynamic properties of liquid water. *J. Chem. Phys*, **36**(12), 3382.

Némethy, G. and Scheraga, H. A. (1964). Structure of water and hydrophobic bonding in proteins. IV. the thermodynamic properties of liquid deuterium oxide. *J. Chem. Phys*, **41**, 680.

Neuefeind, J., Benmore, C. J., Tomberli, B., and Egelstaff, P. A. (2002). Experimental determination of the electron density of liquid H_2O and D_2O. *J. Phys.:Condens. Matter*, **14**, L429–L433.

Nielsen, G. H. and Martin, R. M. (1982). Stresses in semiconductors: *Ab initio* calculations on si, ge, and gaas. *Phys. Rev. B*, **32**, 3792–3805.

Odutola, J. A. and Dyke, T. R. (1980). Partially deuterated water dimers: Microwave spectra and structure. *J. Chem. Phys.*, **72**, 5062–5070.

Pauling, L. (1935). The structure and entropy of ice and of other crystals with some randomness of atomic arrangement. *J. Am. Chem. Soc.*, **57**, 2680–2684.

Perdew, J. P., Burke, K., and Ernzerhof, M. (1996). Generalised gradient approximation made simple. *Phys. Rev. Lett.*, **77**, 3865–3868.

Petrenko, V. F. and Whitworth, R. W. (1999). *Physics of Ice*. Oxford University Press.

Poole, P. H., Sciortino, F., Essmann, U., and Stanley, H. E. (1992). Phase behaviour of metastable water. *Nature*, **360**, 324.

Poole, P. H., Sciortino, F., Essmann, U., and Stanlet, H. E. (1993). Spinodal of liquid water. *Phys. Rev. E*, **48**, 3799–3817.

Poole, P. H., Sciortino, F., Grande, T., Stanley, H. E., and Angell, C. A. (1994). Effect of hydrogen bonds on the thermodynamic behavior of liquid water. *Phys. Rev. Lett.*, **73**(12), 1632–1635.

Pople, J. A. (1951). Molecular association in liquids. II. a theory of the structure of water. *Proc. Roy. Soc. A*, **205**, 163–178.

Prins and Petersen (1936). *Physica*, **3**, 147.

Rapaport, D. C. (1995). *The Art of Molecular Dynamics Simulation*. Cambridge University Press.

Röttger, K., Endriss, A., Ihringer, J., Doyle, S., and Kuhs, W. F. (1994). Lattice constants and thermal expansion of H_2O and D_2O ice Ih between 10 and 265 K. *Acta Crystallographica*, **B50**, 644–648.

Ruscic, B., Wagner, A. F., Harding, L. B., Asher, R. L., Feller, D., Dixon, D. A., Peterson, K. A., Song, Y., Qian, X., Ng, C., Liu, J., Chen, W., and Schwenke, D. W. (2002). On the enthalpy of formation of hydroxyl radical and gas-phase bond dissociation energies of water and hydroxyl. *J. Phys. Chem. A*, **106**, 2727–2747.

Sastry, S., Sciortino, F., and Stanley, H. E. (1993). Limits of stability of the liquid phase in a lattice model with water-like properties. *J. Chem. Phys.*, **98**(12), 9863–9871.

Sastry, S., Debenedetti, P. G., Sciortino, F., and Stanley, H. E. (1996). Singularity-free interpretation of the thermodynamics of supercooled water. *Phys. Rev. E*, **53**(6), 6144–6154.

Sato, H. and Fumio, H. (1999). *Ab initio* study of water. II. liquid structure, electronic and thermodynamic properties over a wide range of temperature and density. *J. Chem. Phys.*, **111**(18), 8545–8555.

Schwegler, E., Galli, G., and Gyri, F. (2000). Water under pressure. *Phys. Rev. Lett.*, **84**(11), 2429–2432.

Sciortino, F., Geiger, A., and Stanley, H. E. (1990). Isochoric differential scattering functions in liquid water: The fifth neighbor as a network defect. *Phys. Rev. Lett.*, **65**(27), 3452–3455.

Sciortino, F., Geiger, A., and Stanley, H. E. (1991). Effects of defects on molecular mobility in liquid water. *Nature (London)*, **354**, 218–221.

Segall, M. D., Lindan, P. L. D., Probert, M. J., Pickard, C. J., Hasnip, P. J., Clark, S. J., and Payne, M. C. (2002). First-principles simulation: Ideas, illustrations and the CASTEP code. *J. Phys.: Cond. Matt.*, **14**(11), 2717–2743.

Shiga, M., Tachikawa, M., and Miura, S. (2000). Ab initio molecular orbital calculation considering the quantum mechanical effect of nuclei by path integral molecular dynamics. *Chem. Phys. Lett.*, **332**(3–4), 396–402.

Simons, B. D. (1999/2000). Part III natural sciences lecture course "phase transitions and collective phenomena". University of Cambridge.

Speedy, R. J. (1982a). Limiting forms of the thermodynamic divergences at the conjectured stability limits in superheated and supercooled water. *J. Phys. Chem.*, **86**, 3002–3005.

Speedy, R. J. (1982b). Stability-limit conjecture. an interpretation of the properties of water. *J. Phys. Chem.*, **86**, 982–991.

Speedy, R. J. (1987). Thermodynamic properties of supercooled water at 1 atm. *J. Phys. Chem.*, **91**, 3354–3358.

Speedy, R. J. and Angell, C. A. (1976). Isothermal compressibility of supercooled water and evidence for a thermodynamic singularity at -45°C. *J. Chem. Phys.*, **65**, 851–858.

Stanley, H. E. and Teixeira, J. (1980). Interpretation of the unusual behaviour of H_2O and D_2O at low temperatures: Tests of a percolation model. *J. Chem. Phys.*, **73**, 3404.

Stanley, H. E., Buldyrev, S. V., Canpolat, M., Mishima, O., Sadr-Lahijany, M. R., Scala, A., and Starr, F. W. (2000). The puzzling behaviour of water at very low temperature. *Phys. Chem. Chem. Phys.*, **2**, 1551–1558.

Steinbach, P. J., Longcharich, J., and Brooks, B. R. (1991). The effects of environment and hydration on protein dynamics: A simulation study of myoglobin. *Chem. Phys.*, **158**, 383–394.

Stern, H. A. and Berne, B. J. (2001). Quantum effects in liquid water: Path-integral simulations of a flexible and polarizable *ab initio* model. *J. Chem. Phys.*, **115**(16), 7622–7628.

Stillinger, F. H. and Rahman, A. (1974). Improved simulation of liquid water by molecular dynamics. *J. Chem. Phys.*, **60**, 1545–1557.

Suresh, S. J. and Naik, V. M. (2000). Hydrogen bond thermodynamic properties of water from dielectric constant data. *J. Chem. Phys.*, **113**(21), 9727–9732.

Svishchev, I. M. and Hayward, T. M. (1999). Phase coexistence properties for the polarizable point charge model of water and the effects of applied electric field. *J. Chem. Phys.*, **111**(19), 9034–9038.

Svishchev, I. M., Kusalik, P. G., Wang, J., and Boyd, R. J. (1996). Polarizable point-charge model for water: Results under normal and extreme conditions. *J. Chem. Phys.*, **105**, 4742–4750.

Swope, W. C., Andersen, H. C., Berens, P. H., and Wilson, K. R. (1982). A computer simulation method for the calculation of equilibrium constants for the formation of physical clusters of molecules: Application to small water clusters. *J. Chem. Phys.*, **76**, 637–649.

Tanaka, H. (1998a). Fluctuation of local order and connectivity of water molecules in two phases of supercooled water. *Phys. Rev. Lett.*, **80**(1), 113–116.

Tanaka, H. (1998b). Simple physical explanation for the unusual thermodynamic behavior of liquid water. *Phys. Rev. Lett.*, **80**(26), 5750–5753.

Tanaka, H. (2001). Hydrogen bonds between water molecules: Thermal and expansivity of ice and water. *J. Mol. Liquids*, **90**, 323–332.

Tomberli, B., Benmore, C. J., Egelstaff, P. A., Neuefeind, J., and Honkimäki (2000). Isotopic quantum effects in water structure measured with high energy photon diffraction. *J. Phys.: Condens. Matter*, **12**, 2597–2612.

Truskett, T. M. and Dill, K. A. (2002). Predicting water's phase diagram and liquid-state anomalies. *J. Chem. Phys.*, **117**(11), 5101–5104.

Verlet, L. (1967). Computer 'experiments' on classical fluids. I. thermodynamical properties of Lennard-Jones molecules. *Phys. Rev.*, **159**, 98–103.

Walton, A. J. (1983). *Three Phases of Matter.* Clarendon Press, Oxford., second edition.

Watanabe, H. (1991). Thermal dilation of water between 0°C and 44°C. *Metrologia*, **28**, 33–43.

Xantheas, S. S. and Dunning, T. H. J. (1993). *Ab initio* studies of cyclic water clusters $(H_2O)_n$, n = 1–6. I. optimal structures and vibrational spectra. *J. Chem. Phys.*, **99**, 8774–8792.

Yamada, M., Mossa, S., Stanley, H. E., and Sciortino, F. (2002). Interplay between time-temperature transformation and the liquid-liquid phase transistion in water. *Phys. Rev. Lett.*, **88**(19), 195701–1.

Index